SITE CHARACTERIZATION OF THE LOS ANGELES BASIN USING AMBIENT NOISE SPECTRAL RATIO MEASUREMENTS FROM A HIGH DENSITY TEMPORARY BROADBAND DEPLOYMENT

A Thesis

Presented to the

Faculty of

California State Polytechnic University, Pomona

In Partial Fulfillment

Of the Requirements for the Degree

Master of Science

In

Geological Sciences

By

Raymond Ng

2017

SIGNATURE PAGE

THESIS: SITE CHARACTERIZATION OF THE LOS ANGELES BASIN USING AMBIENT NOISE SPECTRAL RATIO MEASUREMENTS FROM A HIGH DENSITY TEMPORARY BROADBAND DEPLOYMENT

AUTHOR: Raymond Ng

DATE SUBMITTED: Winter 2017

Geological Sciences Department

Dr. Jascha Polet
Thesis Committee Chair
Geological Sciences

Dr. Jonathan A. Nourse
Geological Sciences

Dr. Nicholas Van Buer
Geological Sciences

ACKNOWLEDGMENTS

This thesis is dedicated to the new generation in my family. May this thesis motivate you to strive for greatness.

Thanks to all the participants of the LASSIE project for allowing the installation of the seismometers on their property. Thank you to all the graduate and undergraduate students who has provided assistance in this project from installation and maintenance to computer trouble shooting. Special thanks to my family and friends who have supported me well before the start of and throughout my graduate career.

Thank you Brent V. Nourm for computer troubleshooting.

Thank you SCEC for partial funding. Installation, service visits, and uninstallation help : Mikey Herrman, Kennis Ho, Terry Cheiffetz, Dandan Zhang, Rosa Nguyen, Jonathan Marshak, Garrett Pankratz Thank you Magali Barba for helping me set up initially with LaTex Thank you Dr. Amber Rosin and Dr. Ryan Szypowski from the Department of Mathematics and Statistics for your time in helping me trouble shoot LaTex.

Finally, thank you Dr. Jascha Polet for guiding me every step of the way and encouraging me to push myself to become better. I have truly learned a lot under your guidance and wish to continue to learn from you for years to come.

ABSTRACT

Earthquake hazard is an increasing concern in densely populated, high-rise cities built on basins. The Los Angeles basin is home to roughly nine million people and a complex fault system. It is well established that sedimentary basins, such as the LA basin, can significantly amplify ground motion and increase its duration. Past earthquakes have shown that site response has a major influence on seismic damage and loss in urban areas. To account for site response, improve the understanding of the damaging ground motions produced in earthquakes and develop better seismic hazard assessment and mitigation in this highly developed area, it is essential to determine site characteristics, such as resonance frequency and amplification, across the basin at a high spatial resolution. Standard methods for site response investigation use data from historic earthquakes and other seismic sources, such as explosions, to gather information about site specific responses. Station coverage for these approaches, however, is incomplete and thus cannot provide high resolution imaging. Furthermore, historic earthquake data is not always available and explosive sources are not permitted in an urban setting. Therefore, other methods have been developed, such as the spectral analysis of the ambient noise field. We present the results of our investigation of site response within the Los Angeles Basin through the application of the microtremor Horizontal-to-Vertical spectral ratio (HVSR) approach. This method was implemented on 3-component broadband waveforms from the Los Angeles Syncline Seismic Interferometry Experiment (LASSIE). LASSIE is a collaborative, temporary, and dense array of 73 broadband seismometers that were active for a two-month period from October until November 2014, transecting the Los Angeles basin from Long Beach to La Puente. The data from this array enabled us to make measurements of small-

scale lateral variations in the peak frequencies and amplitudes of the HVSR curve across this highly populated sedimentary basin. Data analysis and interpretation were conducted in accordance with the Site Effects Assessment Using Ambient Excitations (SESAME) guidelines. The spectral peak amplitudes and peak frequencies both show variation across the LASSIE network, even between stations that are spaced only 1 km apart, suggesting that the site response in this area varies on a very small scale emphasizing the importance of microzonation. Our results show an average resonance period at the basin center of 6 to 10 sec, and additional peaks in the spectral ratio curves at much shorter periods for sites at the basin edge. Given this resonance period, buildings located within the basin that are between 60 to 100 stories in height could experience double resonance. Secondary intermittent peaks are also observed and based on their locations, on the edge of the basin and in areas with topographic highs, they may be explained using basin edge resonance, the presence of small scale basins, and/or topographic effects. Amplified shaking from resonance is characterized by the long period HVSR peak amplitudes ranging from 2 to 5.5, with the highest values measured for the greater Long Beach area. Assuming a simplified model of a sedimentary layer over a bedrock half-space, we calculate basin depth along the LASSIE transect from the resonance frequencies and compare it to various LA basin models. Our calculated depths over the deepest part of the basin are shallower than for these models. We can explain these differences by oversimplifications in the assumptions made in the calculation, errors in the velocity models, or physical complications introduced by the large dimensions of the LA basin.

Contents

List of Tables

List of Figures

Chapter 1

Introduction

Earthquake hazard is an increasing concern in densely populated, high-rise cities built on basins. It has been well documented that basins amplify earthquake ground motion by, for example, Frankel et al. (2002); Hall & Beck (1986); Kagami et al. (1986), and Abbott (2005). Resonance is one reason for amplified ground motion in basins. Resonance and other forms of ground motion amplification due to basin sediments raise many questions regarding areas such as the Los Angeles basin, as investigated by Rogers et al. (1979); Brady et al. (1988); Yomogida & Etgen (1993); Hruby & Beresnev (2003); Wald & Graves (1998); Olsen (2000) and Beresnev et al. (1998). Further investigation of the basin resonance in the Los Angeles basin through studies such as those conducted by Louie (2006, 2007); Mahdyiar (2002) and Mihalic et al. (2011) help improve earthquake engineering standards and hazard assessments. Basin resonance and ground motion amplification in basins has been observed in numerous historical events where significant loss and failure of large structures was observed due to ground motion amplification, such as the well studied 1985 Michoacan earthquake as evidenced by Hall & Beck (1986); Flores-Estrella

et al. (2007) and Lermo & Chavez - Garcia (1994), the 1987 Whittier earthquake by Hruby & Beresnev (2003) and Kawase & Aki (1990), and the 1994 Northridge earthquake, by Hruby & Beresnev (2003); Beresnev et al. (1998); Hartzell et al. (1996); Graves (1995); Olsen (2000) and Field et al. (2001).

The Los Angeles basin has been a topic of interest for over a century for scientific research in seismic hazards, and even longer for the many raw resources in the region. The most obvious commercial interest is in the oil fields, located primarily in the Long Beach area. Development in the Los Angeles basin would not have been possible without interest in its natural resources, such as petroleum. The research in oil development led to extensive geologic research of the LA basin, discovery of faults, stratigraphy, and seismic data acquisition and interpretation. With this thesis, we add to this body of work through our investigation of the seismic amplification and the resonance period of the Los Angeles basin as determined from waveform data from a temporary seismic network that we installed.

1.1 Los Angeles basin

1.1.1 Los Angeles basin tectonic history

The Los Angeles basin, shown in figures 1.1 and 1.2, is a coastal plain of alluviated lowland that slopes gently south towards the coast, interrupted by a series of low hills from Beverly Hills to Newport and the Palos Verdes hills in the southernmost section. A very complicated network of faults is scattered throughout the basin as seen in figure 1.2. Studies in LA basin stratigraphy, tectonic history, and basin structure are extensive

and further understanding of the Los Angeles basin characteristics is important for future investigations and application to seismic hazard mitigation.

The tectonic evolution of the Miocene pull-apart basin that we know as the LA basin has progressed quickly with the evolving San Andreas transform zone that forms the boundary between the Pacific and North American plates. Ingersoll & Rumelhart (1999) proposed a three stage evolution of the Los Angeles basin: transrotation (18 - 12 Ma), transtension (12 - 6 Ma), and transpression (6 - 0 Ma). Throughout the Paleogene (56 Ma), the Farallon Plate subducted beneath the North American plate as discussed in Nilsen (1987). This is evidenced by the arc volcanism in the Sierra Nevada during the Oligocene to Miocene, as shown in Graham (1987). In middle Miocene, the rifting of the western margin of the North American plate is attributed to the upwelling from the overridden spreading center beneath the North American plate described in Yeats (1968) and Wright (1991). Complex rotation, as proposed by Nicholson et al. (1994), rotated the Transverse Ranges block, caused by the transpressional dextral transform motion resulting from the partially subducted Monterey microplate. As proposed by Wright (1991), the deposition of sediments occurred throughout most of the Eocene in the remnant forearc basin of the Los Angeles area. Early Pliocene northwestward extension created structural traps for oil in the basin. Associated underthrusting of the Peninsular Range block beneath the Transverse Ranges in the late Pliocene contraction contributed to present day shortening of the Los Angeles basin.

In the present day, the Los Angeles Basin is bounded by the Santa Monica Mountains, the Elysian, Repetto, and Puente Hills in the north, and on the east and southeast by the

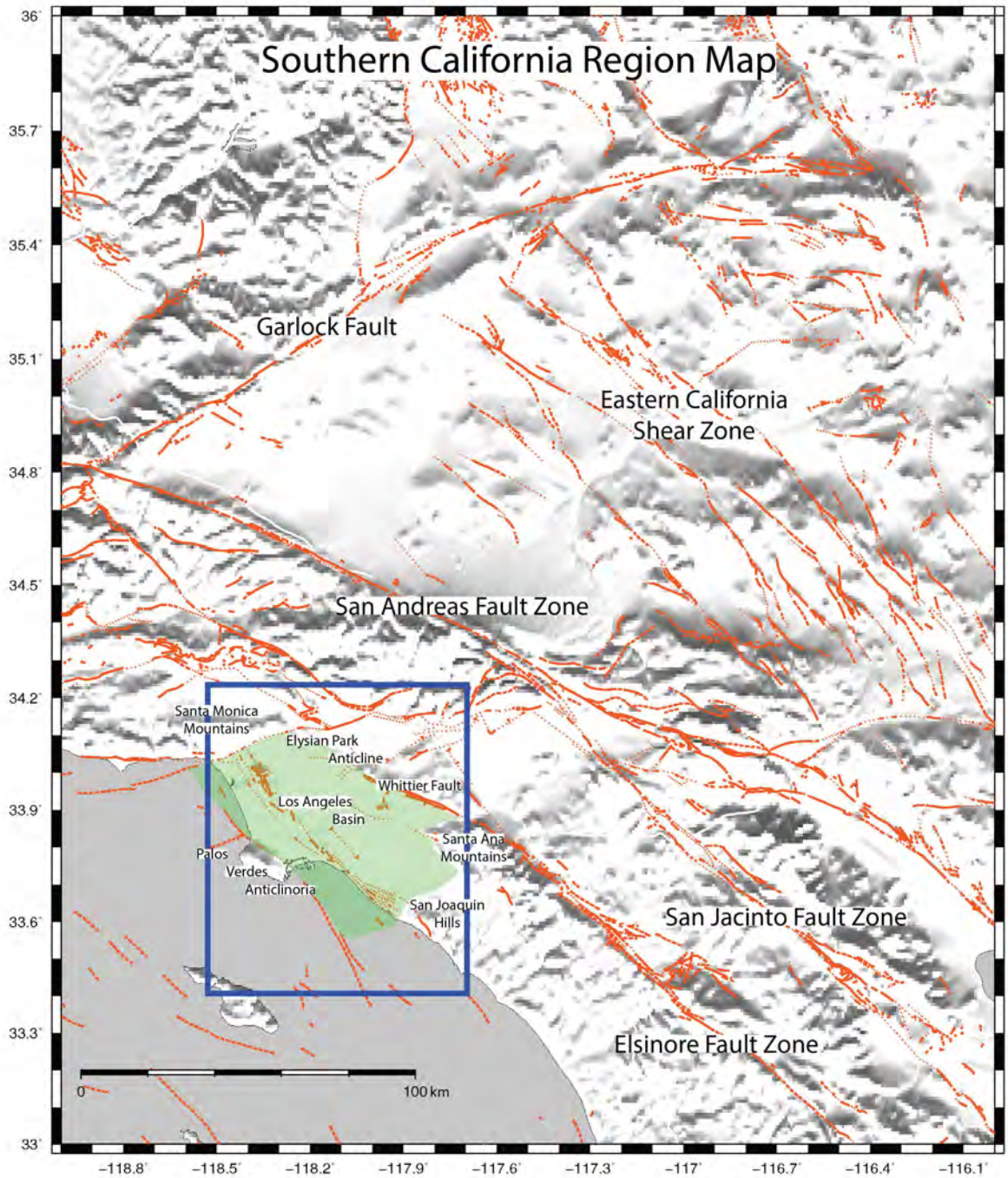

Figure 1.1: *Southern California regional map. A map of the Los Angeles basin's general location is shown in green and framed with a blue rectangle. Important features are labeled. Quaternary faults are shown by orange lines.*

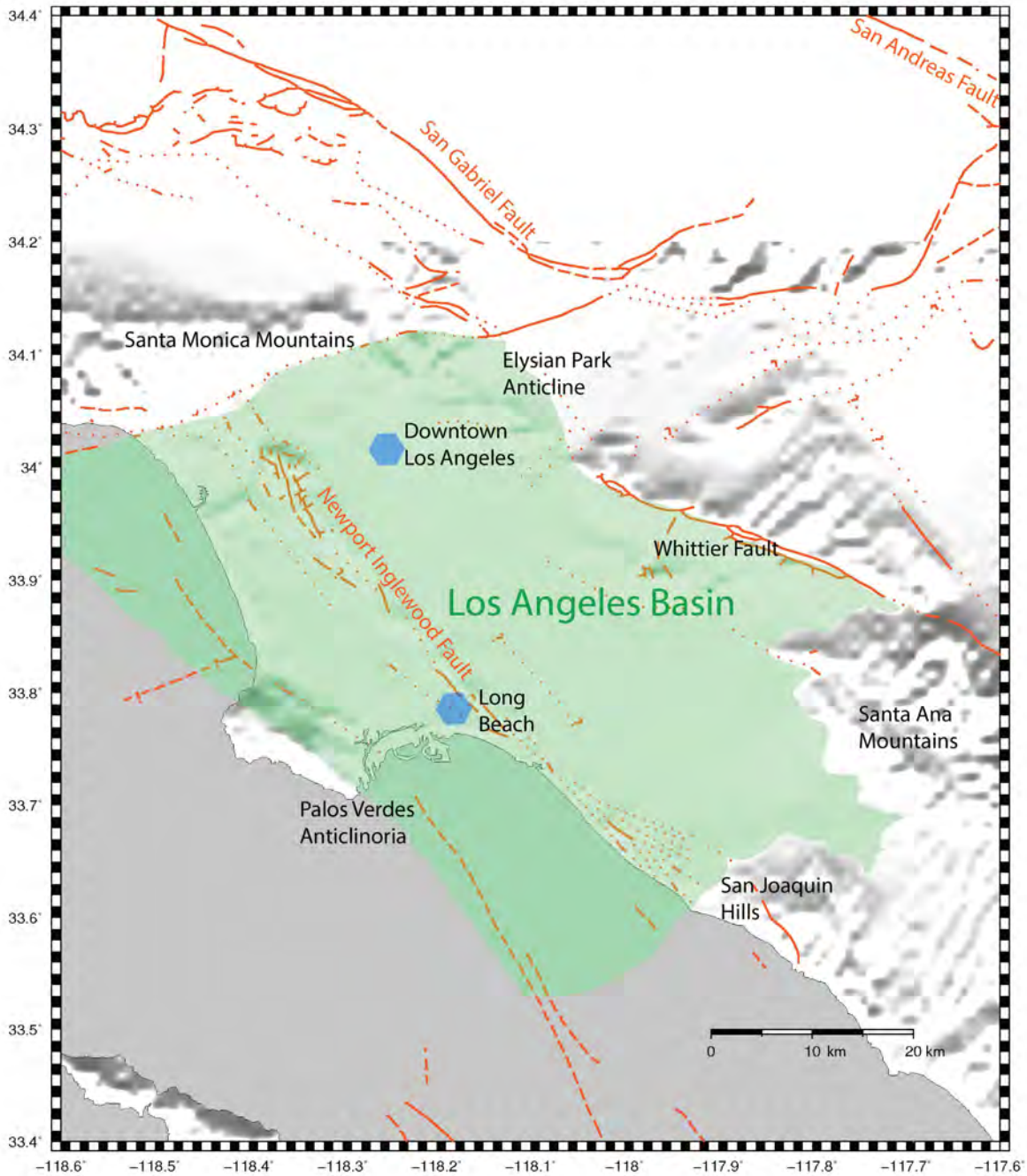

Figure 1.2: *Map of the Los Angeles basin. Zoom in map from the blue box shown in figure 1.1. Colors and labels as in figure 1.1. The location of downtown Los Angeles and Long Beach are shown by blue polygons.*

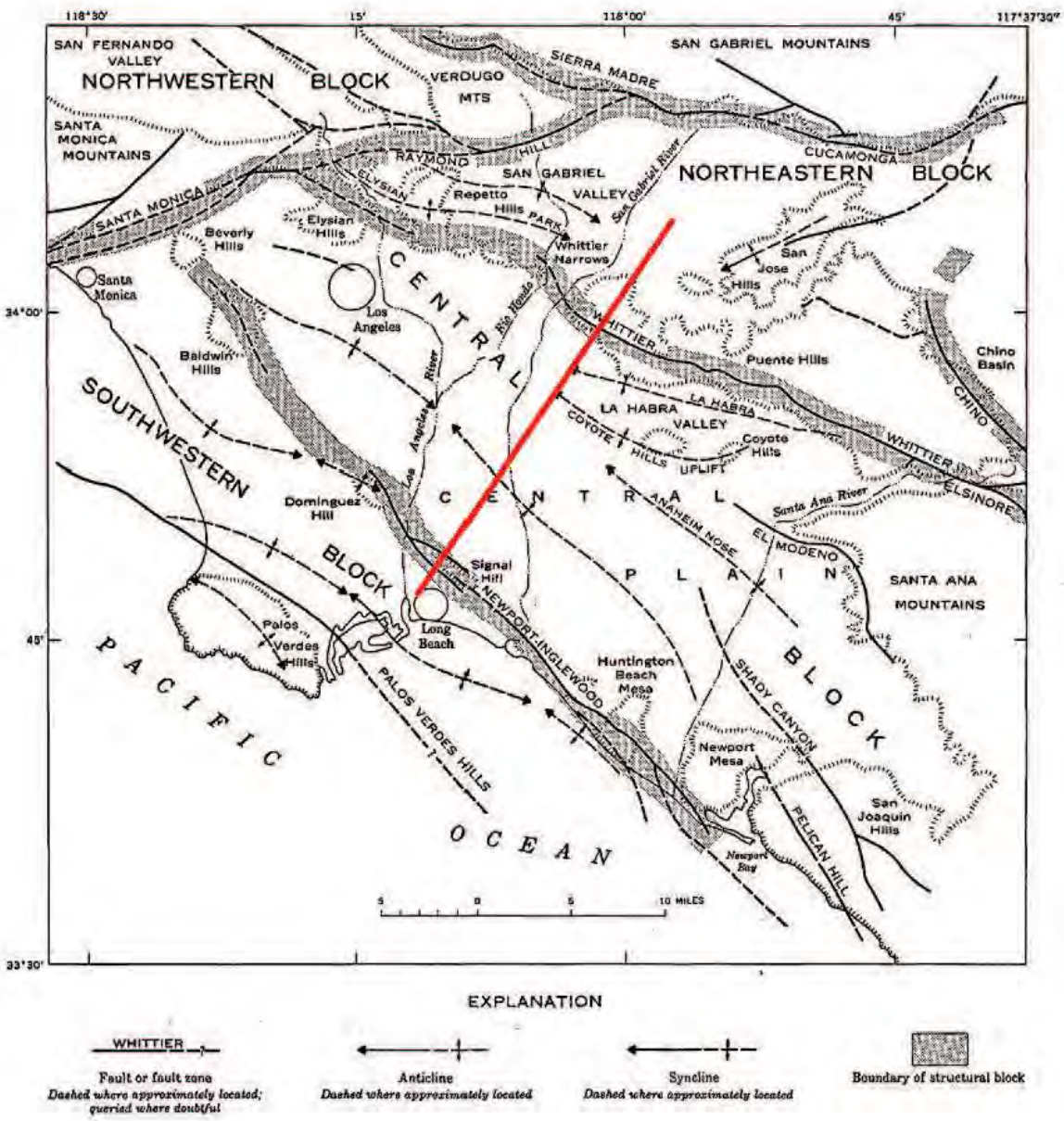

Figure 1.3: *Map of the Los Angeles basin segmented into structural blocks, adapted from Yerkes et al. (1965). The red line corresponds to the transect if the high density temporary network used in this thesis.*

Santa Ana Mountains and San Joaquin Hills. The Los Angeles Basin is best described by the categorization of four structural blocks in Yerkes et al. (1965) and as shown in figure 1.3. The southwestern block runs from Santa Monica at its northwestern point to

Long Beach at its southeastern edge. The majority of this block is offshore, however, the most prominent feature of this block is the Palos Verdes Hills with the Newport-Inglewood deformation zone to the northeast. The northwestern structural block incorporates the Santa Monica Mountains, Verdugo Mountains, and the San Fernando Valley. The Santa Monica Mountains are the result of the middle Miocene deformation. The Santa Monica Mountains are approximately 45 miles long and the northern boundary of the LA basin. The Santa Monica Thrust fault and the Hollywood fault are located at the base of the Santa Monica Mountains. The Central block is wedge shaped, consisting of the Santa Monica Mountains in the northwestern end and the San Joaquin Hills in the southeast, including the prominent Santa Ana Mountains. The dominant structural feature of the Central block is the northwest trending synclinal trough through its center. The axial portion of the trough plunges from depths of 4,000 - 5,000 meters below sea level at its distal end, to 9,500 meters at its deepest point, as indicated by Yerkes et al. (1965). The northeast block of the LA basin is a triangular wedge from northwest to southeast. The wedge is bound by the Repetto Hills and the Puente Hills as described by Yerkes et al. (1965) and Wright (1991).

The surface geology of the Los Angeles basin is comprised of sediments of Quaternary and Miocene age, due to its recent formation as depicted in Jennings et al. (1977), and as shown in figure 1.4. The subsurface geology and structure is as complex as its tectonic history.

The LA basin is underlain primarily by crystalline bedrock and Mesozoic schist as described in Yerkes et al. (1965). Yerkes described the basement material by dividing the basement rock into the structural blocks they correspond to. The ages of the basement ma-

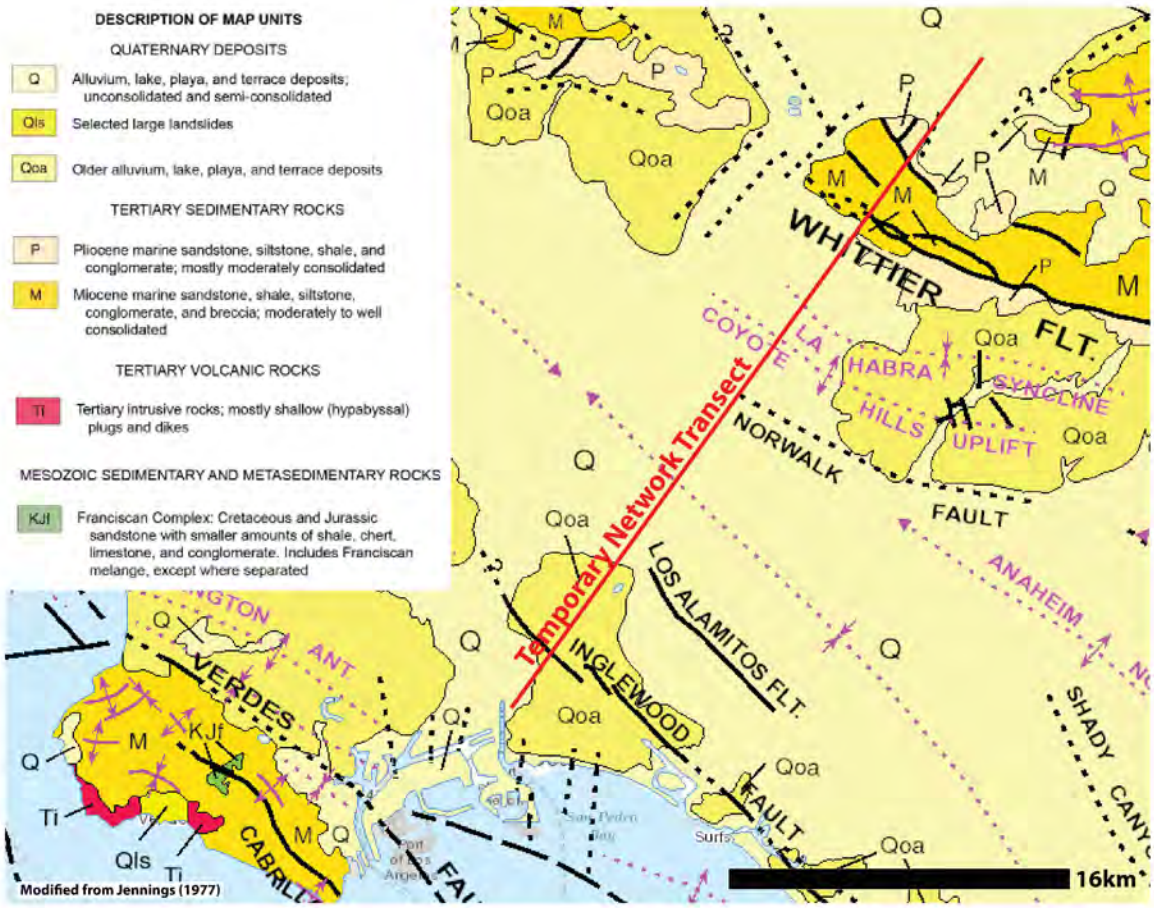

Figure 1.4: *Surface geology map of the Los Angeles basin adapted from Jennings et al. (1977). The red line corresponds to the transect of the high density temporary network used in this thesis.*

terial are constrained by Woodford (1960). Overlying sediments are described in detail by Yerkes et al. (1965). These sediments range in textures from coarse sandstone to shale and fine silt. Interbedded layers are present due to the complicated tectonic environment during deposition as described by Ingersoll & Rumelhart (1999). Sedimentary layer thickness of units described in Yerkes et al. (1965), range from 21 m in thickness for surficial Holocene deposits to upper Miocene siliceous shale and sandstones that are 2600 m thick. Cretaceous, Paleocene, middle Miocene, Pliocene, and middle and lower Pleistocene ages have

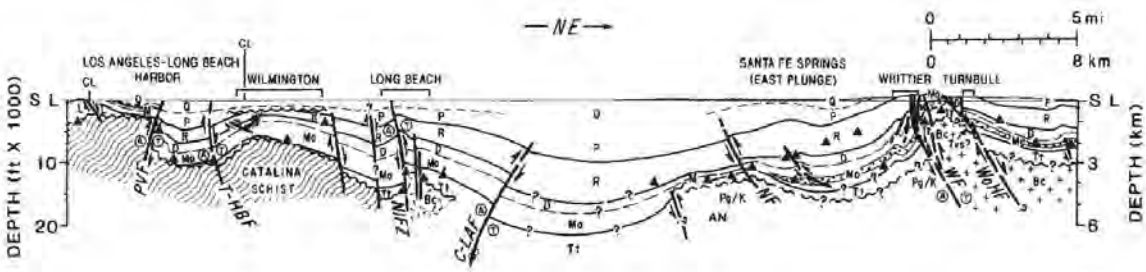

Figure 1.5: *Regional cross section of the LA basin from Wright (1991). This cross section transects the LA basin along the same approximate profile of the temporary array used in this thesis. Solid triangles indicate depth of control wells and "ears" on the triangles indicate the course of deviated wells. Arrows on the faults show vertical slip direction. Circled letters indicate lateral fault motion: A = away from the viewer, T = toward the viewer. NF = Norwalk fault, NIFZ = Newport Inglewood fault zone, C-LAF = Compton - Los Alamitos fault, WF = Whittier fault, and WoHF = Workman Hill fault. Q = Quaternary, P = Pico Formation, R = Repetto Formation, D = Delmontian, Mo = Mohnian, L = Luisian, Tt = Topanga Formation, Pg = Paleogene, K = Cretaceous, and Bc = undifferentiated metamorphic basement complex.*

been constrained through methods of relative age dating of mollusk fossils found in marine sediments throughout the different sedimentary layers by Kleinpell (1938); Wissler (1943); Woodring & Popenoe (1945); Woodring et al. (1946); Kulp et al. (1952), and Popenoe et al. (1960). Notable petroleum bearing sandstone units in the Los Angeles basin are the Mohnian stage (14 Ma) and the Repetto formation (4.5 Ma), the structural contour maps of which serve as an example of the general shape of the basin as shown in figure 1.5 from Wright (1991). These Miocene and Pliocene units are found at depths of 4,900 m - 7,300 m depth in the central basin. They are composed of repeating interbedded fine to coarse clastic sediments that thicken southward as described by Yerkes et al. (1965). Structural

traps were formed in the early Pliocene because of the northwestern basin extension.

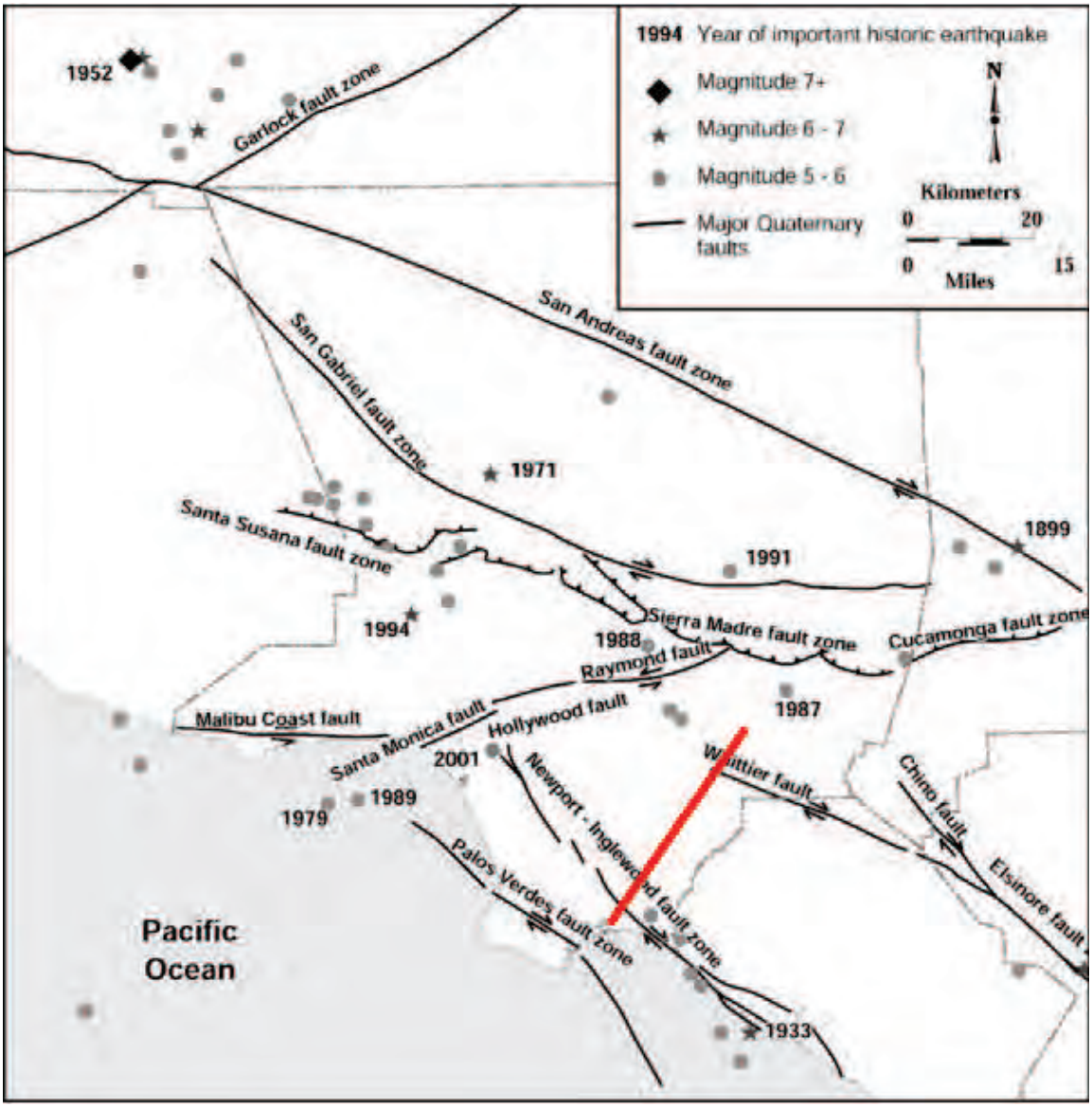

Figure 1.6: *Map of the faults in and surrounding the Los Angeles basin with historical earthquakes, adapted from Bilodeau et al. (2007). The red line corresponds to the transect of the high density temporary network used in this thesis.*

Seismic hazard is a significant issue for the population centers inside the LA basin. Although the San Andreas is at a distance of more than 50 km from downtown Los Angeles,

the fault is capable of generating a magnitude 8 earthquake that would cause significant damage to life and property for those residing in the LA basin. The San Andreas fault is a right-lateral strike-slip fault between the North American and Pacific plate and has an average slip-rate of 48 - 52 mm/yr. Its southern section has not experienced a significant earthquake since the 1857 Fort Tejon earthquake (Lindh, 1983). Thus, the southern section of the San Andreas fault will likely rupture and is a very serious threat as calculated in Lindh (1983) and Olsen et al. (2009).

However, the seismic hazard of the San Andreas is not the only seismic hazard associated with the LA basin. Several faults within the LA basin are active and have been shown to produce large magnitude earthquakes. The left step in the right lateral San Andreas fault results in the compression of the LA basin. The product of this compression is a series of low angle thrust faults. A few examples of the many faults discovered in the LA basin are depicted in figure 1.6: the Puente Hills thrust fault, Newport Inglewood fault zone, Compton Los Alamitos fault, Whittier fault, and the Palos Verdes fault. The Whittier and Palos Verdes faults define the edge of the LA basin. The Puente Hills thrust fault is a northeast dipping blind thrust fault that extends for 40 - 50 km in length from Orange County to Beverly Hills and terminates upward at a depth of 3 km. Based on borehole data, the Puente Hills thrust experienced 4 large Holocene earthquakes with moment magnitudes between 7.2 - 7.5 as evidenced by Dolan et al. (2003). The Newport Inglewood fault zone is marked by en echelon anticlinal folds and faults as discussed by Eaton (1923); Ferguson & Willis (1924), and Moody & Hill (1956). Surface traces strike roughly N45°W for approximately 64 km from Culver City to Newport Beach. The Newport Inglewood fault zone is known to

be an active fault zone from the M_L 4.9 Inglewood 1920 earthquake and the M_L 6.3 Long Beach 1933 earthquake. An element of the Newport Inglewood fault zone is the Compton Los Alamitos fault, as coined by Wright (1991) from combining McMurdie (1973) and Ziony et al. (1974) interpretations of the same previously unknown fault discovered from microseismicity.

Two boundary fault structures in the LA basin are the Palos Verdes fault and the Whittier fault. The Palos Verdes fault is the southwestern boundary structure of the LA basin. The Whittier fault is the northeastern boundary structure of the LA basin. The Palos Verdes fault is a right-lateral fault. The Whittier fault strikes at approximately S60°E for a length of 40 km. Surface measurements of the Whittier fault by Yerkes et al. (1965) determined the fault to be a north dipping reverse right oblique fault.

Seismic hazard within the LA basin will always be a concern. These hazards may be generated from faults nearby or within the basin. It is important to further understand and determine characteristics that play a key role in ground motion amplification.

1.1.2 LA basin subsurface models

The LA basin depth is constrained by its tectonic history and structural setting. Ground and structural block displacement from active and inactive faults are the driving mechanism that controls the basin depth. There have been several investigations such as McCulloh (1960); Yerkes et al. (1965); Hauksson & Haase (1997) and Magistrale et al. (1996) to constrain the deepest portion of the LA basin using well data, geological data, seismic reflection, and travel time tomography. One way to determine the depth of the LA basin

is to use data from petroleum exploration as McCulloh (1960) and Yerkes et al. (1965) have demonstrated. McCulloh (1960) used surface geology, well data, and reflection seismic data to produce a detailed "floor of the basin". Although the source of the detail for McCullohs (1960) LA basin model is not well described, it is consistent with horizons described by Wright (1991). Yerkes et al. (1965) used petroleum company data to determine a LA basin model. This model is 9 - 10 km deep at its deepest point as shown in figure 1.7 and figure 1.8. A second technique for producing a LA basin model is to invert for a velocity model using body wave travel time measurements as described by Magistrale et al. (1996) and Hauksson & Haase (1997). Magistrale et al. (1996) also incorporated geologic information on surface geology and depth to basement to construct a basin model. Hauksson & Haase (1997) use local earthquake events for body wave travel times. These travel times were inverted for three-dimensional P-waves and S-wave velocity models. The LA basin depth from Hauksson & Haase (1997) is approximately 8 - 12 km. Collaborative works to create a large comprehensive basin velocity model were performed by Plesch et al. (2009). This velocity model is the compilation of both industry exploration data, as well as academic research data. Recently, Ma (2016) used receiver functions to determine basin depth using the collaborative model as their starting model. The deepest portion of the LA basin as determined by Ma (2016) is 8 km. All of the aforementioned models are similar in terms of their large scale features, with the basin bowl-shaped structure, shallow at the edges and deep in the central portion. However, details of these LA basin models differ.

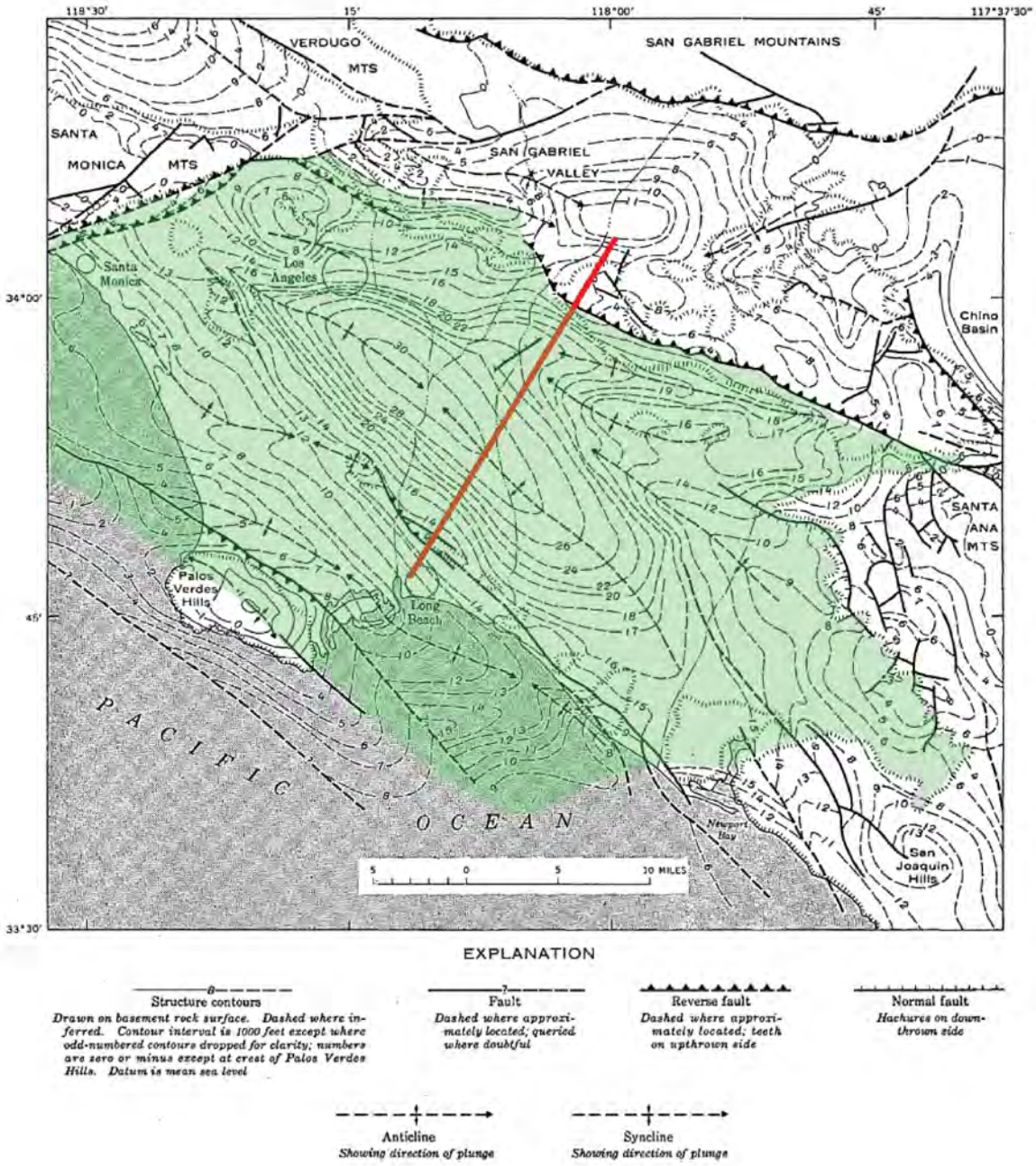

Figure 1.7: *Los Angeles basin basement depth map adapted from Yerkes et al. (1965). The LA basin is colored in green. The red line corresponds to the high density temporary network used in this investigation. The contours are in thousands of feet.*

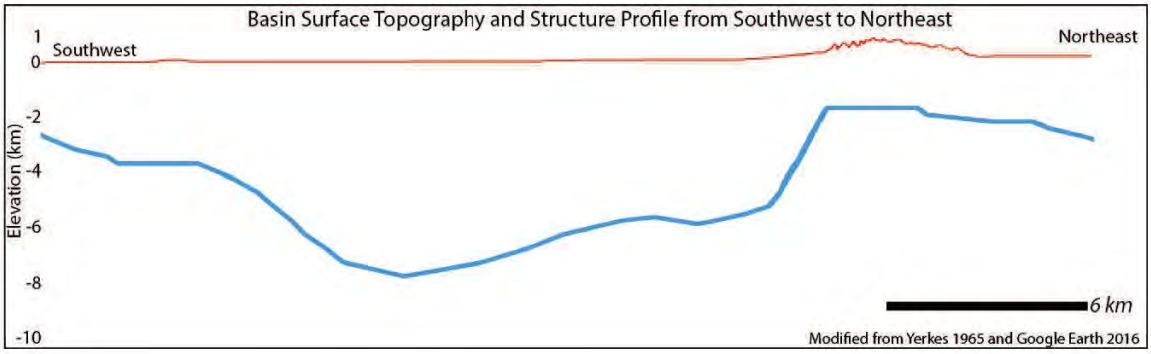

Figure 1.8: *Basement depth cross section of the Los Angeles basin along the high density temporary array transect used in this thesis. The blue line corresponds to the basin basement adapted from Yerkes et al. (1965) and the red line corresponds to the basin surface topography adapted from Google Earth (2015).*

1.2 Site Effects

It is well established that sedimentary basins, such as the Los Angeles basin, can significantly amplify earthquake ground motion and increase its duration in comparison to a hard rock site. Seismic ground motion traveling from hard rock to soft sediment will decrease in velocity and increase in amplitude due to the change in rock properties. This increase in amplitude is an important factor in determining the intensity of ground shaking during a seismic event. Ground motion amplitude will vary in different locations within the basin. This may be attributed to differences in lithology and depth of the basin, and, more generally, to site effects.

Site effects were initially studied following the 1854 Tokyo earthquake in Japan. Studies conducted by Imamura (1913) involved surveying and mapping of urban damage patterns from amplified ground motion. Site conditions vary greatly over a short lateral distance as reaffirmed by Nakamura (1989); Louie (2006) and Louie (2007), leading to mi-

crozonation. Investigation of microzonation will improve seismic hazard maps. Mihalic et al. (2011) provide an overview of the strengths and limitations of seismic microzonation.

There is an elevated interest for the mitigation of destruction and urban damage in the Los Angeles basin that will occur from a major seismic event. Ground motion is affected by factors such as source, path, and site effects. Seismic macrozonation at a regional scale aids in geotechnical designs for hazard mitigation and building designs. However, it is important to consider the effects of the subsurface locally through local site effects. These site effects have been shown to vary on a scale smaller than regional scale by Mihalic et al. (2011); Parolai et al. (2002) and Mahdyiar (2002). Spatial representation of microzonation has proven to be difficult to resolve and has been estimated by using surface geology as a proxy for S-wave velocity in the top 30 m of soil, V_s30, as a proxy for basin amplification in Wills et al. (2000). There are inherent problems with the use of V_s30 since its value is measured for engineering applications to represent V_s of the entire soil column. Studies have shown that V_s30 measurements can vary by more than 30% over a short distance as described in Thelen et al. (2006). Microzonation studies improve land use management, city planning, and resolution of the regional site effect maps.

Understanding site effects is key in furthering the knowledge base of ground motion and for the reduction of earthquake induced damages. Site characteristics are influenced by the type of sediment, thickness and the location of the sedimentary units and may be characterized by the fundamental frequency and ground motion amplification.

There are three regulatory methods described in TC4-ISSMGE (1999) for determining zonation for local site effects. The first method uses existing information such as surface

geology maps to compile site effects. Surface geology has been empirically shown in investigations such as Wills et al. (2000) to correlate with seismic intensities. Thus, surface geologic units may be used to estimate and classify local site effects. The second method uses both geotechnical investigations such as the Cone Penetration Test (CPT), Standard Cone Penetration Test (SPT), and Soil borings. It is preferable that geotechnical studies investigate to the depth of bedrock and supplement their findings with the first method. However, geotechnical methods are invasive, adversely impact the environment, may not be available for all locations, and cannot drill to the bottom of the basin. Geotechnical methods also mainly focus on basic amplification, not effects such as resonance. Geophysical studies such as microtremor investigation are required for complete understanding of site effects, since standard geotechnical studies will only yield insufficient amount of subsurface data. The third method uses numerical 1-D, 2-D, and 3-D basin modeling to estimate site effects.

1.2.1 Resonance

Fundamental frequency is a parameter that describes the resonance of the soil column for site response. Resonance is the phenomenon in which the amplitude of a system may be dramatically increased as a cyclical force is applied at a specific frequency. The frequency of the cyclical force at which this dramatic increase occurs is known as the natural frequency, fundamental frequency, or resonance frequency of the system. When this internal resonance frequency matches an external applied frequency, the system is considered to be in resonance. A system in resonance responds with an increasing amplitude to the

driving force. In harmonics, the first harmonic of the natural frequency is half the standing wavelength, where higher order harmonics are multiples of the fundamental frequency. The occurrence of resonance in a system may result in an increase of oscillation amplitudes to tremendous magnitudes which, in a rigid body, may be violent and could result in a catastrophic system failure.

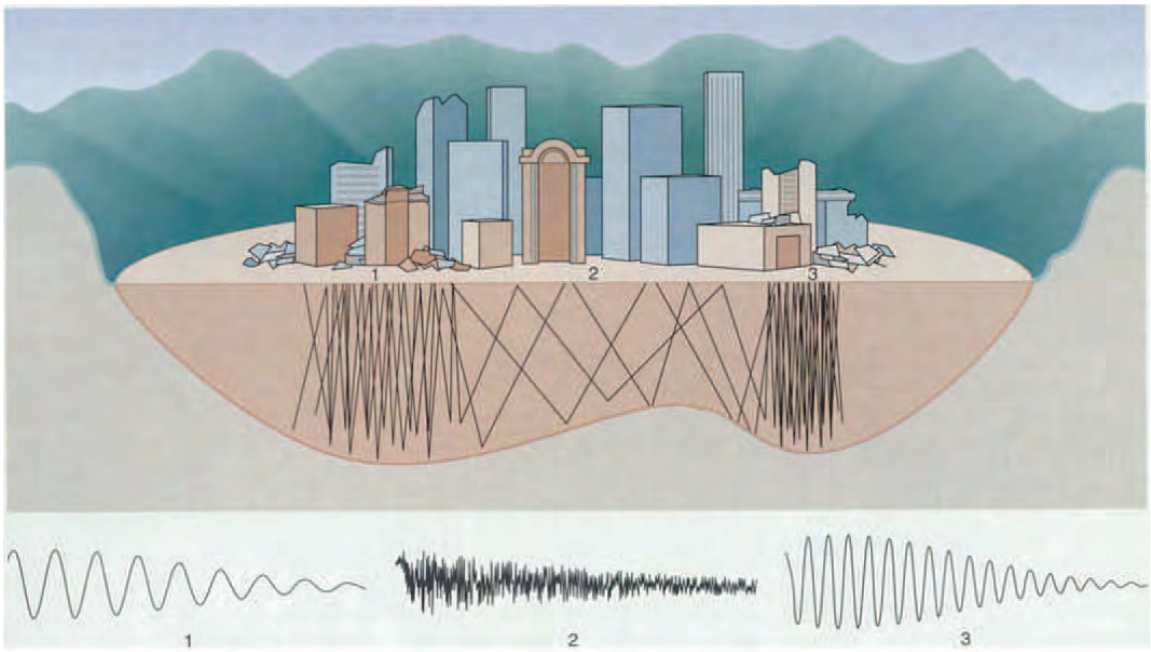

Figure 1.9: *Illustration of basin resonance from J. a. Rial et al. (1992) showing how seismic waves reflected off the basement material and basin surface create destructive basin resonance.*

Basin sediment resonance as illustrated in figure 1.9 is determined by the shape, size, mass, rigidity, and velocity contrast of the basin, described by Bard & Bouchon (1985) and J. a. Rial et al. (1992). Highest amplification is typically located at the center and mid-edge as evidenced by Kagami et al. (1982). In site response characterization studies, the fundamental frequency and resonance may be determined through various methods.

An empirical method in determining the fundamental frequency is the analysis of ambient noise data. Determining the fundamental frequency for site response is vital for structural damage mitigation from the propagation of strong ground motion to a structure, as expressed in Hall & Beck (1986); Brady et al. (1988) and Graves (1995). The Los Angeles basin is a prime candidate for examining its fundamental frequency due to its high population density, high-rise buildings, and risk of ground motion amplification. Ground motion in resonance increases its destructive powers in the form of amplification and possible increase in duration. The level of amplification may be described by comparing the ground motion measured at a particular site to that measured at a hardrock site in hardrock to the soft sediment. This gives us a relative amplification value and this description has been used in investigations such as Gutenberg (1957); Lermo & Chavez - Garcia (1994).

1.3 Basin response case studies

Basin resonance and ground motion amplification have been observed in numerous recent earthquakes. Some prominent case studies are the Mexico City earthquake, Whittier Narrows earthquake, and the Northridge earthquake.

Mexico City 1985

The 1985 M8.1 Michoacan earthquake is the textbook example of basin resonance and engineering considerations of potential seismic motion in building design. The earthquake occurred off the coast of Michoacan and was the result of slip along a shallowly dipping interplate subduction fault striking parallel to the Mid-America trench as noted by Beck &

Hall (1986). Nearly 300 km away, Mexico city experienced ground motions costing and affecting several thousands of lives. Approximately one thousand buildings were damaged by the ground motion as described by Hall & Beck (1986) and Beck & Hall (1986). Later examination by Eissler et al. (1986) and Flores-Estrella et al. (2007) established that the primary cause of the damage was the amplification of ground motion and the double resonance of tall buildings.

Site response investigations determined basin amplification and resonance were the main culprits of the destruction of tall buildings while smaller buildings were unaffected. Mexico City is located on lake bed sediments that resonate at a 2 second period and thus amplify ground motion at that period. The 2 second ground motion period resonated with structures 6 - 15 stories high as described in Hall & Beck (1986). Amplitude spectral ratio determined from station recordings of the 1985 event located on the Mexico City lake-bed sediments display a fundamental period of approximately 2 seconds as evidenced by the Mexico City spectral ratio in Franco-Villafañe et al. (2011).

Whittier 1987

The 1987 M5.9 Whittier earthquake occurred 15 km to the west of Whittier in downtown Los Angeles. Initial investigations concluded that this earthquake did not occur on the Whittier fault, but some other blind fault described in Davis et al. (1989). Although the epicentral distance from the earthquake is 15 km, part of Whittier experienced the highest ground acceleration as expressed in Brady et al. (1988) and Etheredge et al. (1987). Investigations by Kawase & Aki (1990) of building damage pattern distribution led to fur-

ther conclusions that basin edge effects were responsible, where ground motion energy is trapped and reverberated off the edge of the basin. Hruby & Beresnev's (2003) computational models using the Whittier earthquake data and a synthetic rock site also supported the importance of basin edge amplification. Simulation of wave propagation for the earthquake using a 3-D finite difference method exhibited a oscillation of 4 seconds confirming the basin edge effect (Yomogida & Etgen, 1993).

Northridge 1994

The 1994 Northridge M6.7 earthquake caused extensive structural damages to the city of Los Angeles approximately 25 km south of the epicenter as described by Graves (1995). The damage from the earthquake was attributed to basin amplification. Nonlinear ground acceleration was observed at seismometers overlying sedimentary units while, comparatively, non-linearity was not observed at hard rock locations as discussed by Beresnev et al. (1998). 2-D and 3-D numerical simulation modeling by Graves (1995); Hruby & Beresnev (2003) and Olsen (2000) of this earthquake showed similar basin ground motion amplification patterns as the earthquake data.

1.4 Previous site response studies

Site response has been observed and investigated throughout the world using different methods and approaches.

1.4.1 Site response in the LA basin

Site response in the Los Angeles basin has been investigated in the past through the analysis of earthquake, active and passive source data and numerical modeling. Rogers et al. (1979, 1985) investigated the LA basin region using peak ground velocities from a nuclear source. They found that one of the geotechnical factors that has the strongest influence on site response across the full period range is depth to basement rock. Active source experiments are costly and insufficient earthquake based waveform data is available for many areas and time periods. Therefore, other approaches must be considered.

Kagami et al. (1982) analyzed microtremor data for the characterization of the Los Angeles basins deep sediments and concluded that there was no clear systematic change of predominant period in relation to the thickness of soil deposit. In contrast to that observation, the spectral amplitude of the long-period microtremors was found to increase systematically with increase of thickness of soil deposits. Interest in characterizing the Los Angeles basin by passive source continued with the Kohler et al. (2000) 1997 Los Angeles Basin Passive Seismic Experiment (LABPSE). Husker et al. (2006) analyzed the LABPSE data to invert the spectra of P and S body waves for site effects, attenuation, and corner frequency. A subsurface structure was determined for the northern boundary. Observations of S-wave propagation also showed strong basin edge effects. Husker et al. (2006) found anomalous seismic amplitudes and attributed these to a caustic.

The advancements in computer technology in the past several decades have aided in LA basin site characterization research, leading to detailed numerical modeling. Wald & Graves (1998) used several past investigations such as the three seismic response models by

Graves (1996); Hauksson & Haase (1997) and Magistrale et al. (1996) and compared them with measurements of strong ground motion from 1992 Landers earthquake. None of the models matched the observed amplification in the basin. Some of the seismic amplification of the deepest portion of the LA basin was best characterized by Magistrale et al.'s (1996) velocity structure. The spectral peak of the LA basin based on the Magistrale et al. (1996) model is approximately 7 seconds. However, only the Graves's (1996) model accurately predicted the recorded spectral peak period of 10 seconds.

Additional numerical modeling of the LA basin is performed by Olsen (2000); Denolle (2014) and Ma (2016). Olsen (2000) used nine theoretical earthquake scenarios to compute as input to three-dimensional modeling to predict LA basin amplification. Each of the scenarios exhibited a concentration of prolonged SH-wave amplification in the Los Angeles basin. Further investigation by Denolle (2014) on LA basin sedimentary amplification from a virtual M7+ earthquake predicted a large amplitude 3 - 10 second long period ground motion for a M7+ earthquake. More recent investigations of the LA basin by Ma (2016); Ma et al. (2016) and Ma & Clayton (2016) used receiver functions and ambient noise tomography to estimate a basin and Moho depth, and Love and Rayleigh wave inversions to generate a velocity model for the basin, where the basin is 8 km deep and the Moho is 25 km deep under the basin.

1.4.2 Other basin site response investigations

Ground motion amplification has also been observed and modeled in other basins using various methods based on microtremor and earthquake data, as well as theoretical

approaches. These methods include, but are not limited to spectral analysis, calculation of response spectra, and examinations of different components of the full wavefield. Kagami et al. (1986) conducted a spectral analysis of recorded microtremor in deep sediments of the San Fernando valley as a continuation study of the Kagami et al.'s (1982) investigation in a different setting. The San Fernando Valley was chosen in this study for its proximity to hard rock locations as well as deep basin sediments. The conclusions of this study reconfirm the observations of microtremor having a larger amplitude in sediments as compared to basement rock reference sites and thus exhibiting higher relative amplification.

Site response studies are useful for engineering practices. The response spectrum approach is an effective method for characterizing the behavior of a building or soil structure, provided a ground motion event. Ashford et al. (2000) used five strong ground motion events as input for a response spectrum analysis applied to the Bangkok basin. The response spectrum resulted in similar amplification values as amplification values measured from the Mexico City 1985 earthquake, suggesting the Bangkok basin sediments have similar ground motion amplification properties as the Mexico City basin.

A different approach for site characterization would be to analyze the spectral ratio of different components of the full wavefield. Site characteristics were obtained from the spectral ratio of the P-wave, S-wave, coda, and microtemor and compared in Satoh et al. (2001). The investigation concluded that the microtremor Horizontal to Vertical Spectral Ratio (HVSR), a passive method for site response analysis, peak frequencies below 1 Hz with an amplitude greater than 3 are well correlated with the HVSR spectral ratio of S-waves.

1.4.3 HVSR studies in basins

A passive method increasing in popularity for site response analysis is the HVSR method, also commonly referred to as the Nakamura method. The HVSR method is effective to determine site response by removing source effects by dividing the horizontal component of ambient noise by the vertical component. This method has been applied to basins located in countries such as Mexico, Turkey, and Japan, to determine fundamental frequency, amplification and basin depth. The HVSR method has been repeatedly evaluated against other established geophysical methods to test for method reliability. In the Mexico City basin, Lermo & Chavez - Garcia (1994) used the HVSR approach to evaluate site response and ground motion amplification. The authors compared three approaches and determined the HVSR approach to be the most accurate of the three methods for microtremor analysis in the Mexico City basin. The HVSR method was also applied to the Mexican Volcanic Belt (MVB) for a site response investigation by Clemente-Chavez et al. (2014). This experiment determined an amplification factor of 10 in the Mexico City basin.

In their investigation of the Izmit, Turkey basin, Özalaybey et al. (2011) recorded both HVSR and gravimetric measurements to characterize the sediment packet thickness. The results of this investigation show the basin as a very thick packet of low velocity sediment over basement rock, forming a sharp impedance contrast. Measurements from the HVSR method were used to determine sediment thickness and these results were compared with basin depth results from the gravity measurements. Agreement between the two methods for determining basin depth helped confirm the reliability of the HVSR method for

determining the depth to sediment bedrock interface.

Zhao et al. (2000) focused on the analysis of the HVSR method for robustness superiority over other techniques. They compared the spectral ratio of horizontal components (HH spectral ratio), HVSR, and power spectra in the Kansai and Kushiro district. HVSR spectral peaks coincide with peak frequencies of seismic motion, while power spectra did not always agree. Therefore, the HVSR method was determined to be superior in determining site characteristics over the power spectra approach. The establishment of the HVSR method has allowed the method to be used for interferometry applications. Uebayashi et al. (2008) applied the microtremor HVSR method in the Osaka basin to attempt to image the irregular subsurface basement structure. This experiment showed an agreement with existing velocity profile structures in areas where the basin basement inclination is shallow. This use of the HVSR method is further investigated by Matsushima et al. (2011). They adapted the method to investigate azimuthal variations in the HVSR method measurements on the Uji Campus of Kyoto University of Japan and found that the maximum differences in peak amplitude for two orthogonal components for the HVSR method corresponded to the azimuth parallel to the irregular subsurface structure of the Obaku fault plane. The Uji Campus investigation concluded that a 3-D finite-difference simulation for a 3D model of the local basin successfully simulated the differences between the orthogonal horizontal HVSR spectral graph.

Chapter 2

Methodology

In this chapter we discuss the dense temporary array of broadband seismometers that provided the data-set used in this research, the methodology of the data analysis, and show an example of standardized data processing.

2.1 Los Angeles Syncline Seismic Interferometry Experiment (LASSIE)

The Los Angeles Syncline Seismic Interferometry Experiment (LASSIE) is a collaborative experiment that involved the installation of a high density array of broadband seismometers across the LA basin. The collaborative efforts of LASSIE are from academia: California Institute of Technology (Caltech), University of California, Los Angeles (UCLA), and California State Polytechnic University, Pomona (Cal Poly Pomona), government: United States Geological Survey (USGS), and industry: NodalSeismic, Signal Hill Petroleum, and California Resources Corporation. Subsets of the total of 73 broadband seismometers

of the LASSIE array were deployed and maintained by each collaborator and had data collected continuously for one month at a minimum sampling rate of 100 samples per second. The author of this thesis co-led the installation effort for 8 of the 73 seismometers, which constituted the Cal Poly Pomona portion of the network, with the assistance of fellow graduate and undergraduate students. There are two primary components to the LASSIE network. One component of the LASSIE array is the LA basin transect from Long Beach northeastward towards the City of Industry, north of the Puente Hills at an approximate station spacing of 1 km as shown in figure 2.1. The LA basin transect is approximately orthogonal to the horizontal major axis of the basin. The second component of the array is the Long Beach cluster of 29 seismometers over an area of 50 km^2.

The surface geology at the location of most stations is Quarternary alluvium. A few stations that were installed on the basin edge in the Puente Hills, are located on Tertiary sedimentary rock as shown in the geological map of figure 1.4. LASSIE stations and select Southern California Seismic Network (SCSN) stations are displayed on a topographic map of the LA basin and surrounding areas in figure 2.1. SCSN is a permanent network of short period stations, modern broadband stations, and accelerometers that have been continuously monitoring earthquakes since the 1920s, although most SCSN stations have only been operational since the 1980's. SCSN stations were selected based on their proximity to the LASSIE array, with the exception of SCSN station USC which was selected based on its high quality, vault style, installation and location within the LA basin.

We collect continuous full waveform data from both the LASSIE array and nearby SCSN stations via the Seismogram Transfer Program, created by the Southern California

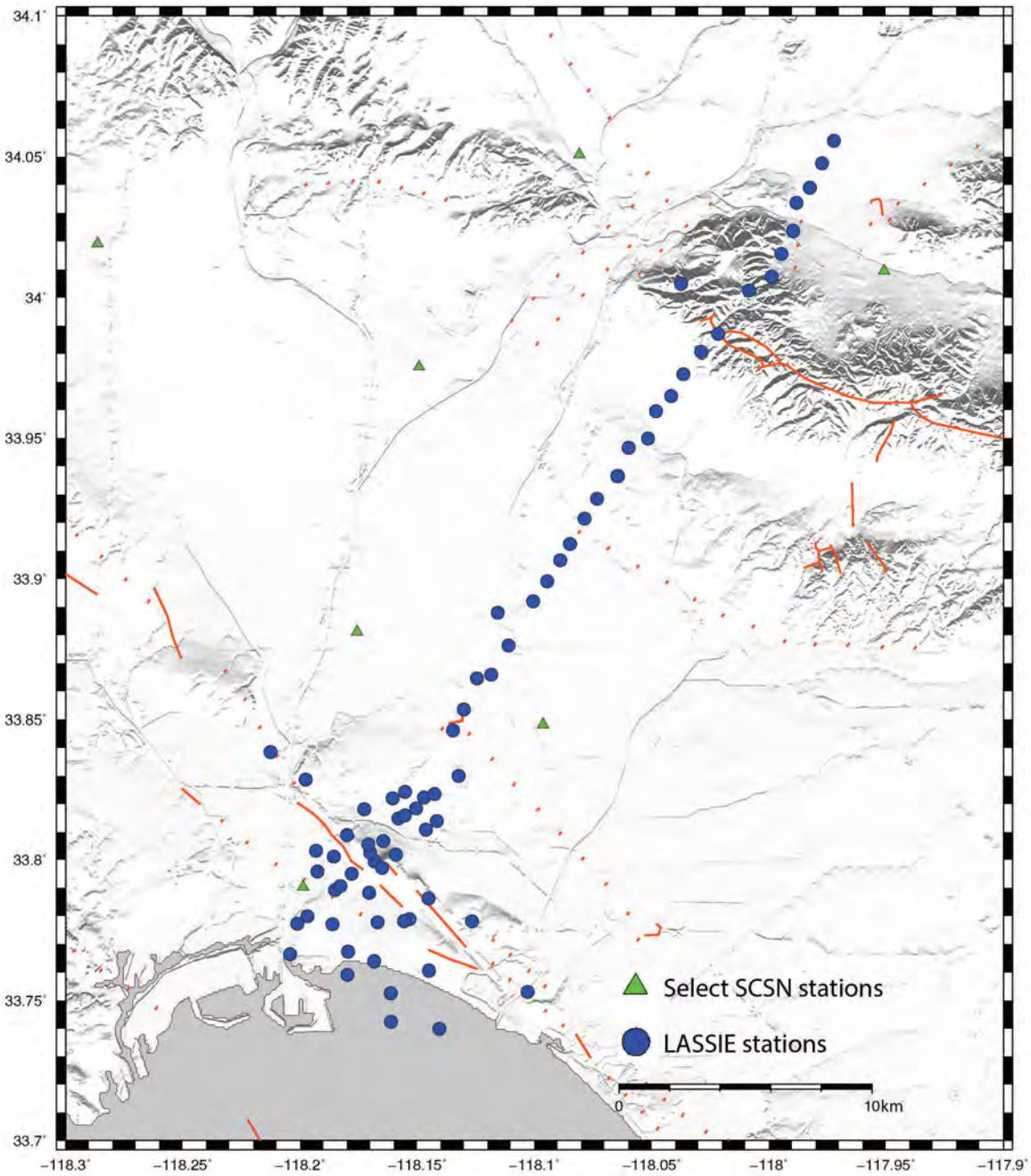

Figure 2.1: *Topographic map of LASSIE stations, depicted as blue circles, and select SCSN stations, depicted as green triangles. A line of LASSIE stations transects the LA basin northeastward from Long Beach, terminating north of the Puente Hills. Quaternary faults are highlighted in orange.*

Earthquake Data Center, Hafner & Clayton (2001). STP is a client side program that allows users to retrieve waveform data from the Southern California Earthquake Data Center. Continuous full waveform data contains both ambient noise data as well as earthquake data from local and teleseismic events. We apply a non-invasive method to the ambient noise three component waveform data collected from the LASSIE array for a site response investigation.

2.2 Analysis approach: Horizontal to Vertical Spectral Ratio (HVSR)

The method we use for data analysis is the Horizontal to Vertical Spectral Ratio (HVSR) approach developed by Nakamura (1989). The HVSR approach is applied to ambient noise and generates a Fourier spectral ratio of amplitude versus frequency. The HVSR method divides the horizontal component of noise to the vertical component to remove source effects as shown in figure 2.2. The spectral ratio is calculated by taking the Fourier transform (Welch, 1967) of the ambient noise recordings. This resulting function shows how the amplitude of motion is distributed with respect to frequency. A narrow spectral peak at a particular frequency (range) implies that a large component of the energy of motion falls within that frequency range.

Lachet & Bard (1994) investigated the HVSR approach on ambient noise recordings to clarify if this method reflected characteristics of the site as opposed to the source. Their study concluded the HVSR approach was able to clearly show the HVSR peak of a sed-

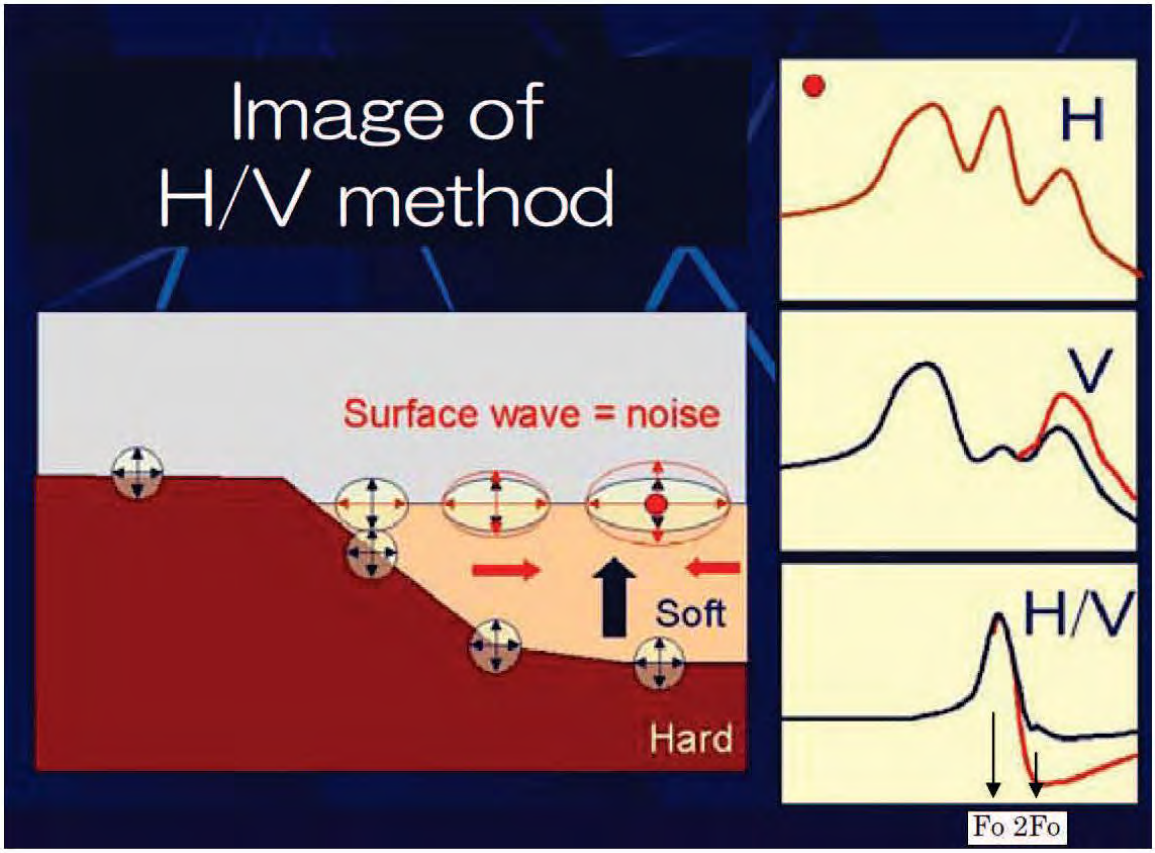

Figure 2.2: *Cartoon of the HVSR method, where Rayleigh wave ellipticity of the basement and ground surface is shown in the left panel. The Fourier transform of the horizontal (top) and vertical (center) component, and the resulting HVSR (bottom) are shown on the right. The image is from Nakamura (2008).*

imentary site independent of source effects. The HVSR analysis is considered to remove the source effect by dividing the horizontal by the vertical component as described by Nakamura (1989); Lachet & Bard (1994); Bard (1999); Nakamura (2000); Panou et al. (2005) and Nakamura (2008).

Ambient noise

Ambient noise is known by many synonyms: microtremor, ambient vibration, seismic noise, ambient wavefield, etc. Ambient noise is produced by random sources, a combination of both natural and anthropic signals as categorized by Gutenberg (1958), and contains both surface and body waves. Natural signals, microseisms, originate from the ocean and are predominantly Rayleigh waves as theorized by Longuet-Higgins (1950), while anthropic signals which originate from industry or human activity are mainly Love and Rayleigh waves as categorized by Gutenberg (1958); Asten (1978) and SESAME WP12 (2004). Typically, the boundary between microseisms and anthropic signals is at the 1 Hz frequency as suggested by various authors (e.g., Gutenberg, 1958; Asten, 1978; Frantti et al., 1962) and Frantti (1963). However, Seo (1997) found the boundary between microseisms and anthropic signals can be at a lower frequency in a deep and soft basin. Microseisms are generated by ocean wave energy coupling with the earth and are commonly observed in ambient noise data by a primary peak at 0.07 Hz and secondary peak at 0.15 Hz as discussed in Longuet-Higgins (1950). According to Bonnefoy-Claudet et al. (2004) low frequencies are predominately fundamental modes of Rayleigh waves, while at higher energies, Love waves begin to have a higher proportion.

2.2.1 The development of HVSR

The HVSR approach is an empirical technique for determining site characteristics and has been shown to be effective by comparing its results with the results of various other approaches as described in Zhao et al. (2000); Mucciarelli et al. (2003); Bard et al. (2004);

Koller et al. (2004); Bard et al. (2005) and Guillier et al. (2007). There are various ways to explain the HVSR method. Initially proposed by Nogoshi & Igarashi (1971) and developed by Nakamura (1989), HVSR assumes the ambient noise field to be composed of S and Rayleigh waves. Later, the HVSR approach was theoretically substantiated for the the fundamental mode of a Rayleigh wave by Lachet & Bard (1994); Konno & Ohmachi (1998) and Bard (1999). Authors throughout the years have attempted to explain the theory behind the HVSR approach. For example, Bard et al. (2004) explained the HVSR theory based on the primary peaks of the spectral graphs referring to the ellipticity of the Rayleigh wave. Also, Arai & Tokimatsu (2000) suggested the frequencies in the HVSR approach are controlled by Rayleigh waves and the amplitudes are controlled by Love waves. More recently, the HVSR analysis was also verified based on the diffuse field, developed by Sánchez-Sesma et al. (2011).

Reliability of the HVSR approach

The HVSR approach has been popular for site response investigations due to its ease of use, low cost, and flexibility in the use of data that is not dependent on strong ground motion or an active source. Ambient noise HVSR studies have been conducted extensively and compared for reliability against other methods, as discussed by Zhao et al. (2000); Mucciarelli et al. (2003); Bard et al. (2004); Koller et al. (2004); Bard et al. (2005) and Guillier et al. (2007). Nakamura (1989); Koller et al. (2004); Lachet & Bard (1994) and Guillier et al. (2007) have shown that the HVSR spectral peak frequency represents the fundamental frequency of the site soil column. This has been confirmed by later studies

which tested the accuracy and reliability of the HVSR approach, as described in papers such as Ducellier et al. (2013); Cara et al. (2010); Nakamura (2008); Guillier et al. (2007) and Parolai et al. (2004). Further investigation by SESAME WP12 (2004) and Bard & SESAME Participants (2004) in the Site Effects Assessment Using Ambient Excitation project (SESAME) compared the ambient noise HVSR results with those from earthquake-based HVSR analysis and these results were further verified in Bard et al. (2004) and Bard et al. (2005). The primary objectives of the SESAME project were to better understand the physical basis of the HVSR approach, determine its purpose in site response, and propose guidelines for correct analysis. As shown in figure 2.3, the SESAME project demonstrated a strong linear correlation between the spectral peak frequency determined through ambient noise HVSR and those determined at the same site through Standard Spectral Ratio (SPR) measurements from earthquake data. This result clearly demonstrates that ambient noise HVSR results for the spectral ratio peak frequency may be interpreted as indicating the expected peak frequency in case of strong ground motion due to earthquakes. Based on this SESAME frequency comparison and investigations mentioned earlier, we will refer to the peak frequency measured from the HVSR graph as the site fundamental frequency in this thesis.

The amplitude of the spectral ratio has been used by some authors as a representation of amplification relative to hard rock site as in for example, Nakamura (1989); Lachet & Bard (1994); Siddiqqi & Atkinson (2002); Theodulidis et al. (2004); Bard & SESAME Participants (2004) and

Thus, the HVSR method is a simple and effective technique for determining the first

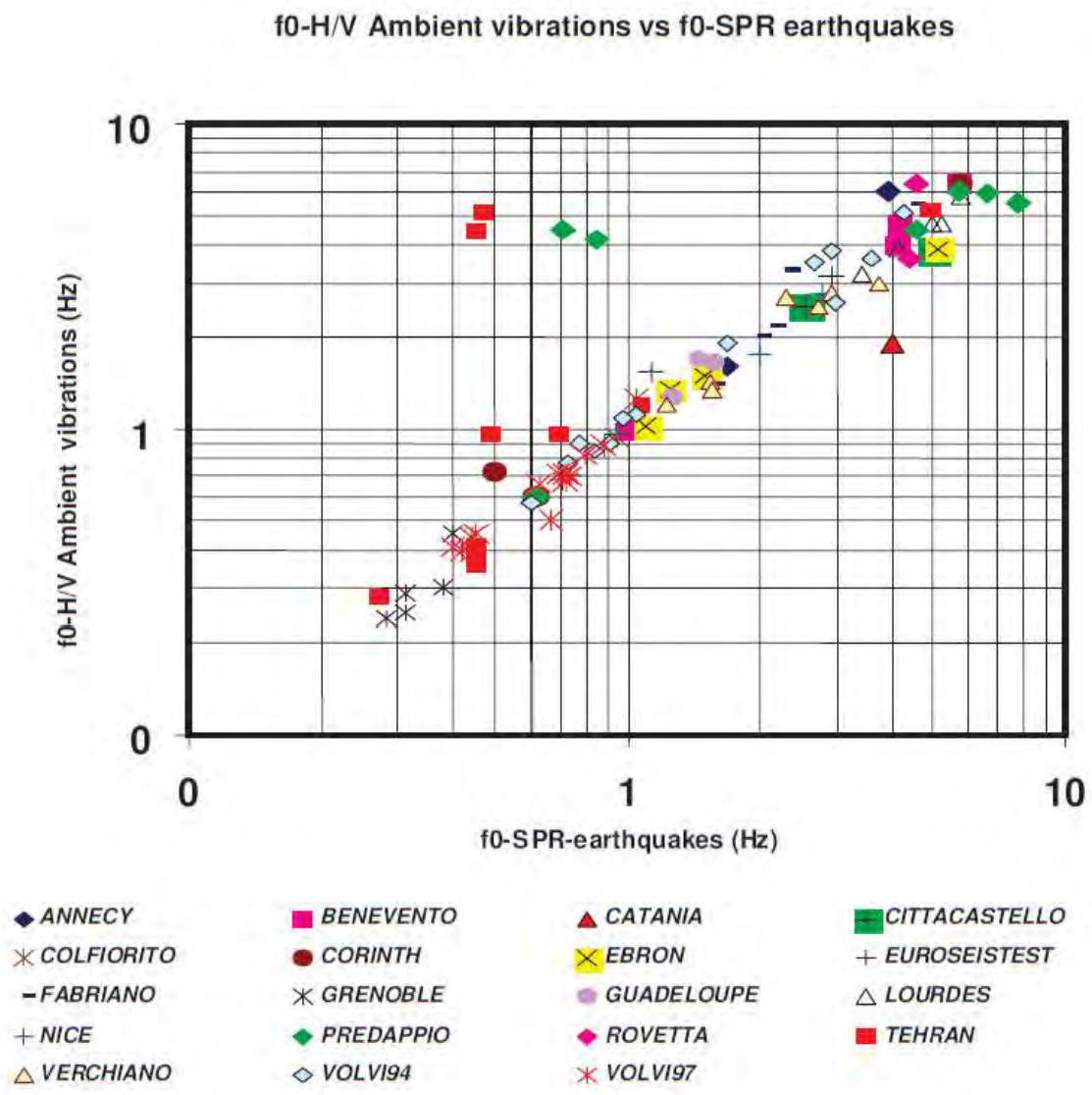

Figure 2.3: *Ambient noise HVSR frequency comparison with earthquake SPR frequency measurements. The vertical axis depicts HVSR frequency values while the horizontal axis shows SPR frequency values for corresponding sites. A strong linear correlation in spectral ratio peak frequency from both methods is shown. Image is from SESAME WP12 (2004).*

fundamental frequency of soil resonance. However, its use in determining higher resonance modes has been controversial. Bonnefoy-Claudet et al. (2009) suggest the HVSR

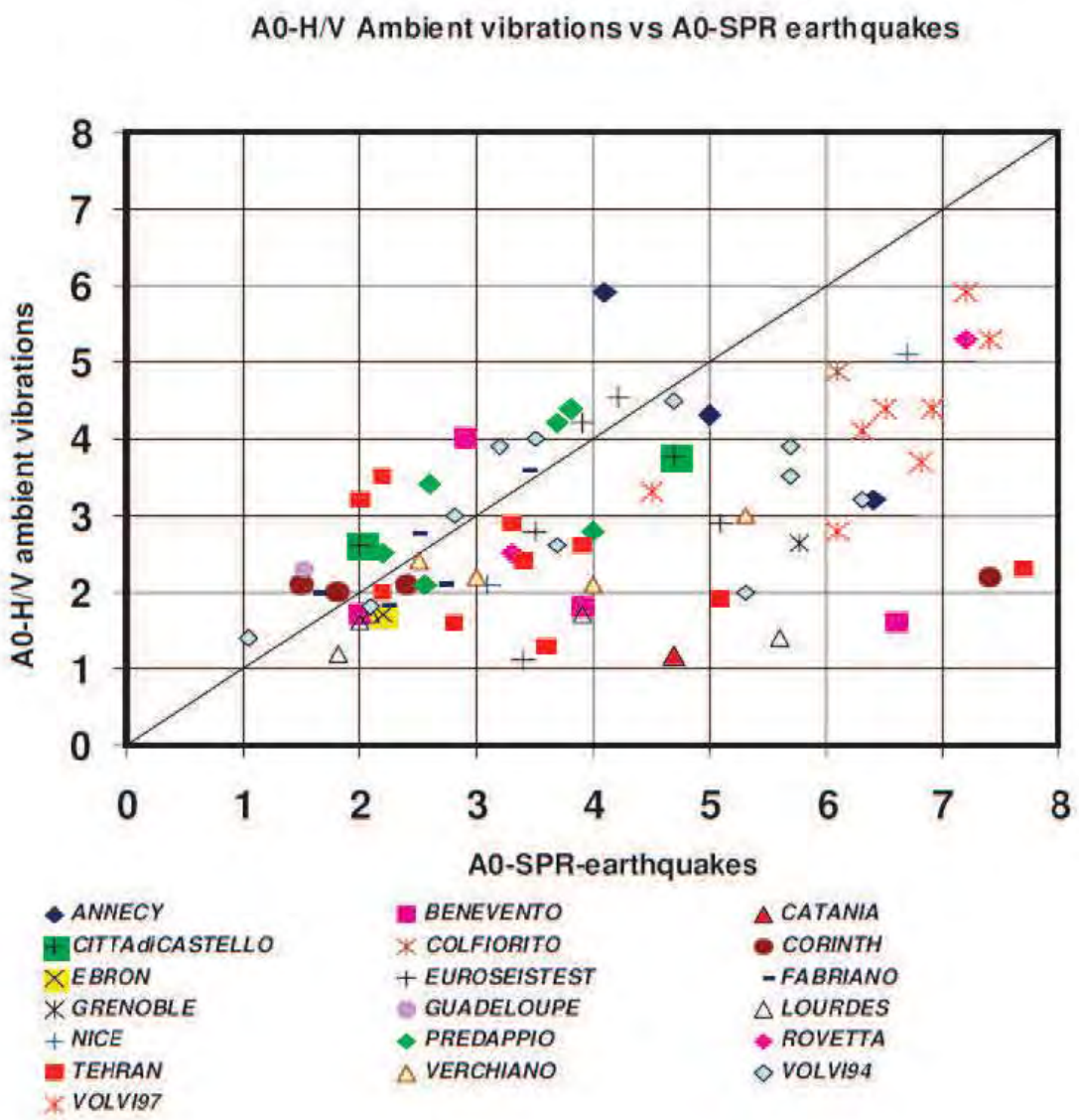

Figure 2.4: *HVSR amplitude comparison with earthquake SPR amplitude measurements. The vertical axis depicts HVSR amplitude values, while the horizontal axis shows SPR amplitude values for corresponding sites. The comparison of amplitudes between the two methods shows overall higher SPR amplitudes than HVSR amplitudes. Image is from SESAME WP12 (2004).*

approach is inadequate for determining higher resonance modes, while other authors such as Lermo & Chavez - Garcia (1994) suggested otherwise.

It is important that, before calculating the HVSR, we filter out earthquake data, any short duration, close (10 - 60 m depending on the size of the source), local sources (footsteps, cars, trains, and other transient sources) and monochromatic signals (construction machines, pumps, industrial machines, etc.) from our data set. Monochromatic signals are evident in the 3 component seismogram in figure 2.5, which shows how the uniform amplitudes of ambient noise data are interrupted by sharp high peaks of induced signal of a single frequency.

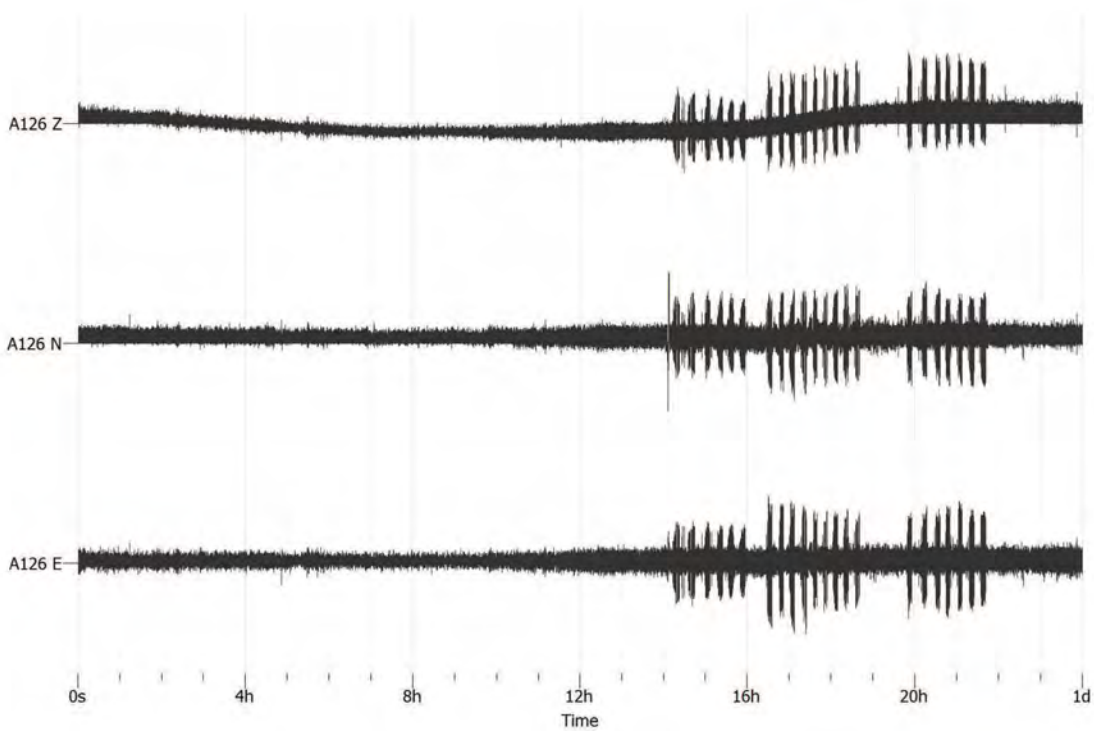

Figure 2.5: *LASSIE station A126 3-component seismogram (Vertical Z, North N, East E) clearly exhibits anthropic noise defined by the interruption of uniform homogeneous signal by sharp distinct peaks between UTC 1400 - 2200 (7 AM - 3 PM PST).*

2.3 Data processing guidelines

We use the Geopsy software (http://www.geopsy.org/) by Wathelet (2005) and Wathelet (2011) to measure the spectra ratio curves at each seismometer location.

Ambient noise data recorded on three component full waveform data, is analyzed in accordance with the Site Effects Assessment Using Ambient Excitations (SESAME) guidelines for implementing the HVSR approach (SESAME WP12, 2004). The SESAME guidelines have three conditions for HVSR curve reliability and five criteria for identification of a peak frequency, f_0, as a clear peak. These criteria are depicted in figure 2.6.

The reliable curve criteria test the amount of variability in the standard deviation of the HVSR amplitude and therefore determine whether the measured curve is a true representation of the HVSR at this site. The criteria for a clear peak determine if the frequency band within which a spectral peak is located is stable and whether the peak may be considered prominent.

Criteria for a reliable H/V curve

i) $f_0 > 10 / l_w$

and

ii) $n_c(f_0) > 200$

and

iii) $\sigma_A(f)<2$ for $0.5f_0<f<2f_0$ if $f0>0.5$Hz

or $\sigma_A(f)<3$ for $0.5f_0<f<2f_0$ if $f0<0.5$Hz

Criteria for a clear H/V peak

(at least 5 out of 6 criteria fulfilled)

i) $\exists f^- \in [f_0/4, f_0] \mid A_{H/V}(f^-) < A_0/2$

ii) $\exists f^+ \in [f_0, 4f_0] \mid A_{H/V}(f^+) < A_0/2$

iii) $A_0 > 2$

iv) $f_{peak}[A_{H/V}(f) \pm \sigma_A(f)] = f_0 \pm 5\%$

v) $\sigma_f < \varepsilon(f_0)$

vi) $\sigma_A(f_0) < \theta(f_0)$

- l_w = window length
- n_w = number of windows selected for the average H/V curve
- $n_c = l_w \cdot n_w \cdot f_0$ = number of significant cycles
- f = current frequency
- f_{sensor} = sensor cut-off frequency
- f_0 = H/V peak frequency
- σ_f = standard deviation of H/V peak frequency ($f_0 \pm \sigma_f$)
- $\varepsilon(f_0)$ = threshold value for the stability condition $\sigma_f < \varepsilon(f_0)$
- A_0 = H/V peak amplitude at frequency f_0
- $A_{H/V}(f)$ = H/V curve amplitude at frequency f
- f^- = frequency between $f_0/4$ and f_0 for which $A_{H/V}(f^-) < A_0/2$
- f^+ = frequency between f_0 and $4f_0$ for which $A_{H/V}(f^+) < A_0/2$
- $\sigma_A(f)$ = "standard deviation" of $A_{H/V}(f)$, $\sigma_A(f)$ is the factor by which the mean $A_{H/V}(f)$ curve should be multiplied or divided
- $\sigma_{logH/V}(f)$ = standard deviation of the $\log A_{H/V}(f)$ curve, $\sigma_{logH/V}(f)$ is an absolute value which should be added to or subtracted from the mean $\log A_{H/V}(f)$ curve
- $\theta(f_0)$ = threshold value for the stability condition $\sigma_A(f) < \theta(f_0)$
- $V_{s,av}$ = average S-wave velocity of the total deposits
- $V_{s,surf}$ = S-wave velocity of the surface layer
- h = depth to bedrock
- h_{min} = lower-bound estimate of h

Threshold Values for σ_f and $\sigma_A(f_0)$

Frequency range [Hz]	< 0.2	0.2 – 0.5	0.5 – 1.0	1.0 – 2.0	> 2.0
$\varepsilon(f_0)$ [Hz]	0.25 f_0	0.20 f_0	0.15 f_0	0.10 f_0	0.05 f_0
$\theta(f_0)$ for $\sigma_A(f_0)$	3.0	2.5	2.0	1.78	1.58
$\log\theta(f_0)$ for $\sigma_{logH/V}(f_0)$	0.48	0.40	0.30	0.25	0.20

Figure 2.6: *Horizontal-to-Vertical Spectral Ratio testing criteria set forth by SESAME. Clockwise from top left panel: Criteria for reliable curve, variable list and description, threshold values for standard deviation of frequency and amplitude, and criteria for clear peak. Image is from SESAME WP12 (2004).*

Conditions for curve reliability: 3 out of 3 must be satisfied

I. f_0 must be greater than 10 divided by the window length. This condition requires that at the frequency (range) of interest, there should be at least 10 cycles in each window.

II. The number of significant cycles must be greater than 200. The second condition determines if the overall recording duration contains sufficient data to be analyzed.

III. This criteria requires an acceptably low level of scattering between all windows. Large standard deviation values often mean that ambient vibrations are strongly non-stationary and undergo some kind of perturbation, which may significantly affect the physical meaning of the HVSR peak frequency. The spectral standard deviation of the amplitude has to be less than a particular value in a particular frequency range that depends on the f_0. If f_0 is greater than 0.5 Hz, the standard deviation of the amplitude must be less than 2 within the range of 0.5 f_0 to $2f_0$. If f_0 is less than 0.5 Hz, the standard deviation of the amplitude must be less than 3 within the range of 0.5 f_0 to $2f_0$.

Criteria for clear HVSR peak: 5 out of 6 must be satisfied

The ”clarity” concept may be related to several characteristics: the amplitude of the spectral ratio peak and its relative value with respect to the spectral ratio values in the surrounding frequency bands, the relative value of the standard deviation of the peak amplitude and frequency, and the standard deviation of estimates from individual windows.

I. Between $\frac{f_0}{4}$ and f_0, there exist a frequency at which the spectral ratio amplitude is less than $\frac{A_0}{2}$.

II. Between f_0 and $4f_0$, there exists a frequency at which the spectral ratio amplitude

at that frequency is less than $\frac{A_0}{2}$.

III. A_0 must be greater than 2.

IV. For frequency stability, the frequency of the peak in the HVSR curves corresponding to mean $+$ and $-$ one standard deviation, is at most 5% higher or lower than f_0.

V. $\sigma_f < \varepsilon(f_0)$ The standard deviation of the peak frequency must be below the threshold value as determined through the threshold value table in figure 2.6.

VI. $\sigma_A(f_0) < \theta(f_0)$ The standard deviation of the amplitude at the peak frequency must be less than the threshold value as determined through the threshold value table in figure 2.6.

2.4 Geopsy software and settings

Ambient noise data collected from the LASSIE array is processed through the application of the HVSR approach by the Geopsy software by Wathelet (2005) and Wathelet (2011). Ho & Polet (2015) demonstrated that variations in Geopsy default parameters yielded negligible variation in results for similar equipment at similar sites in Southern California. Therefore, for our investigation we use the most of the Geopsy default settings for ambient noise HVSR. We adjust the window length l_w to 600 seconds to be able to calculate a HVSR curve up to at least a 30 seconds period (this value represents the corner period of the instrument, beyond which it cannot record the ground motion at its full amplitude). Using these settings, the Geopsy software selects windows that are suitable for analysis, eliminating windows with earthquake like signals or sudden, short impulses and displays these windows color coded based on the time of day, as depicted for an example

recording in figure 2.7, ready for a visual inspection to remove additional windows based on any anomalous signals. We select several days out of the month of data for each station for analysis. Both weekends and weekdays, as well as daytime and nighttime recordings were used for analysis to provide a good statistical representation of the entire month of data for each station. Analysis of ambient noise three component full waveform data for the entire month for each station would require an unnecessary amount of computational hours for minimal to no improvement on the results, as we will show in section 2.4.1. Spectral ratio curves calculated from the selected windows are plotted with colors that match those in the original data window display. These colors help determine if certain peaks or certain signals in the spectral ratio curves are produced only during certain hours of the day, which may suggest a period of signals of anthropic origins in our data. Anomalous windows that suggest an anthropic signal source were removed from our analysis prior to generating the final spectral ratio graph. The HVSR graphs in figure 2.8 show the spectral ratio curves calculated from a Fourier transfer of the time window with its colors corresponding to the colors of the selected time windows.

2.4.1 Data quality check

To investigate the variability in ambient noise data caused by environmental changes and variations in installation, and to assess the magnitude of the variability in the spectral ratio results due to differences in the total duration of the waveforms selected for analysis, we conducted an analysis of waveforms with relatively long duration: a 3-day and a 5-day waveform duration, with 600 second window length for each spectral ratio curve

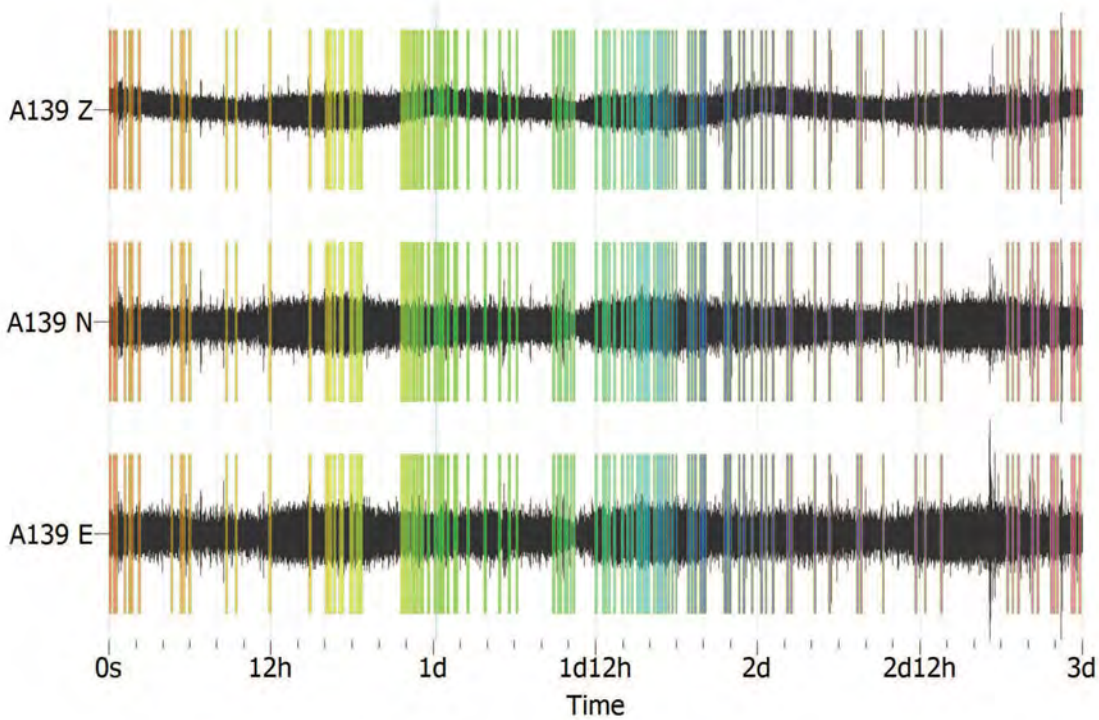

Figure 2.7: *Geopsy window selection of LASSIE site A139 on that station's three component full waveform recording of Z (vertical) component and N and E (horizontal) components. Selected colored windows of data show ambient noise that does not exhibit any sudden, short impulses or undesirable anthropic signals. The color spectrum in the Geopsy software for HVSR analysis shows warmer colors, such as red and orange, at the start time of the ambient noise recording and cooler colors, such as blue and violet, at its end.*

calculation, for the SCSN station at the University of Southern California (USC), as well as LASSIE station N106, as shown in figure 2.9. We chose to use the USC station in our comparison since this station is a permanent vault installation located inside the LA basin with an instrument corner period of 120 seconds, as compared to LASSIE station N106, which has a corner period of 30 seconds. Corner period is the nominal lower period limit beyond which the seismometer's sensitivity to ground motion starts to drop off signifi-

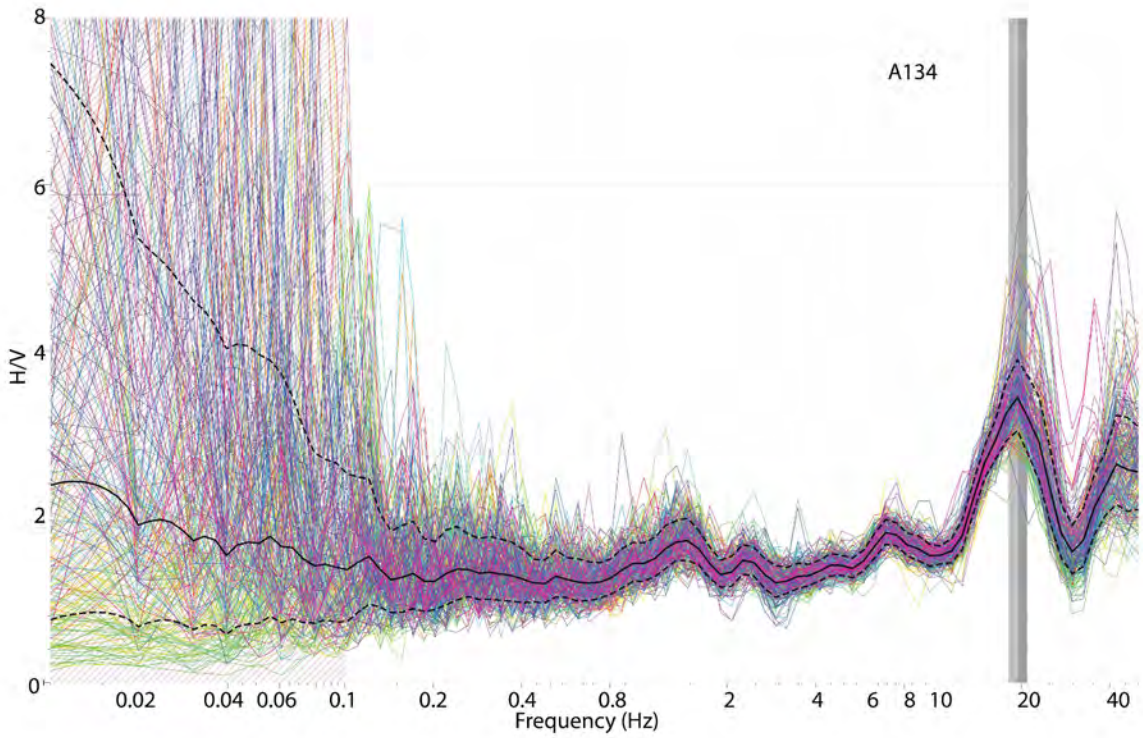

Figure 2.8: *HVSR graph of LASSIE site A134. Each individual line of a particular color represents the spectral ratio curve computed for a specific time window of the same color. The solid line shows the average spectral ratio curve, as determined by the Geopsy software as the geometrical average of all the individual HVSR curves. The dashed lines indicate the standard deviation of the amplitude of the average curve. The peak frequency,* f_0*, is surrounded by grey vertical bars that show its standard deviation.*

cantly and therefore the instrument is no longer able to record ground motions at their true amplitudes. Therefore, with its vault installation and higher corner period, USC represents a ”best case scenario” for our LASSIE analysis. The results for USC show a clear peak at a frequency of 0.15 Hz. The peak value for the USC station shows only a minor improvement in standard deviation of amplitude from 3 day waveform duration to 5 day waveform duration, from a standard deviation of the log value of the amplitude of the peak frequency

of 1.15 to 1.18, for example. Measurements of peak frequency from these spectral graphs also showed only minor changes in the thousandths decimal position. Based on the results of our comparison, we consider the cost of the additional computational time that would be required for this minor improvement to outweigh the benefit of improving the results. We therefore used 3 day time windows in our analysis of the LASSIE data-set.

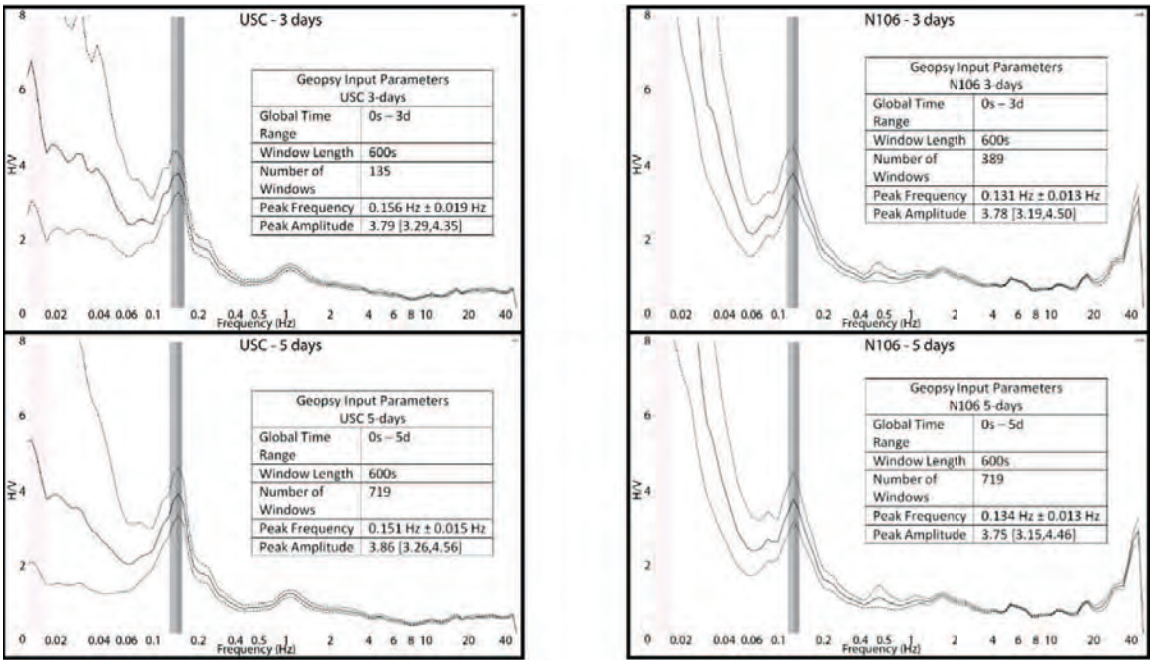

Figure 2.9: *A comparison of LASSIE station, N106, and SCSN station, USC. The two stations were selected to perform a check whether a significant improvement in the results is obtained when the data is analyzed for a longer range of time. Results from this test showed only a minor improvement in both peak values and their standard deviation.*

2.5 HVSR applied to LASSIE site A137

We show the details of the analysis for one example, for LASSIE station A137. We choose to use station A137 since the station has been mostly undisturbed with minimal

external influences to the full waveform data. This station is located outside the Los Angeles basin on Tertiary marine sandstone. The installation site is off the Ahwingna trail in Hacienda Hills, managed by the Puente Hills Landfill Native Habitat Preservation Authority, located on the eastern edge of the Puente Hills. This site is not in close proximity to any residential housing or industrial structure. We therefore expect this location to be an example of an ideal installation site to collect ambient noise data for the LASSIE network.

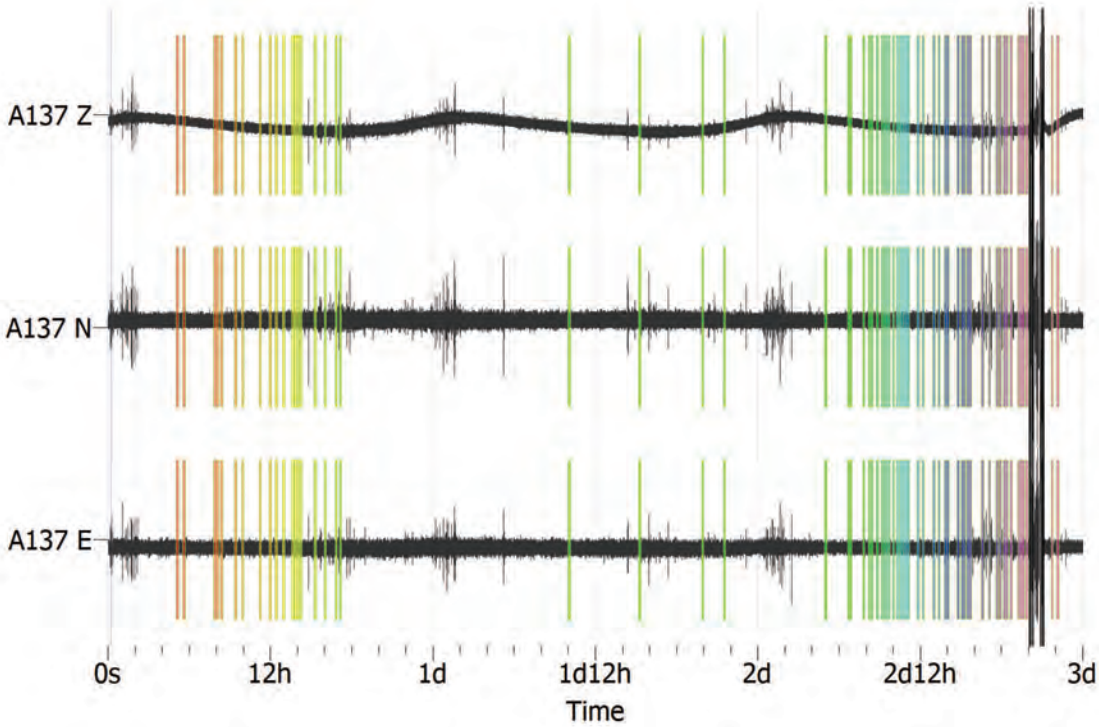

Figure 2.10: *Geopsy window selection for waveform data recorded at LASSIE site A137. Colored boxes show windows selected for a standard window length of 600 seconds.*

We use the Geopsy default parameters as documented in Appendix B. The use of these input parameters produces 65 selected windows of ambient noise as seen in figure 2.10. Each window of data undergoes a Fourier transform and spectra for all windows are then

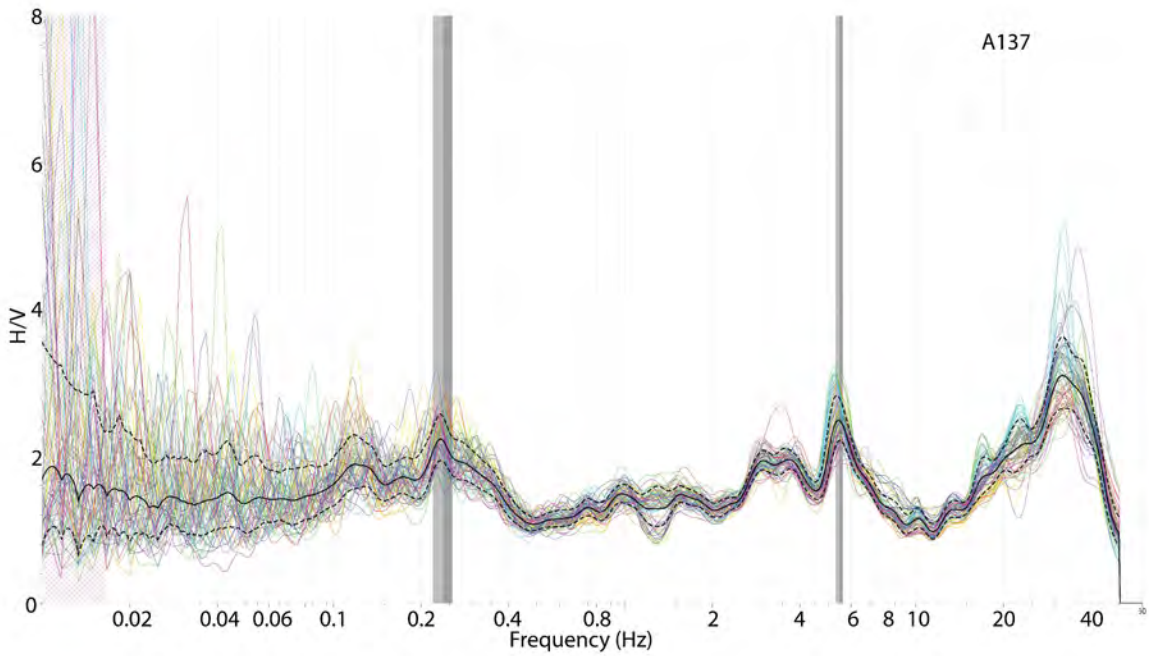

Figure 2.11: *HVSR graph of LASSIE site A137. The pink hatched box on the left hand side of the spectral graph represents the frequency range where the time widow is too short to compute a reliable spectral ratio. Two prominent peaks are shown at 0.238 Hz and 5.450 Hz. Two peaks can occur for two large impedance contrasts in the subsurface. An artifact at high frequency is exhibited near the Nyquist frequency of the seismometer, which due to its high frequency likely represents an industrial or anthropic source, and which is not considered in our analysis.*

averaged to generate the HVSR curve as displayed by figure 2.11. Two peak frequencies of interest are selected for investigation as listed in Table 2.1. The clarity of the two peak frequencies and the reliability of the spectral curve are then tested in accordance to the guidelines set forth by the SESAME project by Bard & SESAME Participants (2004).

f_0	$\pm f_0$	A_0	σ_A
0.238	0.018	2.216	1.149
5.450	0.204	2.423	1.136

Table 2.1: *Information extracted from the A137 spectral graph. Symbols are defined as follows: HVSR peak frequency (f_0), standard deviation of the peak frequency ($\pm f_0$), HVSR amplitude at the peak frequency (A_0), and the standard deviation of A_0 (σ_A).*

SESAME criteria for reliable curve

The three criteria for a reliable curve must be satisfied for it to be considered reliable for interpretation.

I. $f_0 > \frac{10}{l_w}$; Criteria I for a reliable curve states there have to be at least 10 wave periods in each window. We have $f_0 = 5.450Hz$, which is greater than the value of $\frac{10}{600seconds}$; therefore, criteria I for a reliable curve is true. For this example, we test the highest peak observed.

II. $n_c(f_0) > 200$ where the number of significant cycles $n_c(f_0) = l_w \times n_w \times f_0$ is $600 \times 65 \times 5.450 \approx 210,000$. Therefore, criteria II for a reliable curve is true.

III. $\sigma_a(f) < 2 \quad \text{for} \quad 0.5f_0 < f < 2f_0 \quad \text{if} \quad f_0 > 0.5Hz$ translates into $\sigma_a(f) =< 2$ within the frequency range $2.725Hz - 10.9Hz$. At $f = 8.8Hz$, $\sigma_a(f) = 1.136$. Therefore, criteria III for reliable curve is true.

In conclusion, all three criteria for a reliable curve are true. Therefore we proceed to test for the criteria for clear peak.

SESAME criteria for clear peak

I. $\exists f^- \in [\frac{f_0}{4}, f_0] \quad | \quad A_{H/V}(f^-) < \frac{A_0}{2}$ states there exist a frequency f^- between $\frac{f_0}{4}$ and f_0 at which the amplitude of the HVSR curve at the HVSR curve is less than $\frac{A_0}{2}$ where $\frac{A_0}{2}$ is 1.211. There does not exist a frequency f^- between $\frac{f_0}{4}, 1.3625Hz$, and $f_0, 5.450Hz$, at which the amplitude is less than $\frac{A_0}{2}$; therefore criteria I for a clear peak is false.

II. $\exists f^+ \in [f_0, 4f_0] \quad | \quad A_{H/V}(f^+) < \frac{A_0}{2}$ states there exist a frequency f^+ between f_0 and$4f_0$ for which the amplitude of f^- is less than $\frac{A_0}{2}$ where $\frac{A_0}{2}$ is 1.211. There exist a frequency between $8.7Hz$ and $14.8Hz$ for which the amplitude of f^+ is less than $\frac{A_0}{2}$; therefore, criteria II for a clear peak is true.

III. $A_0 > 2$ where A_0 is 2.423; therefore, criteria III for a clear peak is true.

IV. $f_{peak}[A_{H/V}(f) \pm \sigma_A(f)] = f_0 \pm 5\%$ requires that the frequency of the peak for the two curves that represent the HVSR $+$ and $-$ its standard deviation is within 5% of f_0, where $f_0 \pm 5\%$ is the range of $5.17Hz$ to $5.72Hz$. We measure f_{peak} to be $5.37Hz$; therefore, criteria IV for a clear peak is true.

V. $\sigma_f < \varepsilon(f_0)$ states that the σ_f of 0.204 should be less than the threshold value for the stability condition which as shown in figure 2.6 is $\varepsilon(f_0)$, $0.05f_0$ which is $0.05 \times 5.450 = 0.2725Hz$; therefore, criteria V for a clear peak is true.

VI. $\sigma_A(f_0) < \theta(f_0)$ states that the $\sigma_A(f_0)$ of 1.136 should be less than the threshold value for the stability condition which as shown in figure 2.6 is $\theta(f_0) = 1.58$; therefore, criteria V for a clear peak is true.

At least 5 of the 6 criteria must be fulfilled for the peak to be identified as a clear peak. 5 of the 6 criteria for clear peak are fulfilled for the peak near 5 Hz frequency of site A137;

therefore, the peak is clear. This routine process is performed for each reliable curve and peak in each LASSIE station for reliability and clarity.

Chapter 3

Results

We present the values measured from 127 spectral peaks from the LASSIE HVSR graphs as tables, and as regional maps of peak frequencies with corresponding spectral amplitudes. Data from 70 stations produced reliable curves; from those reliable curves, we measured 127 peaks. 94 of the 127 measured peaks may be classified as clear peaks according to the SESAME criteria. A complete set of the HVSR results is available in Appendix B. Our analysis produced a wide variety of HVSR graphs: some spectral ratio curves show multiple peaks occurring at a range of frequencies, some graphs show no peaks or simple clear single peaks. We are unable for 8 stations to process our data with a long window length regardless of waveform duration, due to low ambient noise levels; for 3 other stations we could not retrieve data due to hardware issues or equipment malfunction. However, we still have good spatial coverage of the entire LASSIE line through the LA basin.

We document all 94 clear peaks and as well as the 33 peaks that failed 2 or more clear peak criteria. The original criteria for a clear peak were developed for single station anal-

ysis. However, since our data-set consists of very closely spaced stations, we consider that there is still valuable information contained in peaks that may fail two or more criteria, yet are consistently observed over a significant lateral extent along the network. The distribution of the number of spectral peaks that pass the criteria for reliable curve and clear peak in accordance to the SESAME guidelines is graphed in figure 3.1 together with additional peaks that failed two or more criteria but were consistently observed.

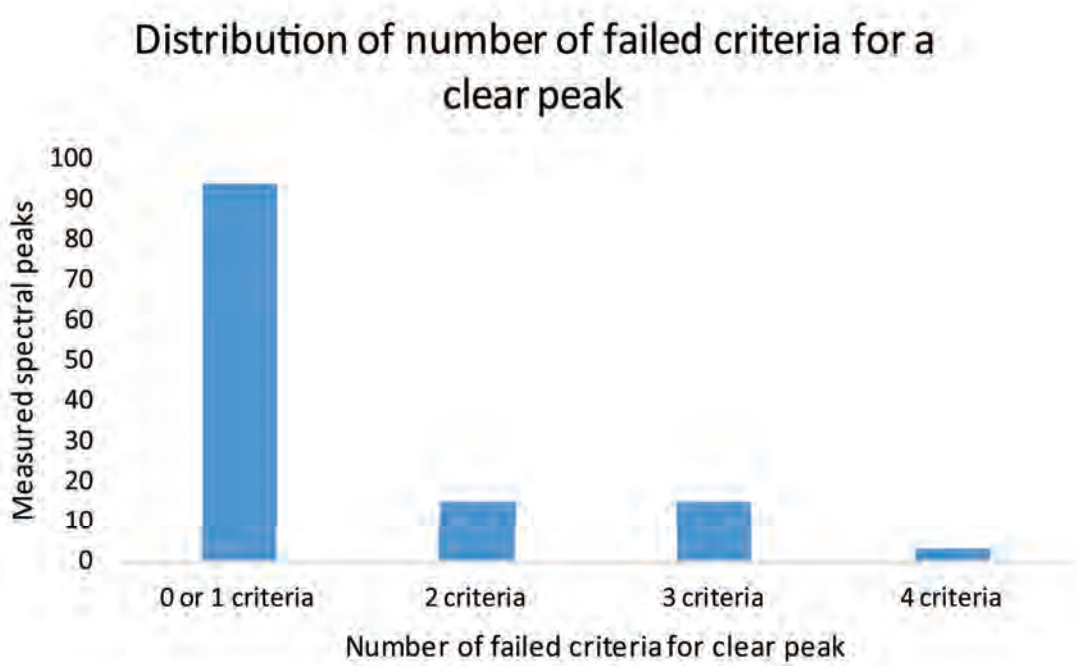

Figure 3.1: *Distribution of number of spectral peaks that failed a specific number of clear peak criteria for LASSIE stations and selected SCSN stations. We measure 94 clear peaks that failed 1 or no criterion, 15 peaks that failed 2 criteria, 15 peaks that failed 3 criteria, and 3 peaks that failed 4 criteria.*

We show our reliable curve and clear peak results in figure 3.2, which groups the results in the frequencies ranges of $0.003Hz \leq f_0 \leq 0.084Hz$, $0.085Hz \leq f_0 \leq 0.159Hz$,

$0.160Hz \leq f_0 \leq 1.0Hz$, and $1.0Hz \leq f_0$ Specific values may be found in Tables B.2, B.3, B.4, B.5, and B.6 in Appendix B. We observe a consistent peak in a frequency range of $0.085Hz \leq f_0 \leq 0.159Hz$ within the LA basin as shown in figure 3.3. We chose these ranges of frequency in order to group peak frequencies that appear to be consistent laterally, just slowly changing in frequency along the line as illustrated by an example in figure 3.4.

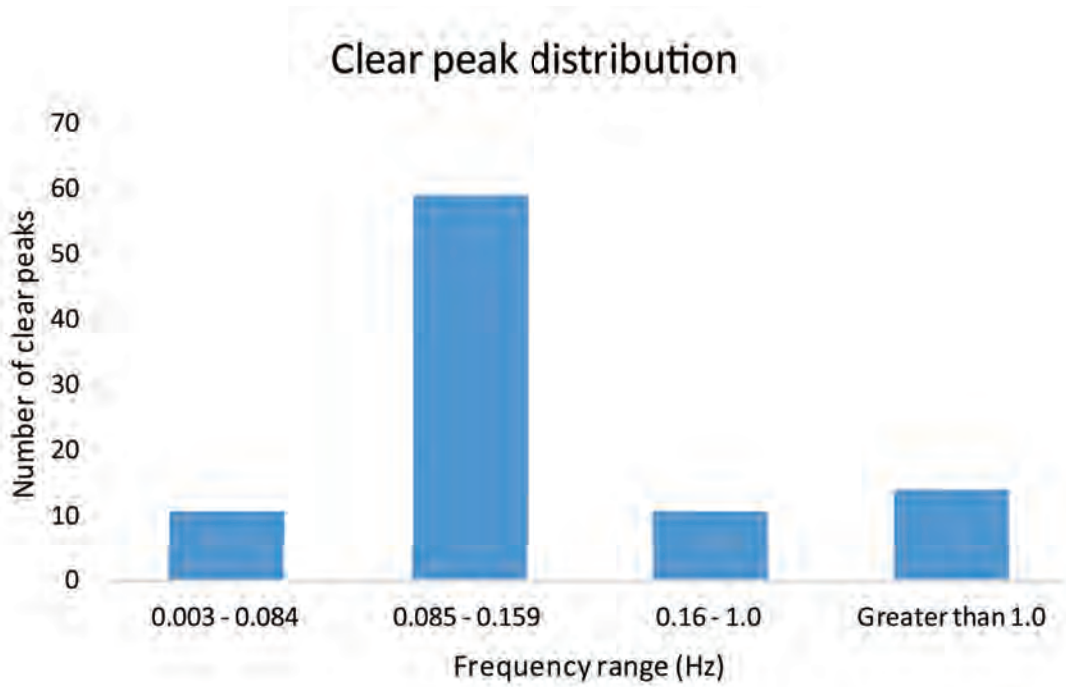

Figure 3.2: *Distribution of number of clear peaks in specific frequency bands for LASSIE stations and selected SCSN stations.*

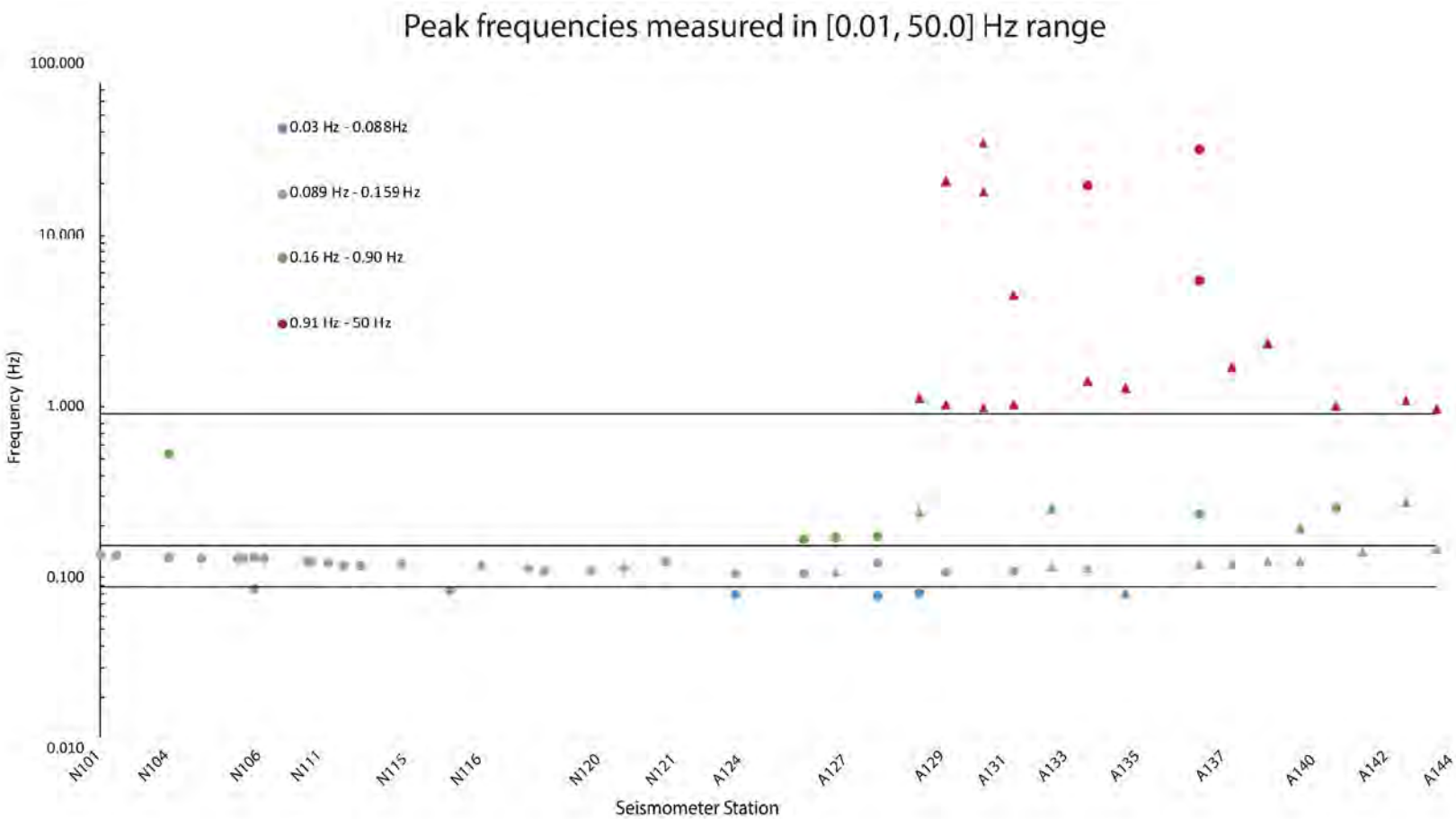

Figure 3.3: *Distribution of Los Angeles basin transect peaks frequencies. Colors shows different frequency groups, circles shows clear peaks, and triangles are peaks that are not classified as clear.*

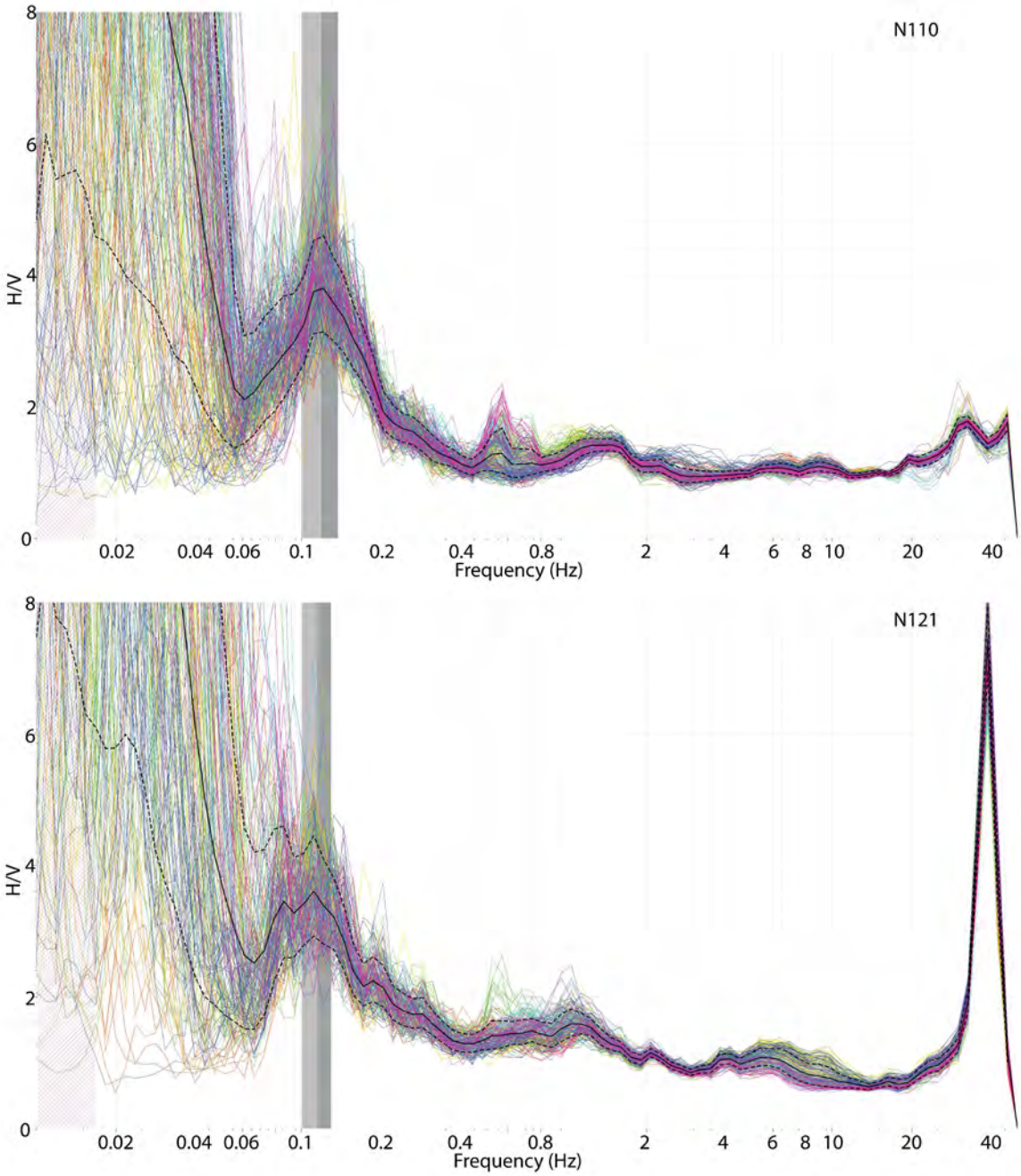

Figure 3.4: *LASSIE stations N110 and N121 show a similar spectral peak at 0.12 Hz and 0.11 Hz respectively. These stations are separated by 8 km. Peaks at similar frequencies can be tracked on numerous stations. Description for the graph is as for figure 2.8.*

3.1 Spectral peak frequencies and amplitudes for the LA basin transect

We examine the measured peak frequencies and their amplitudes for the LA basin transect component of the LASSIE array. We are interested in observing how the measured spectral peak frequencies and peak amplitudes change with distance and basin depth along the transect.

Amplitudes and frequencies for peak frequencies between 0.003 Hz - 0.084 Hz

In figure 3.5 we show the four measured spectral peak frequencies and peak amplitudes between 0.003 Hz and 0.084 Hz from the LA basin transect portion of LASSIE. These measurements are from station site A124, A128, A129, and A135 located near the center and northeastern edge of the basin.

Amplitudes and frequencies for peak frequencies between 0.085 Hz - 0.159 Hz

In figure 3.6 we show our measurements of 37 spectral peak frequencies and the corresponding peak amplitude for peaks between 0.085 Hz and 0.159 Hz from the LA basin transect portion of LASSIE. Measurements in this frequency range are from 36 of the 44 stations on the LA basin transect. Since these peaks are consistently present along the entire length of the profile, it is likely that they are the result of a consistent and systematic impedance contrast along the entire line. Station site N108 has two measured spectral peaks in this frequency range. The peak frequencies in this frequency range show a gradual change in both spectral peak frequencies and peak amplitudes except for the two frequency

measurements from station N108 and N116 at 0.085 Hz and 0.087 Hz. Station N116 is located above the deepest portion of the basin and station N108 is located above the center of the southwestern sloping basement of the basin.

Amplitudes and frequencies for peak frequencies between 0.16 Hz - 1.0 Hz

In figure 3.7 we show our measurements based on 12 spectral peaks from 11 stations within the frequency range of 0.16 Hz to 1.0 Hz from the LA basin transect portion of LASSIE. Apart from one measurement from station N103, located on the southwestern edge of the basin, the other 11 spectral peaks are from 10 stations located over the northeastern half of the LASSIE LA basin transect. Measured frequencies in this range could be subdivided in two groups, a lower frequency group of 9 peaks in the range 0.16 Hz - 0.28 Hz is located on the northeastern half of the basin and a higher group of 3 peaks in the range of 0.5 Hz to 1 Hz located on the southwestern edge and outside of the LA basin.

Amplitudes and frequencies above 1.0 Hz

Our highest frequency peaks are those above 1 Hz. We measured 20 peaks in total, from 12 stations, at this frequency range. At these high frequencies, any impedance contrasts that would cause these peaks are expected to be very shallow, or an alternative explanation could be the presence of industrial noise. These measurements from the LA basin transect of LASSIE are located exclusively over the northeastern half of the LA basin. Since the locations of these peaks are so geographically consistent over a fairly long distance, it appears unlikely that they could be due to a highly localized industrial noise source. Like the previous frequency range group, this frequency range could also be subdivided based

on measured spectral peak values, the first group is between 1.0 Hz to 5.0 Hz and the second group is above 18.0 Hz.

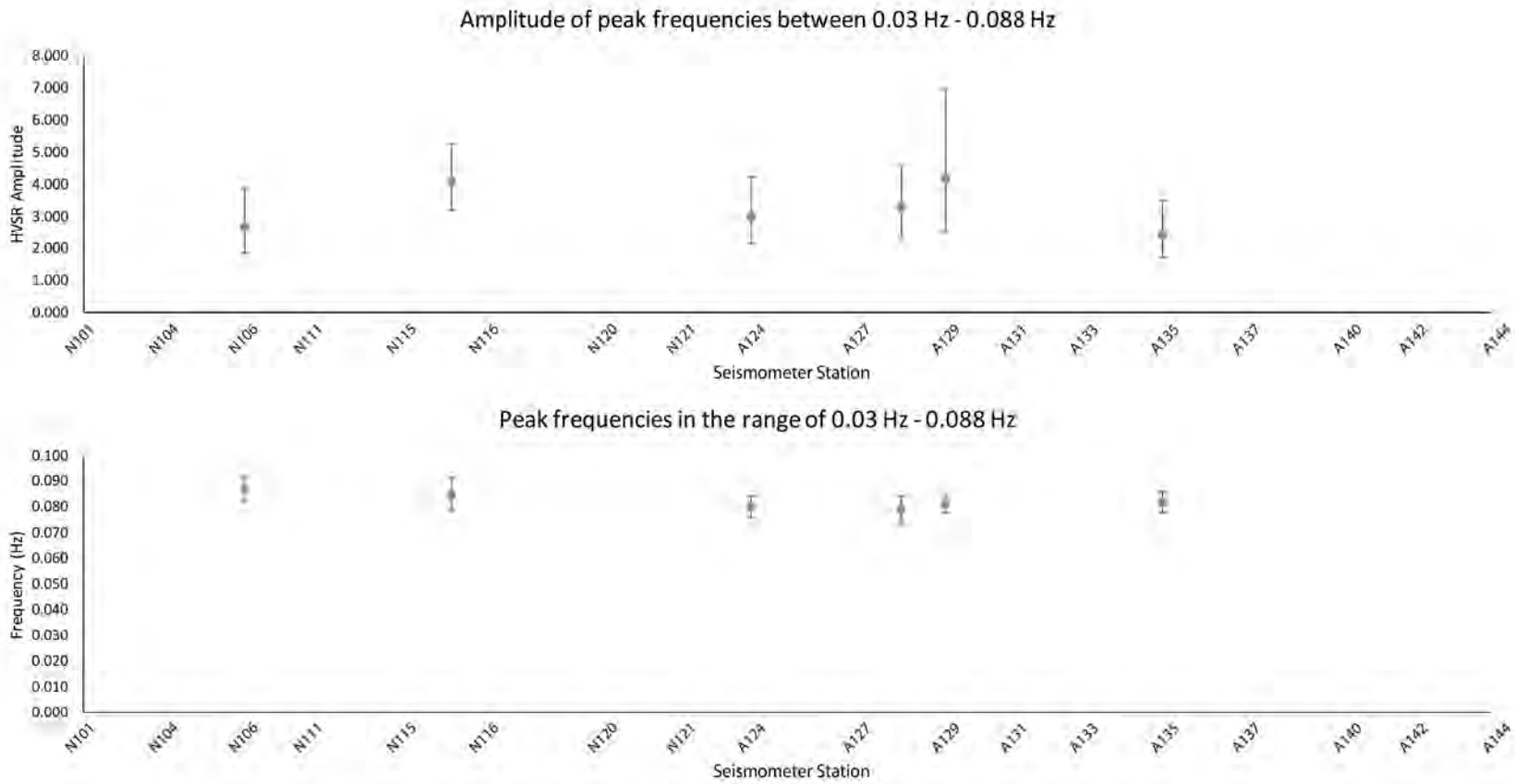

Figure 3.5: *Graphs of the measured spectral peak amplitudes and frequencies in the frequency range of 0.003 Hz - 0.084 Hz. The top graph shows measured HVSR amplitudes for peak frequencies along the y axis and the station positions in the LA basin transect along the x axis. Vertical bars for each point represent the amplitude standard deviation. The bottom graph shows measured HVSR peak frequency values in units of Hz along the y axis and the station along the x axis. Vertical bars on each data point display the standard deviation for each peak frequency.*

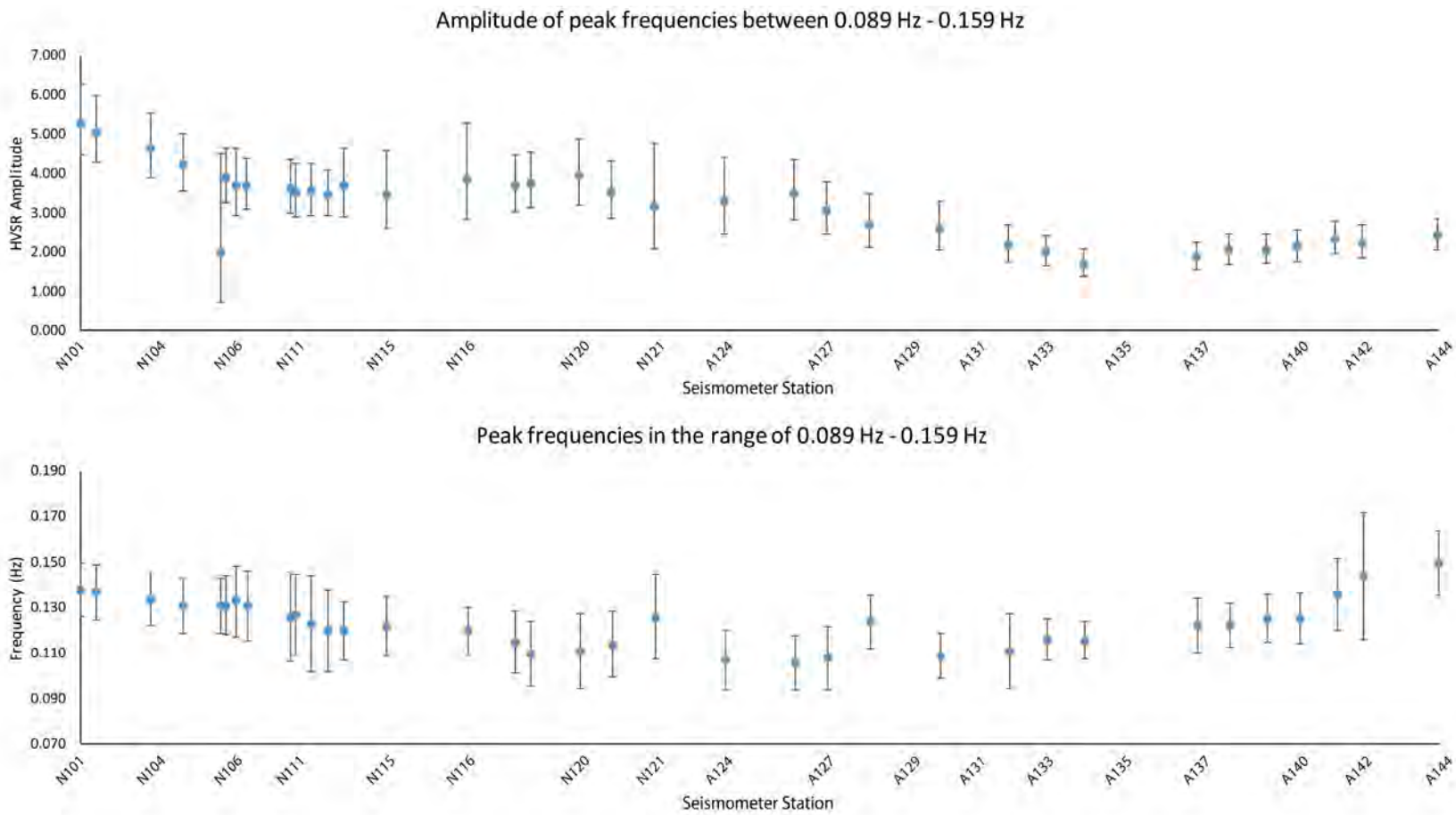

Figure 3.6: *Graphs of the measured spectral peak amplitudes and frequencies in the frequency range of 0.085 Hz - 0.159 Hz. Symbols, axes, annotations and error bars are as in figure 3.5.*

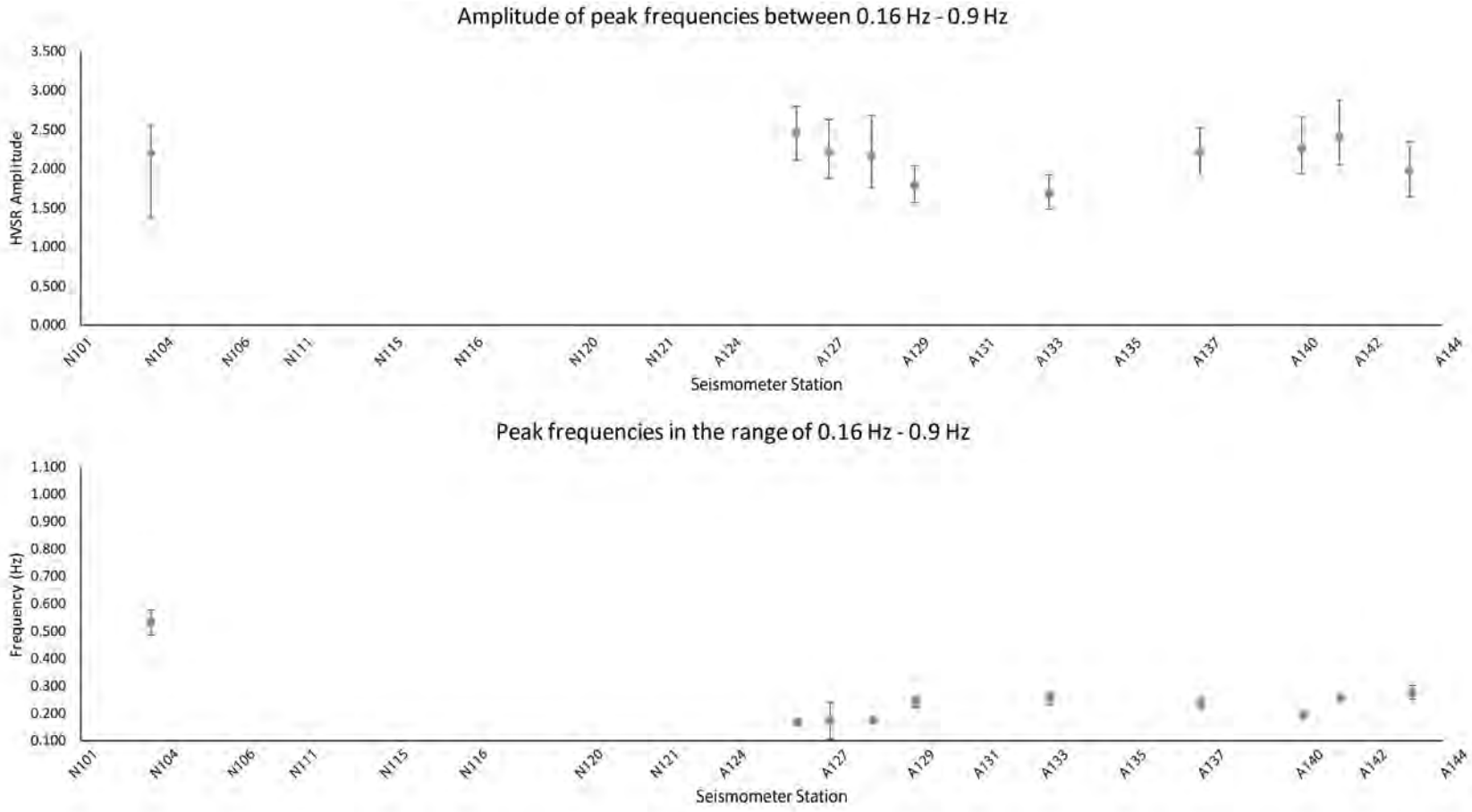

Figure 3.7: *Graphs of the measured spectral peak amplitudes and frequencies in the frequency range of 0.16 Hz - 1.0 Hz. Symbols, axes, annotations and error bars are as in figure 3.5.*

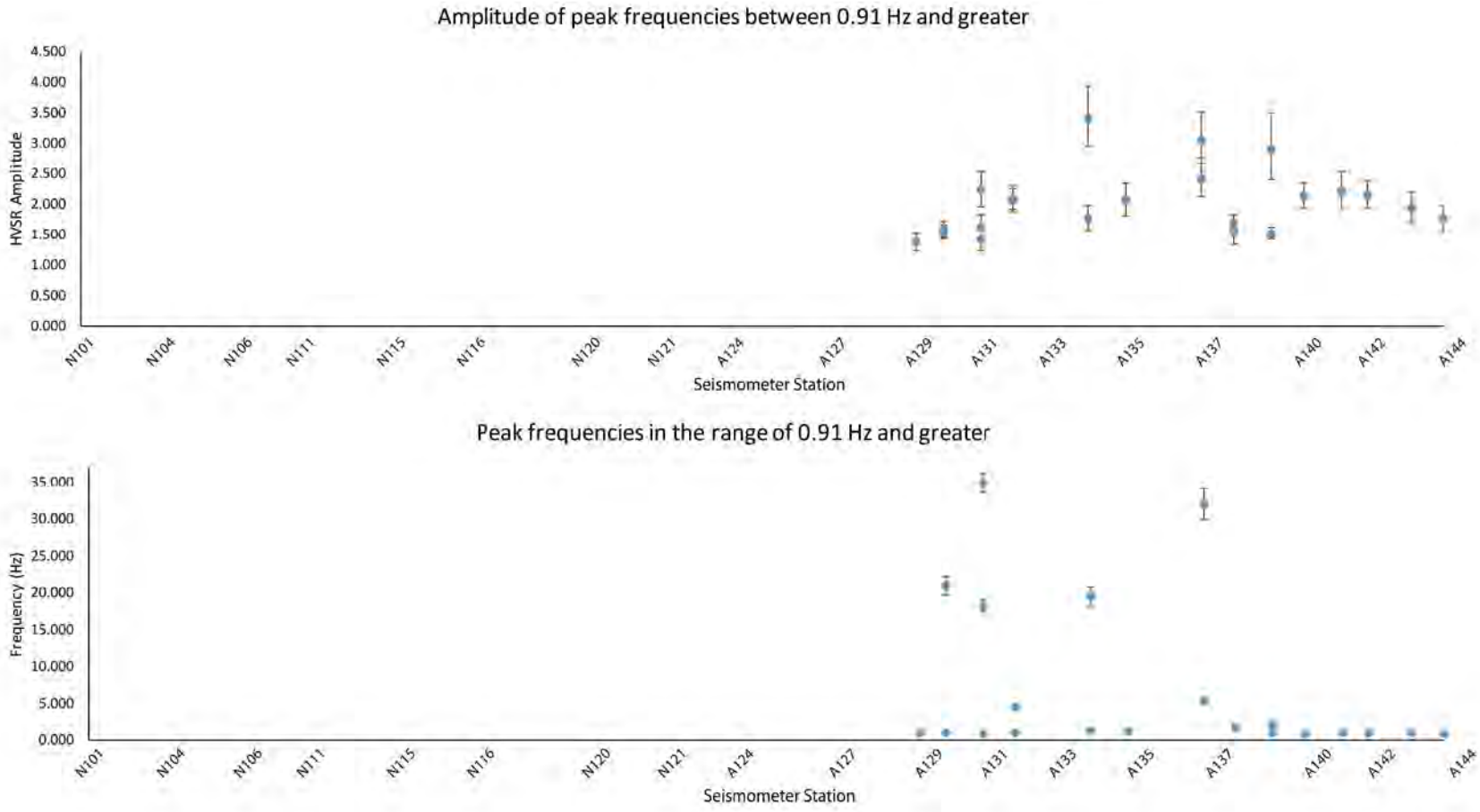

Figure 3.8: *Graphs of the measured spectral peak amplitudes and frequencies above 1.0 Hz. Symbols, axes, annotations and error bars are as in figure 3.5.*

3.2 Maps of spectral peak frequencies and amplitudes for the LA basin

We use the Generic Mapping Tools (GMT) software developed by Wessel et al. (2013) to generate topographic maps of the spectral peak frequencies and peak amplitudes. The LA basin transect of LASSIE is shown in figure 2.1 by the diagonal line of LASSIE stations from the southwest edge of the basin towards the northeast basin edge. The maps were created to more easily visualize and observe variations in spectral peak frequencies and peak amplitudes with changes in position within and outside of the LA basin. The Long Beach cluster covering 50 km^2 is accentuated by a secondary map, which shows smaller scale variations in spectral peak frequencies and peak amplitudes.

Frequency group 0.003 Hz - 0.084 Hz

Figure 3.9 shows a regional map of the LASSIE network and displays the measurements of peak frequencies in the range between 0.003 Hz to 0.084 Hz. Stations with measured spectral peaks within this frequency range are located at both the southwestern and northeastern edge of the LA basin. Measured spectral peak amplitudes are larger near the coast than inland. The more detailed LASSIE regional map for the Long Beach area as shown in figure 3.10 shows a similar pattern of higher spectral peak amplitudes closer to the coastline than inland.

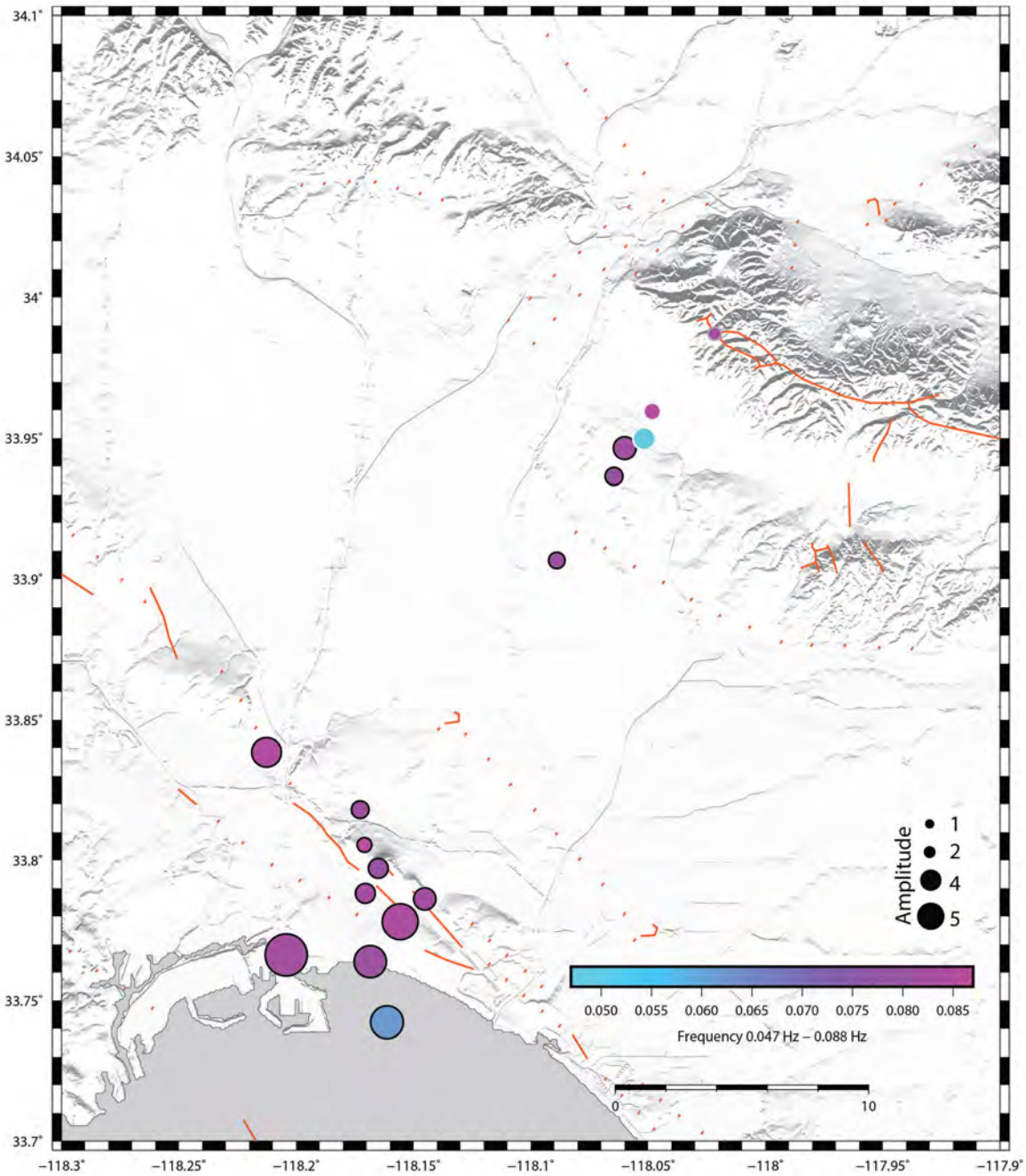

Figure 3.9: *Peak frequencies and amplitudes in the range of 0.003 Hz to 0.084 Hz are shown with color, with the amplitudes of the peaks indicated by the size of the circle. Black outlines indicate clear peaks and gray outlines unclear peaks. Orange lines show faults based on USGS Quaternary Fault and Fold Database. Scale bar in units of kms*

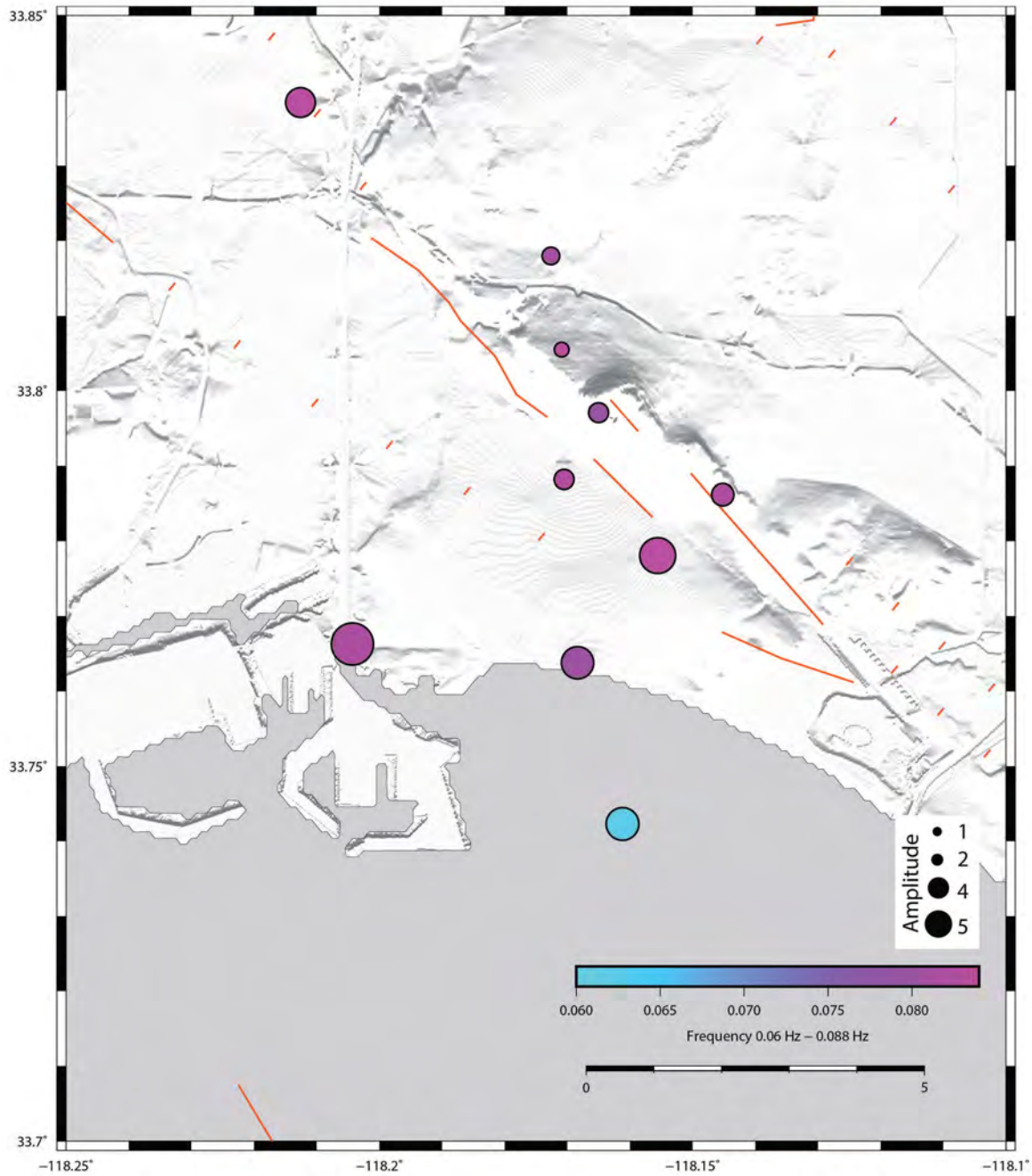

Figure 3.10: *More detailed map of the Long Beach area for peak frequencies and amplitudes in the range of 0.003 Hz - 0.084 Hz. Symbols, lines, scales and colors as in figure 3.9.*

Frequency group 0.085 Hz - 0.159 Hz

Figures 3.11 and 3.12 show similar maps as those in the previous section, but for the measured peak frequencies in the range of 0.085 Hz to 0.159 Hz. We observe an anomalous peak frequency and amplitude measurement offshore of Long Beach. This anomalous recording is likely due to the installation site being a man-made offshore oil platform known as Thumbs Island. Stations with measured spectral peaks within this frequency range are located throughout the LA basin. Measured spectral peak amplitudes are larger near the coast than inland. Spectral peak frequencies are generally lower in value at the basin center than the basin edges and thus correlate with basin depth. The more detailed LASSIE regional map for the Long Beach area shows a similar pattern of higher spectral peak amplitudes closer to the coastline than inland.

Frequency group 0.16 Hz - 1.0 Hz

An additional set of maps for peak frequencies in the range of 0.16 Hz to 1.0 Hz are shown in figures 3.13 and 3.14. Stations with spectral peaks within this frequency range are located at both the southwestern edge near the shore and the northeastern edge of the LA basin. Measured spectral peak amplitudes are similar in value. The more detailed LASSIE regional map for the Long Beach area shows a lower density of measured peak frequencies near the southwestern edge of the basin.

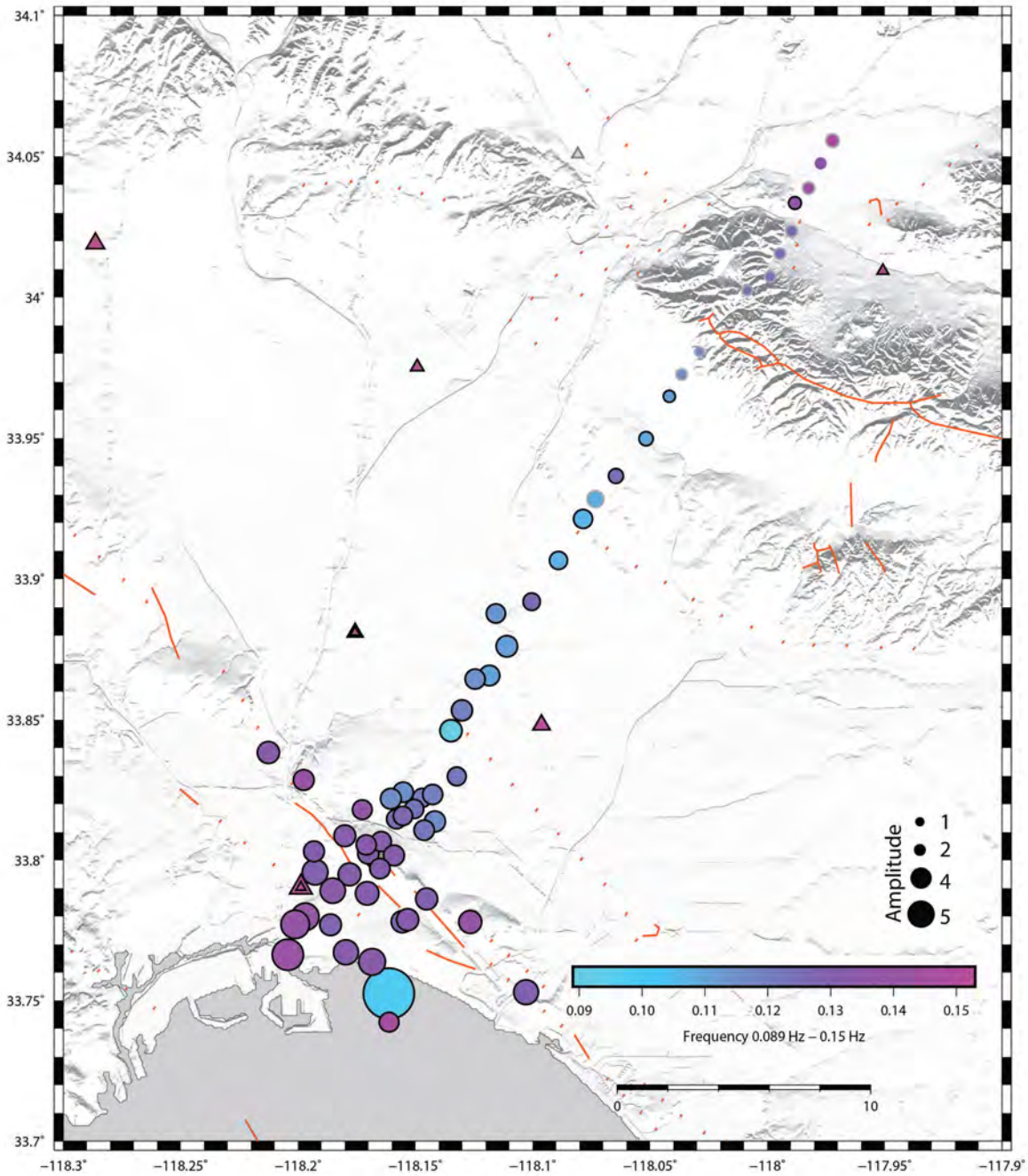

Figure 3.11: *Peak frequencies and amplitudes in the range of 0.085 Hz - 0.159 Hz. Symbols, lines, scales and colors as in figure 3.9*

Frequency group 1.0 Hz and greater

A final set of maps for the highest peak frequencies, those above 1 Hz, are shown in figures 3.15 and 3.16. Stations with these high frequency spectral peaks are located at both

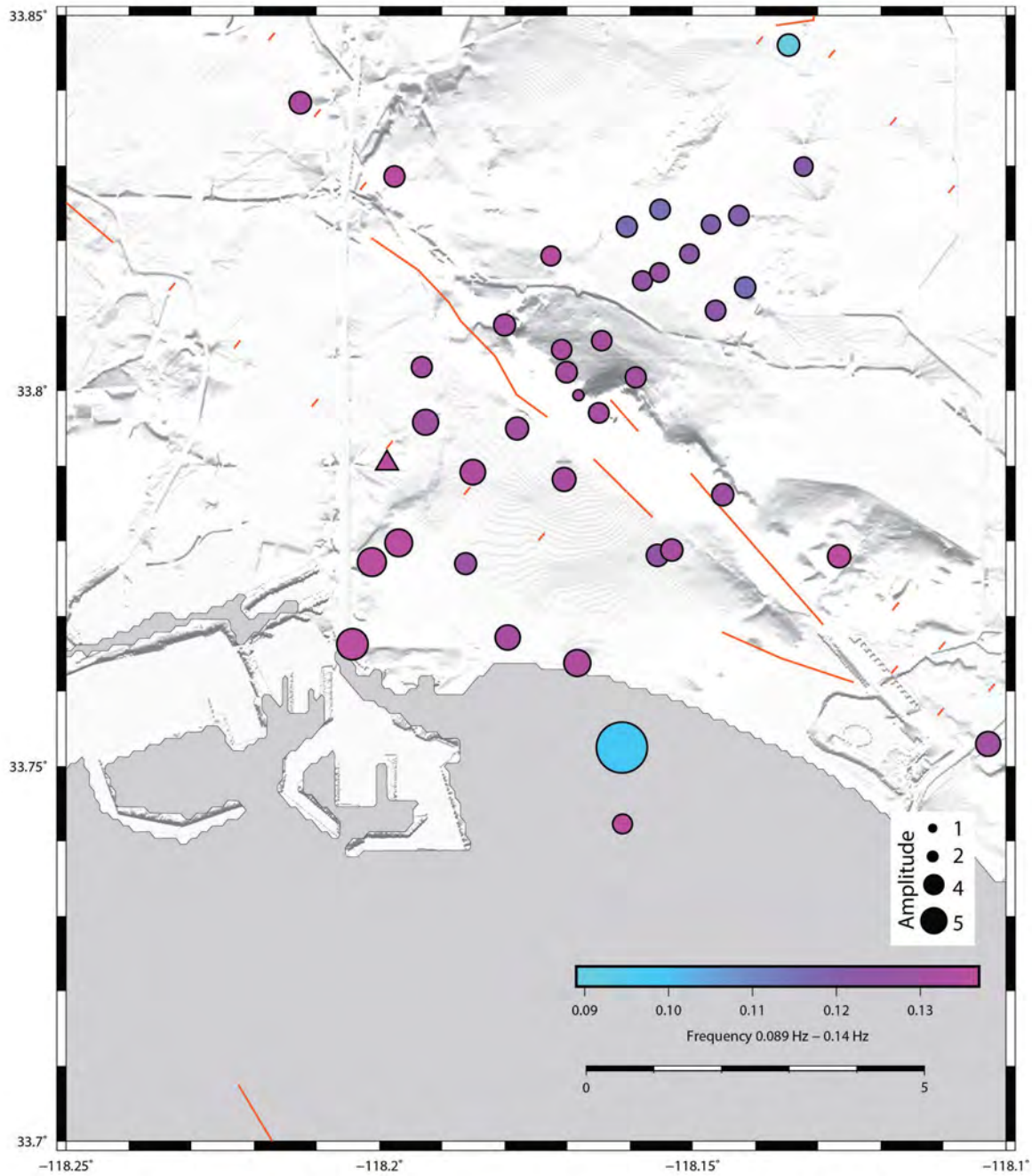

Figure 3.12: *More detailed map of the Long Beach area for peak frequencies and amplitudes in the range of 0.085 Hz - 0.159 Hz. Symbols, lines, scales and colors as in figure 3.9*

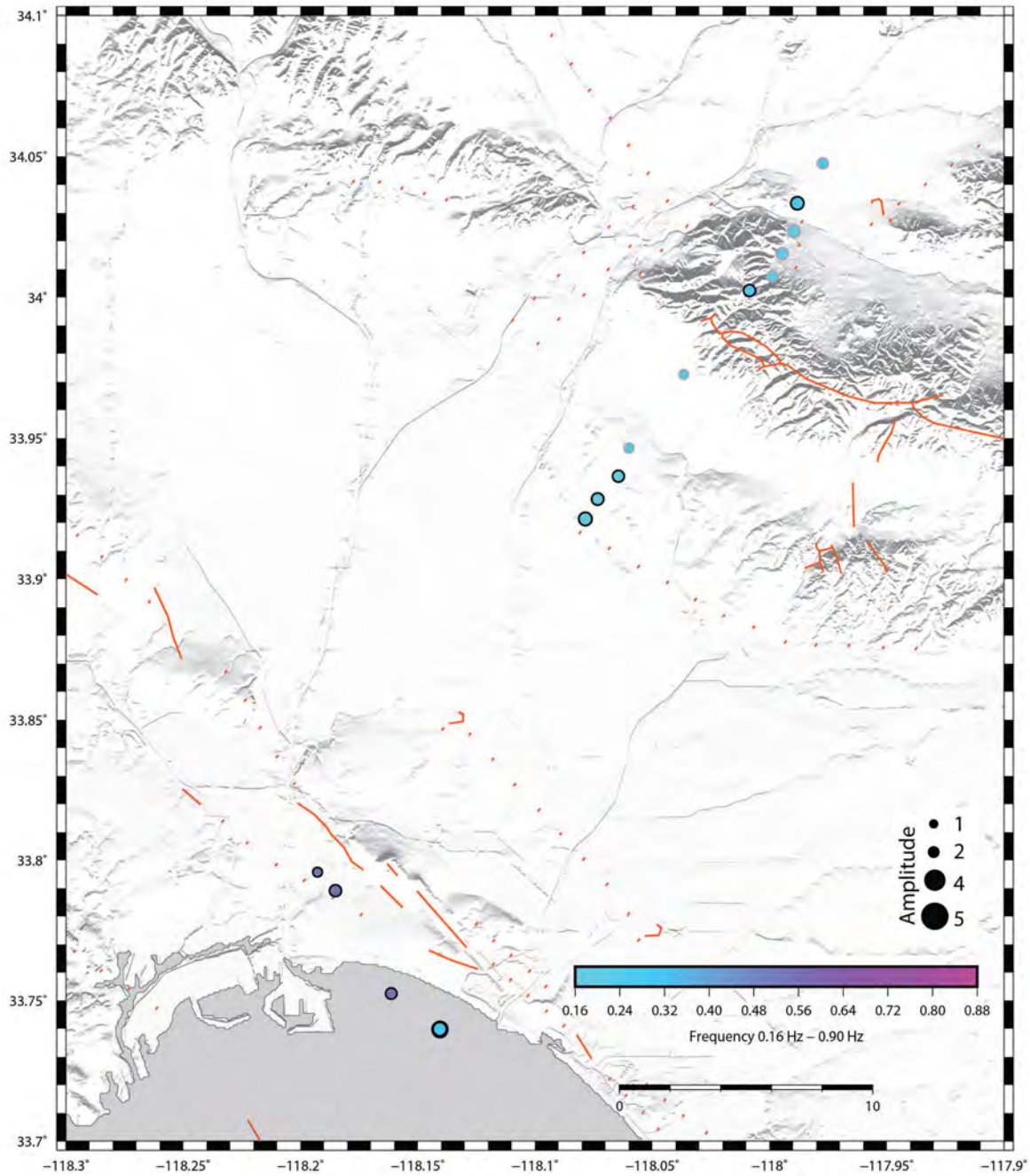

Figure 3.13: *Peak frequencies and amplitudes in the range of 0.16 Hz - 1.0 Hz. Symbols, lines, scales and colors as in figure 3.9*

the southwestern edge near the shore and northeastern edge of the LA basin. Measured spectral peak amplitudes in the Puente Hills are in the range of 1 - 3. The more detailed

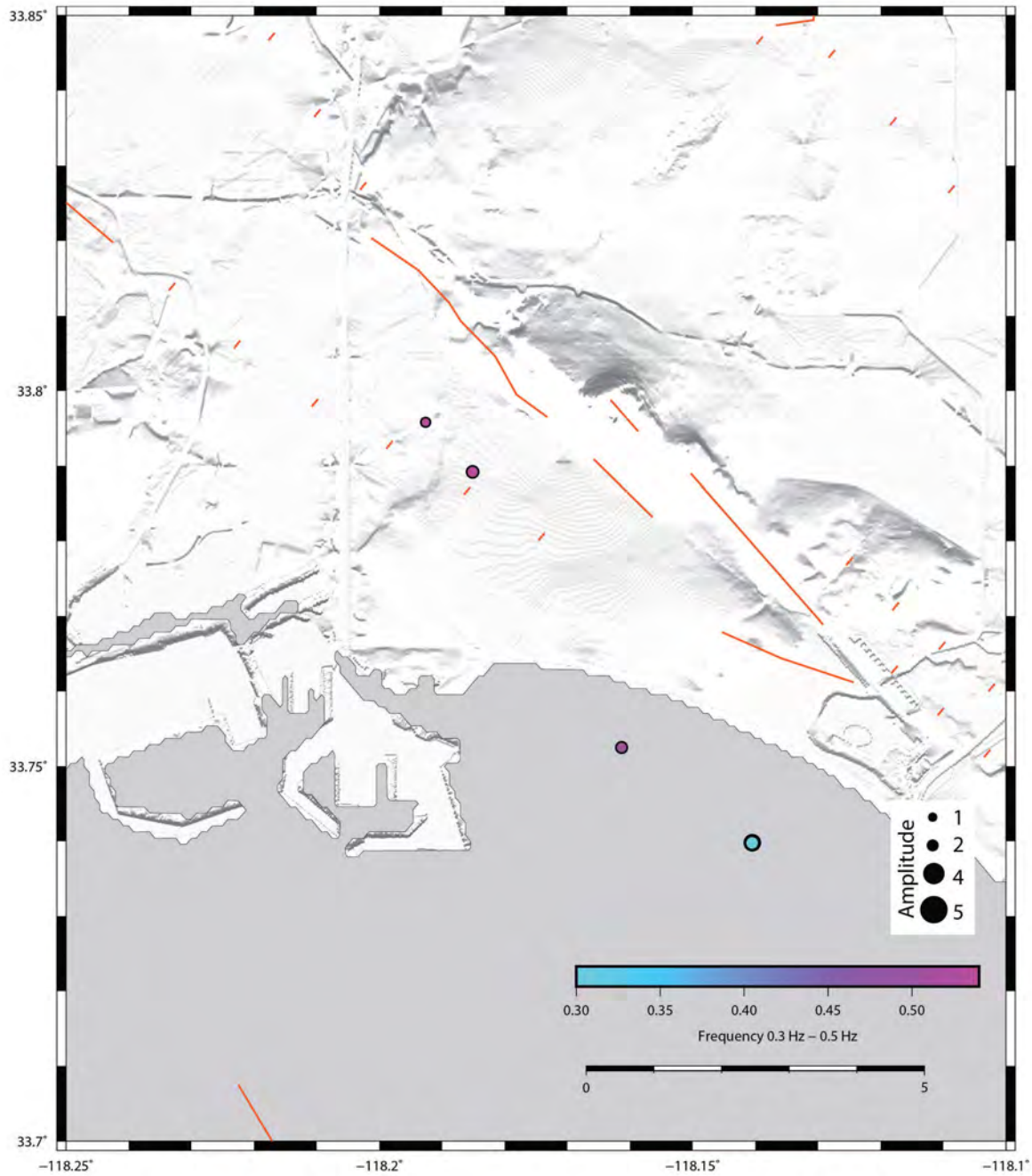

Figure 3.14: *More detailed map of the Long Beach area for peak frequencies and amplitudes in the range of 0.16 Hz - 1.0 Hz. Symbols, lines, scales and colors as in figure 3.9*

LASSIE regional map for the Long Beach area shows lower HVSR peak amplitudes of measured peak frequencies near the shore of the southwestern basin. This observation appears to suggest that these peaks are generated by a different type of subsurface structure than those of previous frequency groups, since the amplitude pattern is inconsistent.

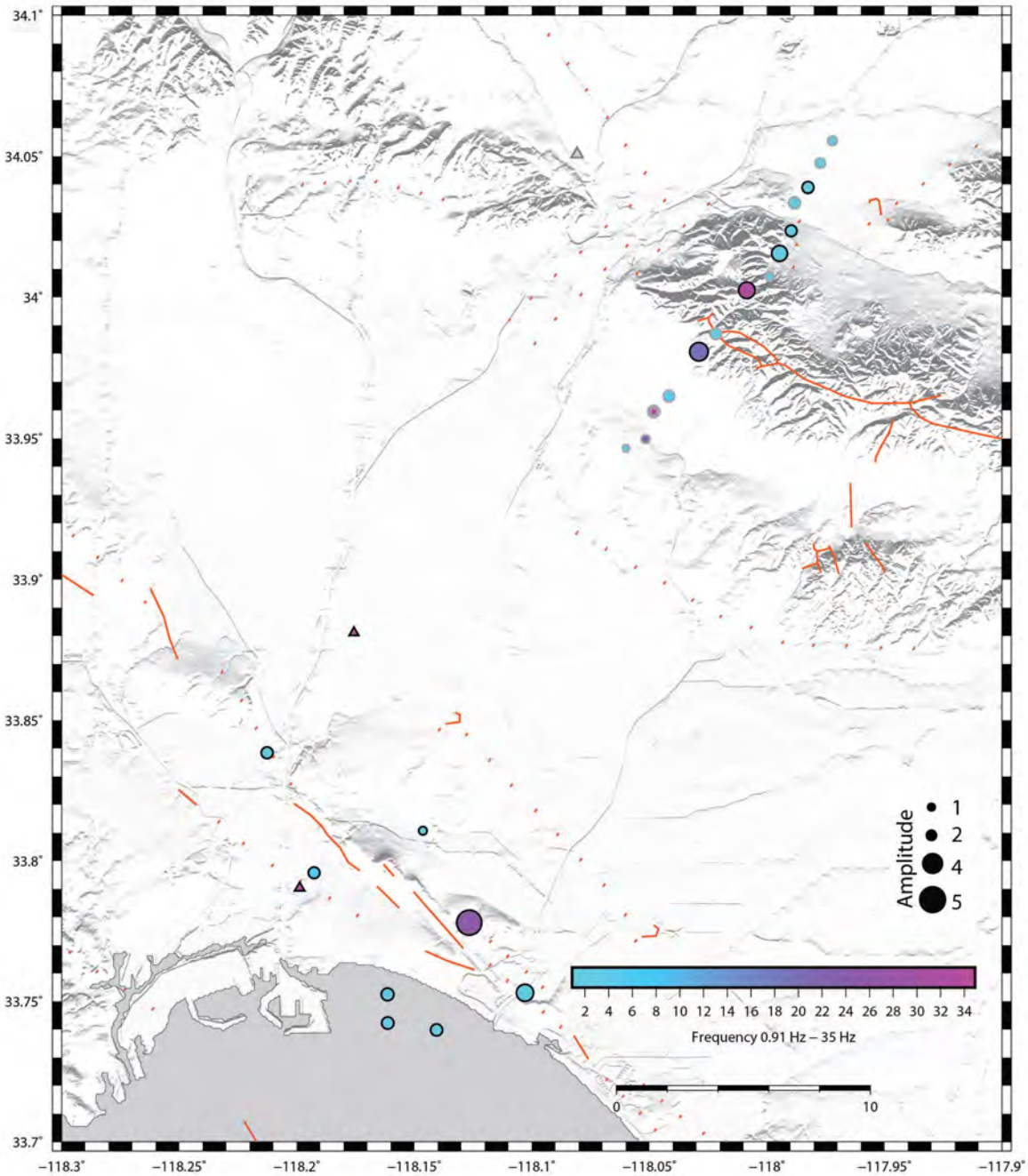

Figure 3.15: *Peak frequencies and amplitudes in the range greater than 1.0 Hz. Symbols, lines, scales and colors as in figure 3.9*

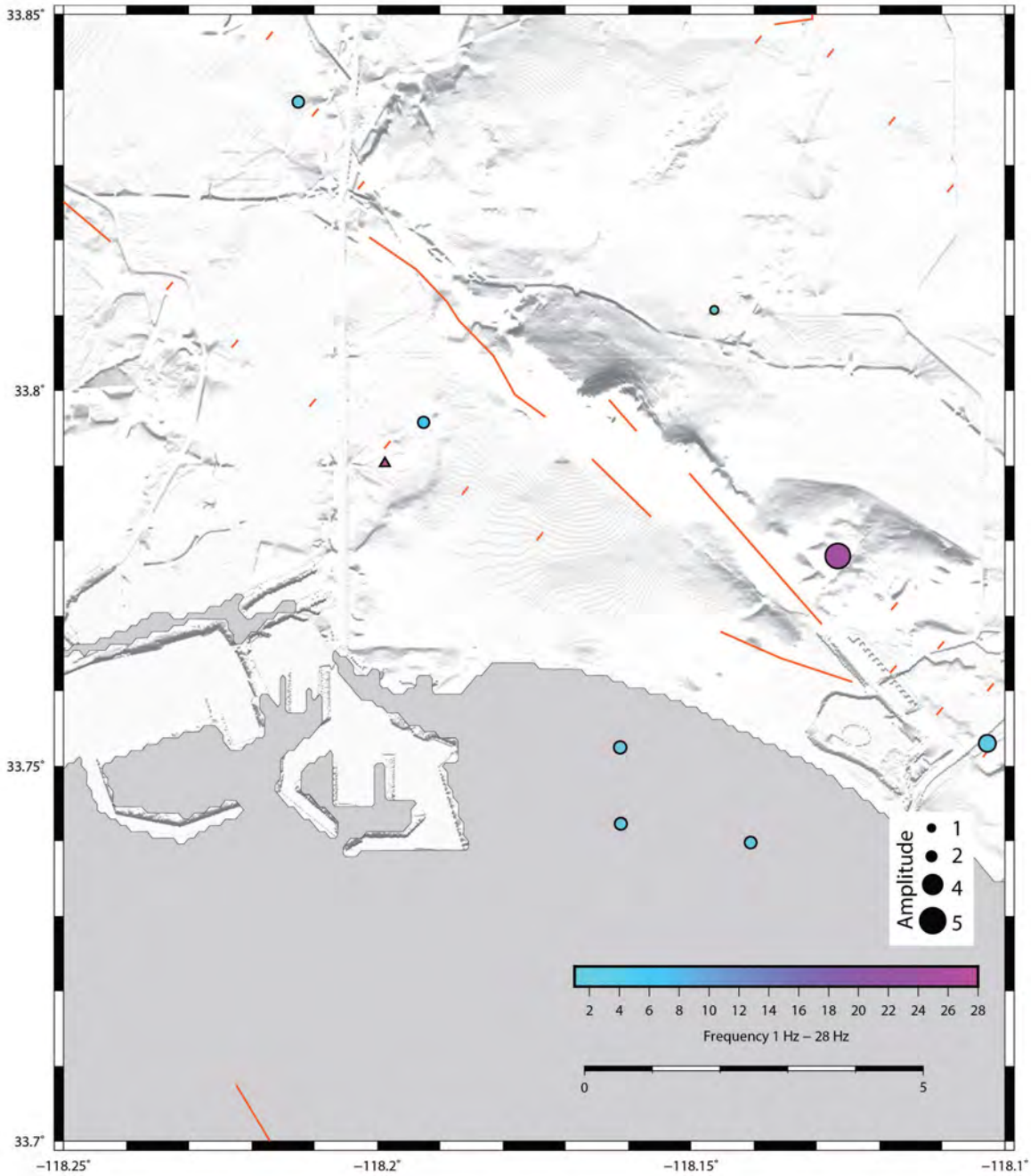

Figure 3.16: *More detailed map of the Long Beach area for peak frequencies and amplitudes greater than 1.0 Hz. Symbols, lines, scales and colors as in figure 3.9*

Chapter 4

Discussion

In this chapter we analyze, discuss and interpret our results in the context of previous investigations. We address first and second order results for resonance periods of the LA basin, the hazard this resonance may pose to structures, and use the resonance period in conjunction with a range of available shear wave velocity models to estimate the depth of the LA basin. We compare and contrast our results with several LA basin models.

4.1 Discussion of primary results

We observe several coherent sets of spectral ratio peaks for our data set of waveforms recorded by the LASSIE deployment, with one group of peaks that could most easily be tracked along the entire network in the frequency range of 0.085 Hz - 0.159 Hz. We should note that in our analysis, we also consider spectral peaks that do not meet sufficient criteria to be classified as "clear" peaks. However, due to the extraordinarily small spacing between our stations, we consider that peaks that may be traced along most of the network

should still be considered significant. The spectral peak amplitudes and peak frequencies both show variation across the LASSIE network, even between stations that are spaced only 1000 m apart, suggesting that the site response in this area varies on a very small scale and emphasizing the importance of microzonation.

We observe a dominant, laterally continuous, spectral peak frequency of approximately 0.10 Hz - 0.15 Hz across the Los Angeles basin. We have tested and established this peak frequency as a resonance frequency of the Los Angeles basin from our measurements based on the SESAME guidelines. These measurements are consistent with the work of Wald & Graves (1998) who used the 3D velocity model of southern California from Graves (1996) to calculate a theoretical resonance frequency of the LA basin at 10 seconds. It is important to note that we observe a similar spectral peak in this frequency range for 36 of 44 LA basin transect stations from the LASSIE network. This allows us to conclude that this peak is not an artifact generated from nearby sources, but indeed a stable feature in the spectral ratio functions.

4.1.1 Peak Amplitude

As described in Chapter 2 of this thesis, the SESAME project systematically compared peak amplitudes as determined by the HVSR and SPR methods, as shown in figure 2.4. They conclude from this comparison that the HVSR peak amplitude appears to be a lower bound for site amplification. Another common interpretation of the peak amplitude from the HVSR approach is to use the value as a proxy for the relative ground motion amplification to a hard rock site. Within the LASSIE network, the best representation of a ”hard

rock" site is the Tertiary sedimentary rocks located in the Puente Hills at the northeastern edge of the basin, as shown in figure 1.2. At these sites, the spectral amplitude is approximately 1.5 - 2 for the frequency range 0.085 Hz - 0.159 Hz. This value, although not equal to 1, is significantly lower than those measured in the LA basin. In conclusion, we will consider the peak spectral amplitudes a lower boundary of the site amplification relative to a hard rock site.

The LASSIE network was deployed on the following surface geologic units: Quaternary alluvium, Quaternary older alluvium, and Tertiary sedimentary rock. The measured amplitudes from the 0.085 Hz - 0.159 Hz frequency range show good correlation with the Tertiary sedimentary rock along the northeastern boundary of the LA basin. We observe a smaller spectral peak amplitude between 1.7 - 3 over and near the Tertiary rock compared to the average peak amplitude of 3.5 - 4 in the center of the basin. However, the change in peak amplitude is counterintuitive for the center of the basin and Long Beach, since commonly a thicker sedimentary layer is associated with higher amplification. Higher amplification was for example observed in the deepest part Mexico City basin by Lermo & Chavez - Garcia (1994). Ambient noise spectral ratios were compared for multiple locations inside and outside of the basin. Spectral peaks from the Mexico City basin exhibited peak amplitudes as high as 10. Since Mexico City was heavily affected during the 1985 earthquake due to ground motion amplification that was measured to have an ambient noise spectral peak amplitude of 10, an average spectral peak of 3.5 - 4 with some individual peaks with values greater than 5 from the LASSIE array would still pose a significant amplification risk.

4.1.2 Spectral peak frequencies

HVSR spectral peaks are associated with a strong acoustic impedance contrast between subsurface layers and have been shown in numerous other basin studies (e.g., Seht & Wohlenberg, 1999; Parolai et al., 2002; Özalaybey et al., 2011; Ho & Polet, 2015) to be related to the sediment basement contact. Other spectral peak frequencies are likely a representation of additional subsurface contacts. We calculate a simple forward prediction for a theoretical resonance frequency for the LASSIE array. We assume a simple two layer model, a soft sedimentary layer over hard bedrock, in which case the spectral peak indicates the fundamental period. The quarter wavelength function

$$f_0 = \frac{V_s}{4h} \tag{4.1}$$

may be then used to calculate a fundamental frequency, f_0, given an average S-wave velocity of the soil structure, V_s, and a depth to the bottom of the sedimentary layer, or basin, denoted by h. An example of this application is in Seht & Wohlenberg (1999). The basis of the quarter wavelength, λ, function comes from the relationship between the fundamental resonant period, f_0, and the first harmonic standing wave that extends from one node to an antinode.

The Southern California Earthquake Center (SCEC) Community Velocity Model, Harvard (CVM-H) by Plesch et al. (2007) and Plesch et al. (2009), as shown in figure 4.1, is used for our forward prediction of the fundamental frequency. We determine the basin depth in this model by analyzing the 1-D velocity profile of each station to identify the

jump in shear wave velocity that may be interpreted to represent the transition from soft basin sediments to bedrock.

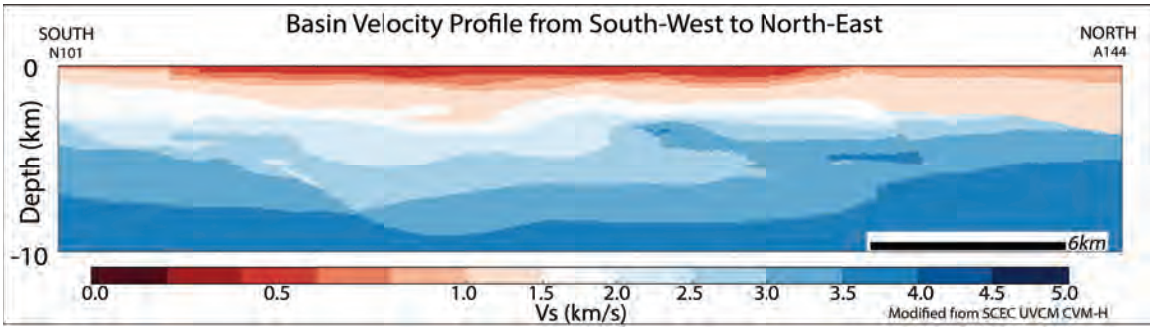

Figure 4.1: *2D velocity profile of the Los Angeles basin along the LASSIE transect from station N101 to A144 from Southern California Earthquake Center (SCEC) Community Velocity Model - Harvard (CVM-H) (Plesch et al., 2007) and (Plesch et al., 2009). This cross section shows a maximum basin depth of 10 km. Shear wave velocity is displayed as a color scale with the warm colors (red) as low velocity and the cool colors (blue) as high velocity.*

We determine a weighted velocity from the SCEC CVM-H for our calculation. The weighted velocity is the average velocity proportional to its depth in a 1-D velocity profile of the given site. We determine a weighted average velocity by taking the total sum average of velocities with respect to depth. From that velocity and the depth to the basin we can use equation 4.1 to determine a resonance frequency. We compare our forward prediction to our measured spectral peak frequencies. The HVSR peak frequency results from LASSIE are relatively at a higher frequency than the predicted results near the center of the basin as shown in figure 4.2. At the edge of the basin, the difference between the predicted and actual results is small. The differences between the HVSR measurements and values predicted from the CVM could be due to several different factors (or a combination of

these factors): the velocity model contains velocities that are too low in the center of the basin, the basin is too deep in the CVM model, the assumption of a simple two-layer model (commonly used in other HVSR basin studies) is too severe a simplification for a deep basin such as the LA basin, and therefore the method used in the calculation of the predicted peak frequency is not appropriate, or in the case of a large and deep basin as the LA basin, the resonance frequency is not determined by an S-wave bouncing up and down in this basin, but in fact may be the result of a different type of wave or a combination of different waves. It is however important to keep in mind that the HVSR results themselves are measurements of the actual peak frequencies and resonances of the LA basin, independent of any model.

Secondary intermittent spectral peaks

In some cases we also observe secondary peaks at lower and/or higher frequencies than the observed laterally continuous spectral peak frequency of approximately 0.10 Hz. Based on their location on the edge of the basin and in areas with topographic highs such as ridges, hills and mountains, the secondary intermittent peaks above 0.10 Hz may be explained by possible basin edge resonance, small-scale basins, and/or resonance due to topography as described by Spudich et al. (1996); J. A. Rial (1996); Bard & Riepl-Thomas (2000); Hough et al. (2011) and Assimaki & Jeong (2013). Intermittent low frequency peaks below 0.10 Hz may be attributed to internal layering within the LA basin. The 2.4 Hz resonance frequency in Whittier (Kawase & Aki, 1990), attributed to basin edge resonance, agrees with HVSR secondary peaks measured in that area.

4.1.3 Building resonance

A simple approximation for potential building resonance is provided by the equation

$$T = \frac{N_{stories}}{10} \tag{4.2}$$

where T is the period of resonance in seconds and $N_{stories}$ is the height of the structure in units of floors or stories. Tall buildings are located in downtown Los Angeles, which is on the northeastern border of the LA basin, north of the LASSIE line. Using equation 4.2 and our measured 0.10 Hz - 0.15 Hz resonance frequency that we determined to be representative for the downtown region, a building height of 66 - 100 floors would resonate at a frequency range of 0.10 Hz - 0.15 Hz. We assume the standard international building convention of one story to be approximately 10 ft or 3 m tall. Therefore, a structure of 66 - 100 floors is approximately 200 m - 300 m tall. Eleven tall structures in the downtown area are within that range of height. Therefore, these buildings would be expected to be severely affected by seismic energy that propagates into the LA basin at a period of 6 to 10 seconds, since both the building and the soil column beneath the building would resonate and amplify these motions, similarly to buildings in Mexico City during the 1985 Mexico City earthquake. Ground motions at these periods are expected to be produced in the LA basin by the propagation of surface waves of large earthquakes at regional distances, such as a significant event on the Southern San Andreas Fault.

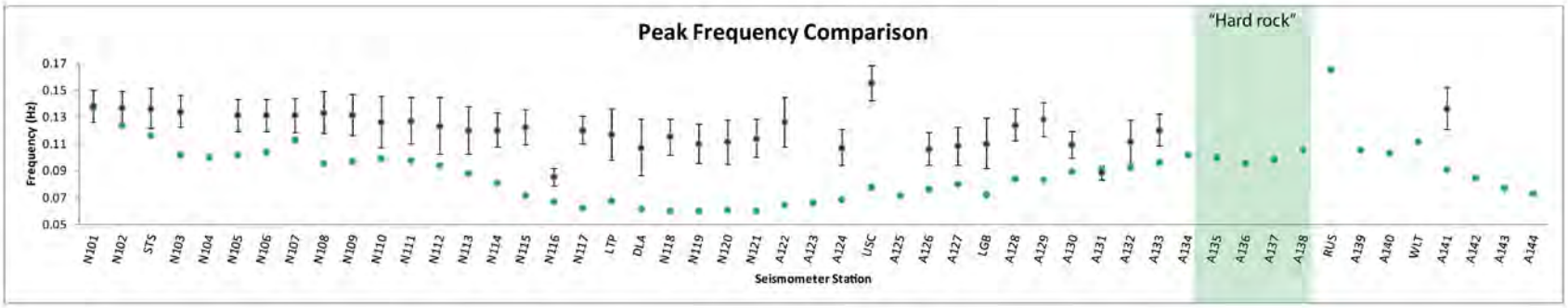

Figure 4.2: *Spectral ratio peak frequencies shown as blue circles with the error bars indicating their standard deviation, compared to the predicted frequencies, shown as green circles.*

4.2 Comparison to basin models

We can also use the quarter wavelength function, equation 4.1, with our measurements of spectral peak frequencies to constrain the basin depth in combination with average velocities extracted from profiles from the CVM-H. In this section, we concentrate our effort on the LA basin transect portion of the LASSIE network since we are interested in characterizing the basin depth and 2-D basin structure shape. The fundamental peak frequency can be interpreted as a physical representation of resonance due to the presence at depth of an interface of high impedance contrast. Previous microtremor HVSR basin studies used equation 4.1 to calculate the basin depth (Seht & Wohlenberg, 1999; Parolai et al., 2002), and Özalaybey et al. (2011) from spectral peaks determined for stations inside and around basins. However, most, if not all, of these studies were carried out in basins that were significantly smaller and shallower than the LA basin. This likely means that shear wave velocity gradients with depth due to compression of sediments, and layering within the basin itself in general, does not play as significant a role as it might in the case of the LA basin, and inherent simplifications in using this approach may be more valid. We also analyze other spectral peaks that most likely are produced by impedance contrasts within the basin, between sedimentary layers.

4.2.1 Basin depth

We extract the weighted velocity of the soil column beneath each LASSIE station in the LA basin transect for basin depth estimation using the quarter wavelength function. We used abrupt velocity increases in the 1-D velocity profile at each station from the CVM-H

model to determine the depth of the basin in the model, which is needed as the lower depth limit for the initial estimate of weighted velocity. We then compare our basin depth estimates with the model in figure 4.3 developed by Yerkes et al. (1965) from his investigation to geological characterize the Los Angeles basin structure. The calculated basin depths from the measured spectral ratio peak frequencies are not matched by the absolute basin depth values from Yerkes' et al. (1965) model. However, they do follow a similar generalized basin shape, exhibiting shallow edges and greater depths in the same area where the deepest portion of the basin is proposed by Yerkes et al. (1965).

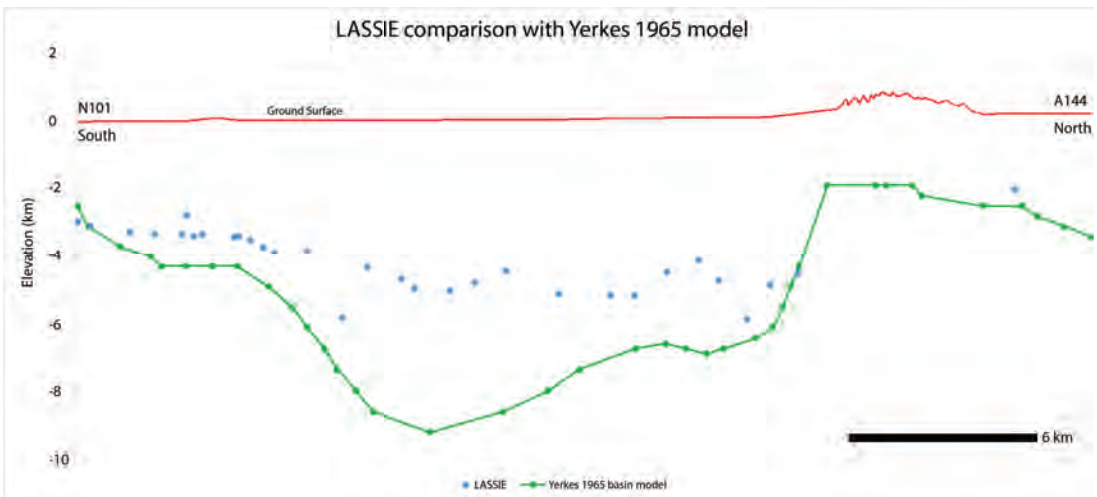

Figure 4.3: *Modified Yerkes et al. (1965) model of the sediment bedrock interface, shown in green, overlain with surface elevation modified from Google Earth (2016) in red and initial calculated depth to interface for LASSIE stations shown with blue dots.*

Subsequently, we also compare our basin depth results with the basin model of sedimentary layers proposed by Wright (1991), shown in figure 4.4. Wright identified two sedimentary layers within the basin, the Reppetto (4.5 Ma) and Mohnian (14 Ma) formation. We are particularly interested in also comparing our depth estimates with any

contrast between shallower sedimentary structures. Near the basin southwestern edge the calculated depths correlate well with the base of Mohnian formation. However, towards the center of the basin, the calculated basin depth estimates are a better match with the base of the Repetto formation. If we assume that the assumptions made in our calculations are correct, this pattern could suggest that the HVSR spectral peaks near the deepest part of the basin may not be due to a sediment/bedrock contrast, but may be the result of a shallower contrast within the sediments themselves. Alternative explanations could be: poor representation of possible high shear wave velocities within the basin, an overestimation of the total CVM-H basin depth, an over simplification of the deep basin model, and the strong assumption that the resonance period is only defined by a vertically inclined single mode shear wave.

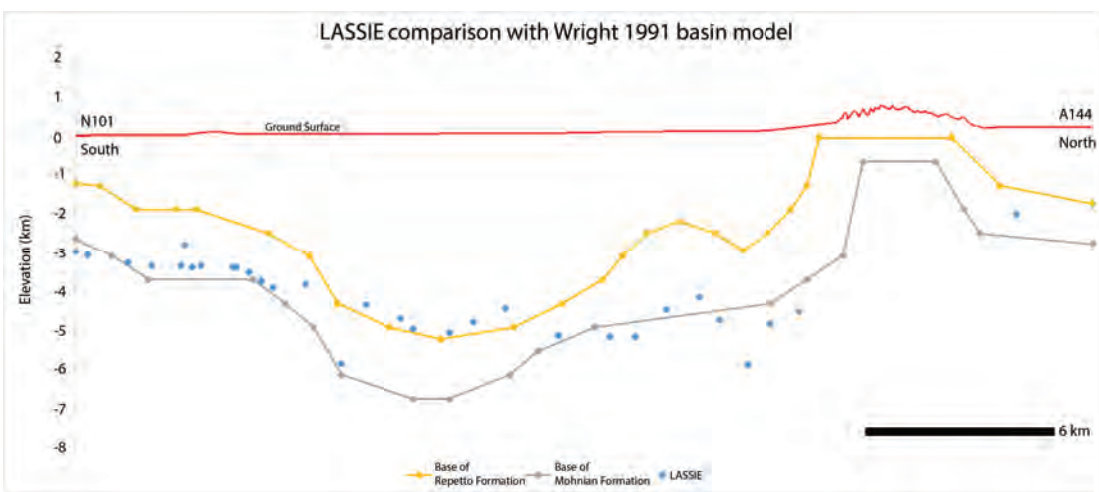

Figure 4.4: *Modified Wright (1991) model of base of the Repetto formation shown in yellow and Mohnian formation shown in grey overlain with surface elevation modified from Google Earth (2016) shown in red and calculated depth to interface for LASSIE stations represented with blue dots.*

We also interpret our results in the context of another recent model proposed by Ma (2016), determined by a tomographic shear wave velocity inversion. This study used the full waveform data from the LASSIE array for their investigation. We compare our calculated basin depth results with the tomographic velocity model developed by Ma (2016) in figure 4.5. Our estimates for the depth of the contrast that is responsible for generating the peak HVSR frequency appears to correlate well with the velocity model, showing the calculated interface depth to be associated with shear wave velocities in the range of 2.2 km/s - 3.0 km/s. This velocity range is the generalized approximate maximum shear wave velocity for the sedimentary material that overlies hard crystalline bedrock.

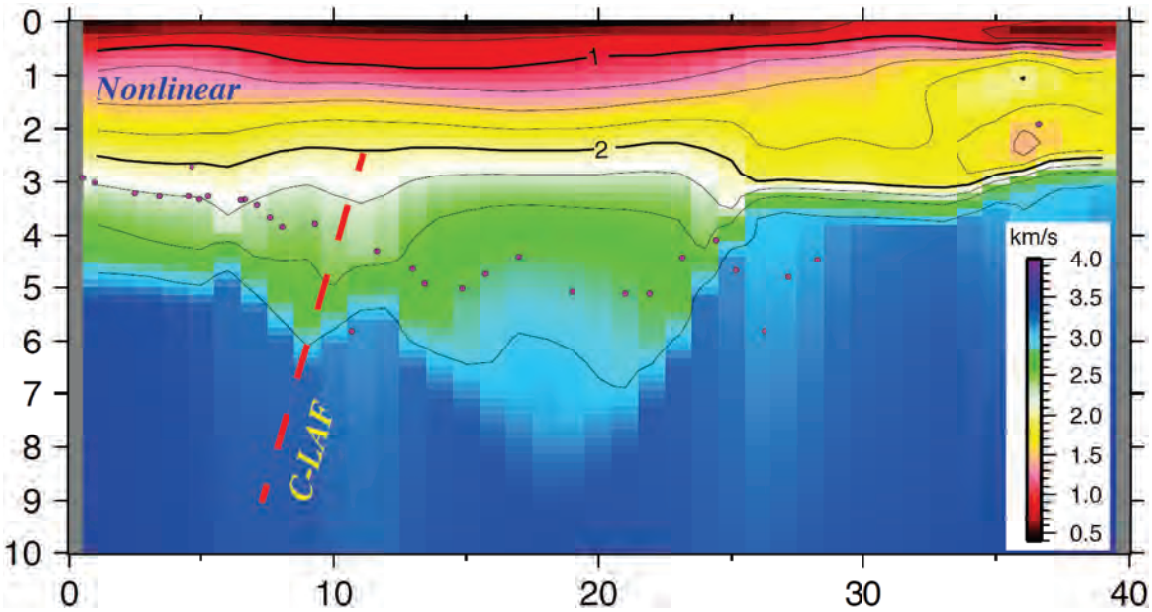

Figure 4.5: *Ma (2016) non-linear shear wave inversion velocity model. Color gradient shows shear wave velocity with warm colors representing slow velocity and cool colors representing fast velocities. The pink dots represent the calculated basin depth from the HVSR peak frequencies of the LA basin transect portion of the LASSIE array.*

4.2.2 Comparison of predictions and measurements

In the previous sections, our measured results do not agree with existing velocity models. However, in our calculations of the weighted velocity, we used the CVM model basin depth as the lower bound of the depth range, which is incorrect if the resulting basin depth is markedly different. We recalculate the weighted velocity based on the "new" basin depth, use this velocity and the quarter-wavelength function to recalculate the interface depth and continue this process using an iterative approach, until a stable interface depth is achieved. The final iterative results are displayed at depths between 1 km and 3 km as shown in figure 4.6. A few outlying points are due to inclusion of secondary intermittent spectral peaks that did not pass the required criteria for clear peaks. The final iteration results are even more different from the Yerkes et al. (1965) model. To further illustrate the importance of the specifics of the velocity model, we compare results using two similar velocity models near the center of the basin as shown in 4.7. We varied the velocity models and the peak frequencies, using the parameters for two stations in the center of the basin as an example and found that, although the velocity models appear quite similar upon first glance, they result in interface depths that differ by more than 1 km. We can conclude that, given the sensitivity of this calculation to the details of the velocity model, we cannot determine well constrained basin depths using this approach.

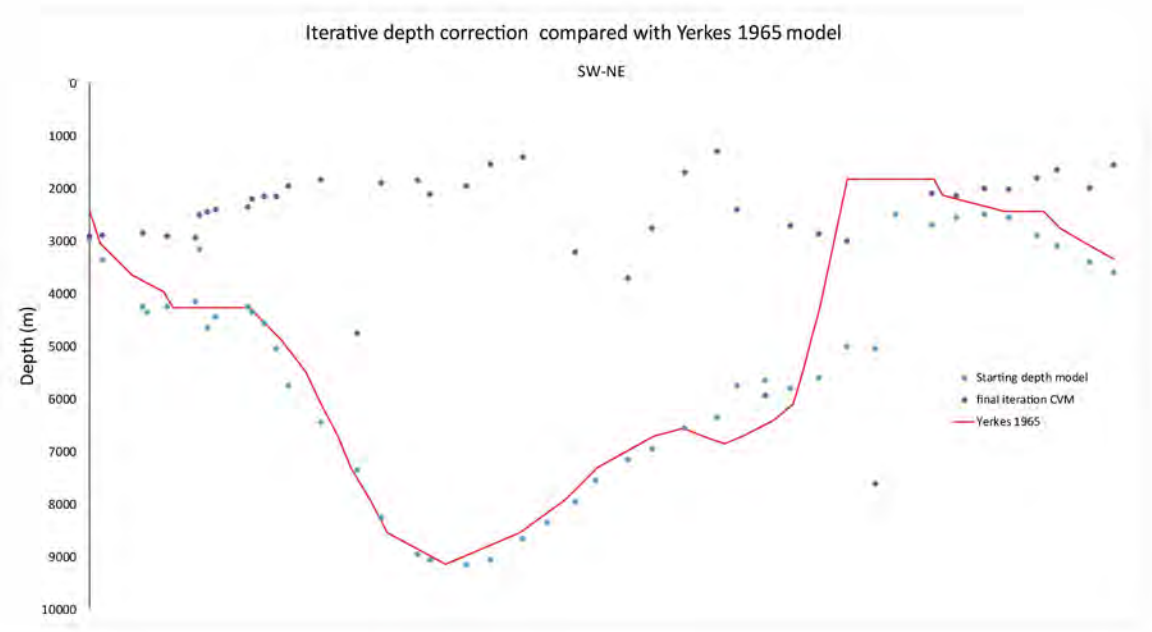

Figure 4.6: *The starting depth model, determined from 1-D profiles through the CVM-H from Plesch et al. (2007) and Plesch et al. (2009) in blue and the Yerkes et al. (1965) basin model in red. Our final iterative results, shown in purple, plot at a very shallow depth in comparison to the starting model.*

Parameters	A122	A124	A122	A122
f_0	0.126 Hz	0.107 Hz	0.126 Hz	0.107 Hz
h_{start}	8650 m	7950 m	7000 m	8650 m
$V_{A_{CVM}}$	2224 m/s	2173m/s	1987 m/s	2224 m/s
$h_{est_1} = \frac{V_{A_{CVM}}}{4f_0}$	4400 m	5100 m	3950 m	5200 m
$V_{B_{CVM}}$	1475 m/s	1716 m/s	1363 m/s	1655 m/s
$h_{est_2} = \frac{V_{B_{CVM}}}{4f_0}$	2950 m	4000 m	2700 m	3850 m
$h_{est_{Final}} = \frac{V_{\infty_{CVM}}}{4f_0}$	1400 m	3300 m	1400 m	2200 m

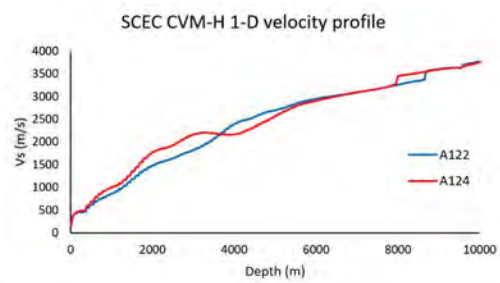

Figure 4.7: *Investigation of the iterative velocity model correction. Two similar LASSIE station CVM-H 1-D velocity profiles are shown on the right panel. The left panel displays the results of the iterative basin depth calculation when varying the velocity model and the peak frequency between these two stations, located within a few kms.*

4.3 Future work

Additional research can help provide more in depth interpretation of the HVSR measurements from this study. One approach would be to implement the HVSR inversion code developed by García-jerez et al. (2016). This code is an algorithm that, under the assumptions that the ambient noise field is comprised of Love, Rayleigh, P, and S waves, can invert the spectral ratio measurements for a velocity profile with depth, given a reasonably close starting model. The software also produces a predicted spectral ratio curve based on this velocity profile, for comparison with the original measurements. Although this inversion is non-unique, given the availability of models of the LA basin that are considered to be reasonably well constrained as starting models, we would expect that this approach will help constrain the depths of the major acoustic impedance contrasts in the basin. Further investigation should attempt to correlate our measured peak frequencies to calculated basin depths with the results of this code.

Future research could also include an investigation of the azimuthal variations in the HVSR curves, a technique used by Uebayashi et al. (2008) and Matsushima et al. (2014), particularly useful near basin edges, which has shown that these types of variations may be used to detect 2-D basin structures.

It would also be instructive to relate the HVSR results to damage patterns for historical earthquakes in the greater LA basin area, such as the Whittier earthquake, Northridge earthquake, and Long Beach earthquake to see if locations of unusually high damage correspond to relatively high amplification values.

Chapter 5

Conclusions

To study the variation of site effects on a small scale across the Los Angeles basin we participated in the installation of 73 broadband seismometers with a seismometer spacing of 1 km for the temporary LASSIE network and collected full waveform data to carry out a spectral ratio analysis, based on ambient noise. We extract spectral peak frequencies and peak amplitudes from the HVSR graphs and interpret these measurements as resonance frequencies and a lower limit for ground motion amplification.

We observe a primary spectral peak frequency that is laterally coherent, with slight variations in its frequency range from 0.10 Hz to 0.15 Hz, that we interpret to be a resonance frequency for the LA basin. We also observe several additional sets of peak frequencies, some only appearing near the basin edge or near topographic features, within a higher frequency range, for example, 10 neighboring stations with spectral peaks in the frequency range of 0.17 Hz - 0.27 Hz. Based on the location of these measurements of intermittent secondary peaks, on the edge of the basin and in areas with topographic highs such as ridges, hills and mountains, they may be explained using basin edge resonance, the

presence of small scale basins, and/or topographic effects.

The spectral peak amplitudes of the primary peaks inside the LA basin tend to have a higher value on sites over deep sediments compared to sites over sedimentary rocks. However, these peak amplitude values do not follow a trend based on sediment depth. We observe the potential of higher ground motion amplification within the basin than outside of the basin by up to a factor of 5.

The spectral peak amplitudes and peak frequencies both show variation across the LASSIE network, even between stations that are spaced only 1000 m apart, suggesting that the site response in this area varies on a very small scale and emphasizing the importance of microzonation. The average LA basin resonance frequency range of 0.10 - 0.15 Hz is potentially devastating for buildings approximately 200 m - 300 m tall, which have resonance frequencies that fall in that same range. Large earthquakes at regional distances, such as a significant event on the Southern San Andreas Fault, are expected to produce significant energy in the LA basin in this range of periods through the propagation of seismic surface waves.

Assuming a simplified model of a sedimentary layer over a bedrock half-space, we calculate the predicted resonance frequency for the SCEC CVM-H model using the quarter wavelength equation and find that the predicted resonance frequencies are consistently lower than our measurements. We also calculate interface depths from our measured resonance frequencies using a similar approach. We find that the predicted interface depth from our primary peak frequencies does not agree with the depth to the LA basin from a variety of models. Possible explanations for the discrepancy between our measurements and the

predicted resonance frequencies include: the presence of a significantly higher shear wave velocity within the basin than included in the model, an overestimation of the basin depth in the model, an oversimplification of the method used to calculate predicted values and the assumption that the resonance is due to a vertically inclined single mode shear wave.

References

Abbott, R. E. (2005). Basin Amplification of Seismic Waves in the City of Pahrump, Nevada. *Sandia Report. United States. Department of Energy*, *SAND2005*(7005).

Arai, H., & Tokimatsu, K. (2000). Effects of Rayleigh and Love waves on microtremor H/V spectra. Paper Presented at Proceedings of the 12th World Conference on Earthquake Engineering. *New Zealand Society for Earthquake Engineering, Auckland*, 2232–2240.

Ashford, S. A., Jakrapiyanun, W., & Lukkunaprasit, P. (2000). Amplification of earthquake ground motions in Bangkok. *Proceedings of the 12th World Conference on Earthquake Engineering, Auckland, New Zealand*.

Assimaki, D., & Jeong, S. (2013). Ground-motion observations at hotel Montana during the M 7.0 2010 Haiti earthquake: Topography or soil amplification? *Bulletin of the Seismological Society of America*, *103*(5), 2577–2590. doi: 10.1785/0120120242

Asten, M. W. (1978). Geological control on the three-component spectra of Rayleigh-wave microseisms. *Bulletin of the Seismological Society of America*, *68*(6), 1623–1636.

Bard, P.-Y. (1999). Microtremor measurement : a tool for site effect estimation. *The effects of surface geology on seismic motion*, *3*, 1251–1279.

Bard, P.-Y., Atakan, K., Azzara, R. M., Cara, F., Cultrera, G., Dimitriou, P., ... Others (2004). Site effects assessment using ambient excitations (SESAME). *Europeam Commission - Research General Directorate*, *WP04*(Project No. EVG1-CT-2000-00026 SESAME).

Bard, P.-Y., & Bouchon, M. (1985). The Two-Dimensional Resonance of Sediment-Filled Valleys. *Bulletin of the Seismological Society of America*, *75*(2), 519–541.

Bard, P.-Y., Jongmans, D., Ohrnberger, M., & Wathelet, M. (2005). Site effects assessment using ambient excitations (SESAME). *Europeam Commission - Research General Directorate*, *Final Repo*(Project No. EVG1-CT-2000-00026 SESAME).

Bard, P.-Y., & Riepl-Thomas, J. (2000). Wave propagation in complex geological structures and their effects on strong ground motion. *Wave motion in earthquake eng*, 37–95.

Bard, P.-Y., & SESAME Participants. (2004). The SESAME project: an overview and main results. *Proceedings of the 13th world conference on earthquake engineering, Vancouver*.

Beck, J. L., & Hall, J. F. (1986). Factors contributing to the catastrophe in Mexico City during the earthquake of September 19, 1985. *Geophysical Research Letters*, *13*(6), 593–596.

Beresnev, I. A., Field, E. H., Van Den Abeele, K., & Johnson, P. A. (1998). Magnitude of nonlinear sediment response in Los Angeles Basin during the 1994 Northridge, California, Earthquake. *Bulletin of the Seismological Society of America*, *88*(4), 1079–1084.

Bilodeau, W. L., Bilodeau, S. W., Gath, E. M., Oborne, M., & Proctor, R. J. (2007). Geology of Los Angeles, California, United States of America. *Environmental & Engineering Geoscience*, *13*(2), 99–160.

Bonnefoy-Claudet, S., Baize, S., Bonilla, L. F., Berge-Thierry, C., Pasten, C., Campos, J., … Verdugo, R. (2009). Site effect evaluation in the basin of Santiago de Chile using ambient noise measurements. *Geophysical Journal International*, *176*(3), 925–937. doi: 10.1111/j.1365-246X.2008.04020.x

Bonnefoy-Claudet, S., Cornou, C., Kristek, J., Ohrnberger, M., Wathelet, M., Bard, P.-Y., … Cotton, F. (2004). Simulation of seismic ambient noise: I. Results of H/V and array techniques on canonical models. *Proceedings of the 13th world conference on earthquake engineering, Vancouver*.

Brady, A., Etheredge, E., & Porcella, R. (1988). The Whittier Narrows, California earthquake of October 1, 1987-Preliminary assessment of strong ground motion records. *Earthquake Spectra*, *4*(1), 55–74.

Cara, F., Di Giulio, G., Milana, G., Bordoni, P., Haines, J., & Rovelli, A. (2010). On the stability and reproducibility of the horizontal-to-vertical spectral ratios on ambient noise: the case study of Cavola, northern Italy. *Bulletin of the Seismological Society of America*, *100*(3), 1263—-1275.

Clemente-Chavez, A., Zúñiga, F. R., Lermo, J., Figueroa-Soto, A., Valdés, C., Montiel, M., … Arroyo, M. (2014). On the behavior of site effects in central Mexico (the Mexican volcanic belt MVB), based on records of shallow earthquakes that occurred in the zone between 1998 and 2011. *Natural Hazards and Earth System Sciences Discussions*, *14*(6), 1391–1406. doi: 10.5194/nhess-14-1391-2014

Davis, T. L., Namson, J., & Yerkes, R. F. (1989). A cross section of the Los Angeles Area: Seismically active fold and thrust belt, The 1987 Whittier Narrows earthquake, and earthquake hazard. *Journal of Geophysical Research: Solid Earth*, *94*(B7), 9644–9664. doi: 10.1029/JB094iB07p09644

Denolle, M. A. (2014). Seismic hazard analysis using the ambient seismic field. *PhD Dissertation. Stanford University*.

Dolan, J. F., Christofferson, S. A., & Shaw, J. H. (2003). Recognition of paleoearthquakes on the Puente Hills blind thrust fault, California. *Science*, *300*(5616), 115–118. doi: 10.1126/science.1081940

Ducellier, A., Kawase, H., & Matsushima, S. (2013). Validation of a new velocity structure inversion method based on horizontal-to-vertical (H/V) spectral ratios of earthquake motions in the Tohoku Area, Japan. *Bulletin of the Seismological Society of America*, *103*(2 A), 958–970. doi: 10.1785/0120120214

Eaton, J. (1923). Structure of the Los Angeles basin and environs. *Oil Age*, *20*.

Eissler, H., Astiz, L., & Kanamori, H. (1986). Tectonic Setting and Source Parameters of the September 19,1985 Michoacan, Mexico Earthquake. *Geophysical Research Letters*, *13*(6), 569–572.

Etheredge, E., Porcella, R., Johnson, D., Salsman, M., Ellis, F., Acosta, A., ... Others (1987). Strong-motion data from the October 1, 1987 Whittier Narrows earthquake. *US Geological Survey. Open File Report*(87-616).

Ferguson, R., & Willis, C. (1924). Dynamics of oil-field structure in southern California. *AAPG Bulletin*, *8*(5), 576–583.

Field, N., Jones, L., Jordan, T., Benthien, M., & Wald, L. (2001). Earthquake Shaking-Finding the" Hot Spots". *US Dept. of the Interior, US Geological Survey. Fact Sheet*(001-01).

Flores-Estrella, H., Yussim, S., & Lomnitz, C. (2007). Seismic response of the Mexico City Basin: A review of twenty years of research. *Natural Hazards*, *40*(2), 357–372. doi: 10.1007/s11069-006-0034-6

Franco-Villafañe, J. A., Flores, J., Mateos, J. L., Méndez-Sánchez, R. A., Novaro, O., & Seligman, T. H. (2011). Novel doorways and resonances in large-scale classical systems. *EPL (Europhysics Letters)*, *94*(3), 1–5. doi: 10.1209/0295-5075/94/30005

Frankel, A. D., Carver, D. L., & Williams, R. a. (2002). Nonlinear and linear site response and basin effects in Seattle for the M 6.8 Nisqually, Washington, earthquake. *Bulletin of the Seismological Society of America*, *92*(6), 2090–2109. doi: 10.1785/0120010254

Frantti, G. (1963). The nature of high-frequency earth noise spectra. *Geophysics*, *28*(4), 547–562.

Frantti, G., Willis, D., & Wilson, J. T. (1962). The spectrum of seismic noise. *Bulletin of the Seismological Society of America*, *52*(1), 113–121.

García-jerez, A., Piña-flores, J., Sánchez-sesma, F. J., Luzón, F., & Perton, M. (2016). A computer code for forward calculation and inversion of the H / V spectral ratio under the diffuse field assumption. *Computers & Geosciences*. doi: 10.1016/j.cageo.2016.06.016

Graham, S. A. (1987). Tectonic controls on petroleum occurrence in central California. *Cenozoic basin development of coastal California*, *6*, 47–63.

Graves, R. W. (1995). Preliminary analysis of long-period basin response in the Los Angeles region from the 1994 Northridge earthquake. *Geophysical Research Letters*, *22*(2), 101–104.

Graves, R. W. (1996). Simulating seismic wave propagation in 3D elastic media using staggered-grid finite differences. *Bulletin of the Seismological Society of America*, *86*(4), 1091–1106.

Guillier, B., Chatelain, J.-L., Bonnefoy-Claudet, S., & Haghshenas, E. (2007). Use of Ambient Noise : From Spectral Amplitude Variability to H / V Stability. *Journal of Earthquake Engineering*, *11*(6), 925–942. doi: 10.1080/13632460701457249

Gutenberg, B. (1957). Effects of ground on earthquake motion. *Bulletin of the Seismological Society of America*, *47*(3), 221–250.

Gutenberg, B. (1958). Two types of microseisms. *Advances in Geophysics*, *5*, 53–92.

Hafner, K., & Clayton, R. W. (2001). The Southern California Earthquake Data Center (SCEDC). *Seismological Research Letters*, *72*(6), 705–711.

Hall, J. F., & Beck, J. L. (1986). Structural damage in Mexico city. *Geophysical Research Letters*, *13*(6), 589–592.

Hartzell, S., Leeds, A., Frankel, A., & Michael, J. (1996). Site response for urban Los Angeles using aftershocks of the Northridge earthquake. *Bulletin of the Seismological Society of America*, *86*(1B), S168—-S192.

Hauksson, E., & Haase, J. S. (1997). Three-dimensional VP and VP/VS velocity models of the Los Angeles basin and central Transverse Ranges, California. *Journal of Geophysical Research*, *102*(B3), 5423–5453. doi: 10.1029/96JB03219

Ho, K. K., & Polet, J. (2015). Mapping Site Response Parameters on Cal Poly Pomona Campus Using the Spectral Ratio Method. *MSc Thesis. California State Polytechnic University, Pomona*.

Hough, S. E., Yong, A., Altidor, J. R., Anglade, D., Given, D., & Mildor, S. L. (2011). Site characterization and site response in Port-Au-Prince, Haiti. *Earthquake Spectra*, *27*(S1), 137–155. doi: 10.1193/1.3637947

Hruby, C. E., & Beresnev, I. a. (2003). Empirical corrections for Basin effects in stochastic ground-motion prediction, based on the Los Angeles basin analysis. *Bulletin of the Seismological Society of America*, *93*(4), 1679–1690. doi: 10.1785/0120020121

Husker, A. L., Kohler, M. D., & Davis, P. M. (2006). Anomalous seismic amplitudes measured in the Los Angeles basin interpreted as a basin-edge diffraction catastrophe. *Bulletin of the Seismological Society of America*, *96*(1), 147–164. doi: 10.1785/0120040216

Imamura, A. (1913). Seismic Intensity Distribution in Tokyo and Osaka. *Report of the Imperial Earthquake Investigation Committee*, *77*, 17–42.

Ingersoll, R. V., & Rumelhart, P. E. (1999). Three-stage evolution of the Los Angeles basin, southern California. *Geology*, *27*(7), 593–596.

Jennings, C. W., Strand, R. G., Rogers, T. H., & Boylaw, R. (1977). Geologic map of California. *Division of Mines and Geology*.

Kagami, H., Duke, C. M., Liang, G., & Ohta, Y. (1982). Observation of 1 to 5 second microtremors and their application to earthquake engineering. Part II. Evaluation of site effect upon seismic wave amplification due to extremely deep soil deposits. *Bulletin of the Seismological Society of America*, *72*(3), 987–998.

Kagami, H., Okada, S., Shiono, K., Daravinski, M. O., Daeavinski, M., & Mal, A. (1986). Observation of 1-to 5-second microtremors and their application to earthquake engineering. Part III. A two-dimensional study of site effects in the San Fernando Valley. *Bulletin of the Seismological Society of America*, *76*(6), 1801–1812.

Kawase, H., & Aki, K. (1990). Topography effect at the critical SV-wave incidence Possible explanation of damage pattern by the Whittier Narrows, California, earthquake of 1 October 1987. *Bulletin of the Seismological Society of America*, *80*(1), 1–22.

Kleinpell, R. M. (1938). Miocene Stratigraphy of California. *AAPG*, *450*.

Kohler, M. D., Kerr, B. C., & Davis, P. M. (2000). The 1997 Los Angeles Basin Passive Seismic Experiment: A Dense, Urban Seismic Array to Investigate Basin Lithospheric Structures. *US Department of the Interior, US Geological Survey*, *Open-File*(00-148).

Koller, M. G., Chatelain, J.-L., Guillier, B., Duval, A.-M., Atakan, K., Lacave, C., & Bard, P.-Y. (2004). Practical user guidelines and software for the implementation of the H/V ratio technique: measuring conditions, processing method and results interpretation. *Proceedings of the 13th world conference in earthquake engineering, Vancouver*.

Konno, K., & Ohmachi, T. (1998). Ground-motion characteristics estimated from spectral ratio between horizontal and vertical components of microtremor. *Bulletin of the Seismological Society of America*, *88*(1), 228–241.

Kulp, J. L., Tryon, L. E., Eckelmen, W. R., & Snell, W. A. (1952). Lamont natural radiocarbon measurments II. *Science*, *116*, 409–414.

Lachet, C., & Bard, P. Y. (1994). Numerical and Theoretical Investigations on the Possibilities and Limitations of Nakamura's Technique. *Journal of the Physical Earth*, *42*, 377–397.

Lermo, J., & Chavez - Garcia, F. J. (1994). Are microtremors useful in site response evaluation? *Bulletin of the Seismological Society of America*, *84*(5), 1350–1364.

Lindh, A. G. (1983). Preliminary assessment of long-term probabilities for large earthquakes along selected fault segments of the San Andreas fault system in California. *U.S. Geological Survey*, *Open-File*(83-63).

Longuet-Higgins, M. S. (1950). A theory of the origin of microseisms. *Philosophical Transactions of the Royal Society of London A: Mathematical, Physical and Engineering Sciences*, *243*(857).

Louie, J. N. (2006). Improving Next-Generation Attenuation Models with Shear-Velocity Measurements at All TriNet and Strong-Motion Stations in LA. *Final Technical Report University of Nevada Seismological Laboratory*, *05HQGR0078*.

Louie, J. N. (2007). Shear-wave velocity map for California: Collaborative Research with CGS, and UNR. *US Geological Survey Technical Report*, *07HQGR0029*.

Ma, Y. (2016). Imaging the earth with ambient noise and earthquakes. *PhD Dissertation. California Insitution of Technology*.

Ma, Y., & Clayton, R. W. (2016). Structure of the Los Angeles Basin from ambient noise and receiver functions. *Geophysical Journal International*, *206*, 1645–1651. doi: 10.1093/gji/ggw236

Ma, Y., Clayton, R. W., & Li, D. (2016). Higher-mode ambient-noise Rayleigh waves in sedimentary basins. *Geophysical Journal International*, *206*, 1634–1644. doi: 10.1093/gji/ggw235

Magistrale, H., McLaughlin, K., & Day, S. (1996). A geology-based 3D velocity model of the Los Angeles basin sediments. *Bulletin of the Seismological Society of America*, *86*(4), 1161–1166.

Mahdyiar, M. (2002). Are NEHRP and Earthquake-based Site Effects in Greater Los Angeles Compatible? *Seismological Research Letters*, *73*(1), 39–45. doi: 10.1785/gssrl.73.1.39

Matsushima, S., Hirokawa, T., Martin, F. D., Kawase, H., & SánchezSesma, F. J. (2011). The effect of lateral heterogeneity on H/V spectral ratio of microtremors inferred from observation and synthetics. *4th IASPEI / IAEE International Symposium, University of California Santa Barbara*, 1–10.

Matsushima, S., Martin, F. D. E., Kawase, H., & Francisco, J. (2014). The Effect of the Basin Edge To the Directional Dependent Horizontal To Vertical Spectral Ratios of Microtremors. *Proc. of the 2nd European Conference on Earthquake Engineering and Siesmology, Istanbul*.

McCulloh, T. H. (1960). Gravity variations and the geology of the Los Angeles basin in California. *US Geological Survey Professional Paper*, *400-B*, 320–325.

McMurdie, D. (1973). Geology and general history of the Dominguez oil field in an urban environment-Los Angeles County, California. *Metropolitan oil fields and their environmental impact: American Association of Petroleum Geologist Trip*, *1*, 25–31.

Mihalic, S., Maja, O., & Krkac, M. (2011). Seismic microzonation: A review of principles and practice. *Geofizika*, *28*(1), 5–20.

Moody, J. D., & Hill, M. J. (1956). Wrench-fault tectonics. *Bulletin of the Geological Society of America*, *67*(9), 1207–1246. doi: 10.1130/0016-7606(1956)67[1207:WT]2.0.CO;2

Mucciarelli, M., Gallipoli, M. R., & Arcieri, M. (2003). The stability of the horizontal-to-vertical spectral ratio of triggered noise and earthquake recordings. *Bulletin of the Seismological Society of America*, *93*(3), 1407–1413. doi: 10.1785/0120020213

Nakamura, Y. (1989). A method for dynamic characteristics estimation of subsurface using microtremor on the ground surface. *Railway Technical Research Institute, Quarterly Reports*, *30*(1).

Nakamura, Y. (2000). Clear identification of fundamental idea of Nakamura's technique and its applications. *Proceedings of the 12th World Conference on Earthquake Engineering*, *2656*.

Nakamura, Y. (2008). On the H/V spectrum. *The 14th World Conference on Earthquake Engineering*, 1–10.

Nicholson, C., Sorlien, C. C., Atwater, T., Crowell, J. C., & Luyendyk, B. P. (1994). Microplate capture, rotation of the western Transverse Ranges, and initiation of the San Andreas transform as a low-angle fault system. *Geology*, *22*(6), 491–495.

Nilsen, T. H. (1987). Paleogene tectonics and sedimentation of coastal California. *Cenozoic basin development of coastal California*, *6*, 81–123.

Nogoshi, M., & Igarashi, T. (1971). On the amplitude characteristics of microtremor (part 2). *Journal of Seismological Society Japan (ZISIN)*, *24*, 26–40.

Olsen, K. B. (2000). Site amplification in the Los Angeles basin from three-dimensional modeling of ground motion. *Bulletin of the Seismological Society of America*, *90*(6B), 6–77. doi: 10.1785/0120000506

Olsen, K. B., Day, S. M., Dalguer, L. A., Mayhew, J., Cui, Y., Zhu, J., ... Chourasia, A. (2009). ShakeOut-D: Ground motion estimates using an ensemble of large earthquakes on the southern San Andreas fault with spontaneous rupture propagation. *Geophysical Research Letters*, *36*(4), 2–7. doi: 10.1029/2008GL036832

Özalaybey, S., Zor, E., Ergintav, S., & Tapirdamaz, M. C. (2011). Investigation of 3-D basin structures in the zmit Bay area (Turkey) by single-station microtremor and gravimetric methods. *Geophysical Journal International*, *186*(2), 883–894. doi: 10.1111/j.1365-246X.2011.05085.x

Panou, A. A., Theodulidis, N., Hatzidimitriou, P., Stylianidis, K., & Papazachos, C. B. (2005). Ambient noise horizontal to vertical spectral ratio in site effects estimation and correlation with seismic damage distribution in urban environment: The case of the city of Thessaloniki (Northern Greece). *Soil Dynamics and Earthquake Engineering*, *25*(4), 261–274. doi: 10.1016/j.soildyn.2005.02.004

Parolai, S., Bormann, P., & Milkereit, C. (2002). New relationships between Vs, thickness of sediments, and resonance frequency calculated by the H/V ratio of seismic noise for the cologne area (Germany). *Bulletin of the Seismological Society of America*, *92*(6), 2521–2527. doi: 10.1785/0120010248

Parolai, S., Richwalski, S. M., Milkereit, C., & Bormann, P. (2004). Assessment of the stability of H/V spectral ratios from ambient noise and comparison with earthquake data in the Cologne area (Germany). *Tectonophysics*, *390*(1), 57–73. doi: 10.1016/j.tecto.2004.03.024

Plesch, A., Suess, M., Munster, J., Shaw, J., Hauksson, E., Tanimoto, T., ... Others, U. W. G. (2007). A new velocity model for southern California: CVM-H 5.0. *2007 Southern California Earthquake Center Annual Meeting, Proceedings and Abstracts*, *17*, 159.

Plesch, A., Tape, C., Shaw, J., & USR Working Group and others. (2009). CVM-H 6.0: Inversion integration, the San Joaquin Valley and other advances in the community velocity model. *2009 Southern California Earthquake Center Annual Meeting, Proceedings and Abstracts*, *19*, 260–261.

Popenoe, W. P., Imlay, R. W., & Murphy, M. A. (1960). Correlation of the Cretaceous formations of the Pacific coast (United States and northwestern Mexico). *Geological Society of America Bulletin*, *71*(10), 1491–1540.

Rial, J. A. (1996). The anomalous seismic response of the ground at the Tarzana Hill site during the Northridge 1994 Southern California earthquake: A resonant, sliding block? *Bulletin of the Seismological Society of America*, *86*(6), 1714–1723.

Rial, J. a., Saltzman, N. G., & Ling, H. (1992). Earthquake-induced resonance in sedimentary basins. *American Scientist*, *80*(6), 566–578.

Rogers, A. M., Tinsley, J. C., & Borcherdt, R. D. (1985). Predicting relative ground response. *US Geological Survey Professional Paper*, *1360*, 221–248.

Rogers, A. M., Tinsley, J. C., Hays, W. W., & King, K. W. (1979). Evaluation of the relation between near-surface geological units and ground response in the vicinity of Long Beach, California. *Bulletin of the Seismological Society of America*, *69*(5), 1603–1622.

Sánchez-Sesma, F. J., Rodríguez, M., Iturrarán-Viveros, U., Luzón, F., Campillo, M., Margerin, L., ... Rodríguez-Castellanos, A. (2011). A theory for microtremor H/V spectral ratio: Application for a layered medium. *Geophysical Journal International*, *186*(1), 221–225. doi: 10.1111/j.1365-246X.2011.05064.x

Satoh, T., Kawase, H., & Matsushima, S. (2001). Differences between site characteristics obtained from microtremors, S-waves, P-waves, and codas. *Bulletin of the Seismological Society of America*, *91*(2), 313–334. doi: 10.1785/0119990149

Seht, M. I. V., & Wohlenberg, J. (1999). Microtremor Measurements Used to Map Thickness of Soft Sediments. *Bulletin of the Seismological Society of America*, *89*(1), 250–259.

Seo, K. (1997). Comparison of measured microtremor with damage distribution. *JICA Research and Development Project on Earthquake Disaster Prevention, 306-320*, 306–320.

SESAME WP12. (2004). Guidelines for the implementation of the H/V spectral ratio technique on ambient vibrations. Measurements, processing and interpretation. SESAME European research project. *European Commission. Research General Directorate Project No. EVG1-CT-2000-00026 SESAME*, *D23.12*.

Siddiqqi, J., & Atkinson, G. M. (2002). Ground-motion amplification at rock sites across Canada as determined from the horizontal to vertical component ratio. *Bulletin of the Seismological Society of America*, *92*(2), 877–884. doi: 10.1785/0120010155

Spudich, P., Hellweg, M., & Lee, W. H. K. (1996). Directional topographic site response at Tarzana observed in aftershocks of the 1994 Northridge, California, earthquake: implications for mainshock motions. *Bulletin of the Seismological Society of America*, *86*(1B), 193–208.

TC4-ISSMGE. (1999). Manual for Zonation on Seismic Geotechnical Hazard (Revised edition). *Japanese Geotechnical Society*, 1–210.

Thelen, W. A., Clark, M., Lopez, C. T., Loughner, C., Park, H., Scott, J. B., ... Louie, J. N. (2006). A transect of 200 shallow shear-velocity profiles across the Los Angeles Basin. *Bulletin of the Seismological Society of America*, *96*(3), 1055–1067. doi: 10.1785/0120040093

Theodulidis, N., Culterera, G., Tento, A., Faeh, D., Atakan, K., Bard, P.-Y., ... Haghshenas, E. (2004). Empirical evaluation of the horizontal-to-vertical spectral ratio technique: results from the SESAME project. *13th World Conference on Earthquake Engineering*.

Uebayashi, H., Kawabe, H., Kamae, K., & Horike, M. (2008). Behavior of Microtremor H / V Spectrum and Phase Velocity on the Basin Peripheral and Inversion for Determining Basin Structure. *The 14th World Conference on Earthquake Engineering*, 2–37.

Wald, D. J., & Graves, R. W. (1998). The Seismic Response of the Los Angeles Basin , California. *Bulletin of the Seismological Society of America*, *88*(2), 337–356.

Wathelet, M. (2005). GEOPSY Geophysical Signal Database for Noise Array Processing. *Software, LGIT, Grenoble, Fr*.

Wathelet, M. (2011). Geopsy project. *Software, LGIT, Grenoble, Fr*.

Welch, P. D. (1967). The use of fast Fourier transform for the estimation of power spectra: A method based on time averaging over short, modified periodograms. *IEEE Transactions on audio and electroacoustics*, *15*(2), 70–73.

Wessel, P., Smith, W. H., Scharroo, R., Luis, J., & Wobbe, F. (2013). Generic mapping tools: Improved version released. *Eos, Transactions American Geophysical Union*, *94*(45), 409–410.

Wills, C., Petersen, M., Bryant, W., Reichle, M., Saucedo, G., Tan, S., ... Treiman, J. (2000). A site-conditions map for California based on geology and shear-wave velocity. *Bulletin of the Seismological Society of America*, *90*(6B), S187–S208.

Wissler, S. G. (1943). Stratigraphic formations of the producing zones of the Los Angeles Basin oil fields. *Geologic formations and economic development of the oil and gas fields of California: California Department of Natural Resources, Division of Mines Bulletin*, *118*, 209–234.

Woodford, A. (1960). Bedrock patterns and strike-slip faulting in southwestern California. *American Journal of Science*, *258*, 400–417.

Woodring, W. P., Bramlette, M. N., & Kew, W. S. W. (1946). Geology and paleontology of Palos Verdes Hills, California. *Professional Paper. US Government Printing Office*, *207*.

Woodring, W. P., & Popenoe, W. (1945). Paleocene and Eocene stratigraphy of the northwestern Santa Ana Mountains, Orange County, California. *US Geological Survey Oil and Gas Investigation : Preliminary*, *Chart 12*(1).

Wright, T. L. (1991). Structural Geology and Tectonic Evolution of the Los Angeles Basin, California. *Active Margin Basins*, *52*, 35–134.

Yeats, R. S. (1968). Southern California structure, sea-floor spreading, and history of the Pacific Basin. *Geological Society of America Bulletin*, *79*(12), 1693–1702.

Yerkes, R., McCulloh, T., Schoellhamer, J., & Vedder, J. (1965). Geology of the Los Angeles Basin - Introduction. *Geological Survey Professional Papers.(US);(United States)*, *420-A*.

Yomogida, K., & Etgen, J. T. (1993). 3-D wave propagation in the Los Angeles Basin for the Whittier- Narrows earthquake. *Bulletin of the Seismological Society of America*, *83*(5), 1325–1344.

Zhao, B., Horike, M., & Yoshihiro, T. (2000). Analytical study on reliability of seismic site-specific characteristics estimated from microtremor measurements. *Proceeding of the 12th World Conference on Earthquake Engineering*, 1522–1530.

Ziony, J. I., Wentworth, C. M., Buchanan-Banks, J. M., & Wagner, H. C. (1974). Preliminary map showing recency of faulting in coastal southern California. *Department of the Interior United State Geological Survey*, *MF-585*.

Appendix A

All About LASSIE

A.1 LASSIE

The Los Angeles Syncline Seismic Interferometry Experiment (LASSIE) is a collaborative experiment that involves a high density linear array of broadband seismometers across the Los Angeles Basin. The collaborative efforts of LASSIE are from academia (USGS, Caltech, UCLA, and Cal Poly Pomona) and industry (NodalSeismic, Signal Hill Petroleum, and Occidental Petroleum). 73 broadband seismometers were installed and had data collected continuously for a month. The details of the seismometers are listed in table A.1.

Equipment

The seismometer stations installed by Cal Poly Pomona, shown by figure A.1, used Guralp seismometers, CMG-6TD, a three axis seismometer that measures north/south, east/west, and vertical components. The seismometer is capable of recording a frequency

Figure A.1: *Guralp Seismometer CMG-6TD shown with cables and GPS unit.*

range of 0.333 - 50 Hz as long as the base of the seismometer is within 3 degrees of level.

A.1.1 Installation

Installation of the Guralp Seismometer CMG-6TD at LASSIE locations A137 - A144 by Cal Poly Pomona, an effort led by the author and Mikey Herrman, required (at each site) two 200 liter holes, shown in figure A.2, to be dug for proper subterranean installation of the seismometer, wires, and battery. Obstacles to overcome were leveling of the seismometer, potential water damage to the equipment, temperature fluctuations, and potential ground disturbance caused by human and wildlife influences. A porous concrete

Figure A.2: *At LASSIE site A144, Terry C. and Dandan Z. use pick axes to dig installation holes for the battery and seismometer in very warm weather.*

leveling stone is used with well sorted medium sand to provide a level base and adequate drainage from water for the seismometer. Although the CMG-6TD is a waterproof unit, the instrument and a 12 volt marine battery are both secured and sealed within large plastic bags to protect against dust and water damage. A subterranean installation protects the instrument from daily temperature variability which causes thermal expansion and contraction of the high precision and sensitive components within the CMG-6TD unit itself. The excavated depth of 0.6 m - 0.7 m allowed for the surrounding soil to insulate the unit from the radical changes in ground and air temperatures. A split wire conduit was used to

help protect the cables from possible wildlife and human caused damage. Chicken wire was buried approximately 3 cm below the surface to prevent accidental excavation of the unit. Cross section of the installation is shown in figure A.3. The shallow trench allowed easy access of seismometer data and computer cables without disturbing the seismometer during maintenance visits. At the end of the installation, the GPS unit is the only exposed part of the equipment. This is visually appealing to both the environment and the property owners.

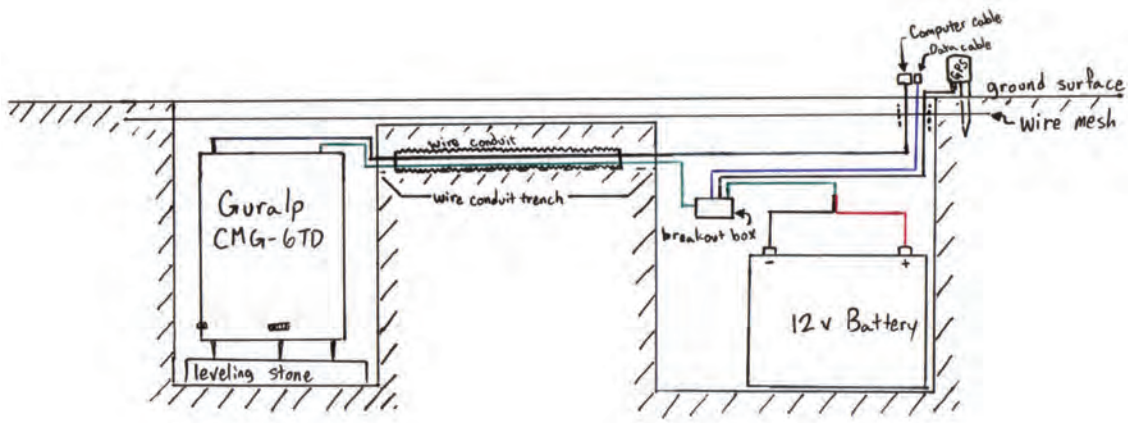

Figure A.3: *Simplified cartoon of the installation of a Guralp Seismometer CMG-6TD with cables and GPS unit.*

A.1.2 Installation challenges

Temperatures in the summer of 2014 reached record high with ground temperatures in the triple digits. We installed the broadband seismomters in a two week time window of early to mid September. The first week was spent visiting, surveying, and gaining permission to install the instruments at potential installation sites. This process involved

looking at a regional map of the proposed installation sites by the lead project designers of LASSIE. Using this map we scouted potential sites within a 100 m radius of the originally proposed site. We personally spoke with the property owners to acquire access to install the broadband Guralp CMG 6TD on the property. We were careful to explain our project goals to avoid inciting panic and fear into our volunteers by avoiding key words such as earthquake, hazard, risk, industry, etc. We made sure to use language that is comforting and nonthreatening such as explaining our status as college students and how we are using this opportunity to investigate the ambient field.

The second week of the two week time window was spent physically installing the seismometers. The author of this thesis was the primary project manager and Michael Herrman secondary lead project manager of this process; in charge of coordinating a reasonable time to arrive at the property with an installation team and equipment, delegation of task and responsibilities to team members, and overseeing the successful installation of the 8 broadband seismometers.

The record high temperatures posed a problem for practical reasons such as heat stroke, sunburns, and dehydration. The high temperatures and lack of recent precipitation also meant that the soils were stiff from drying. We also lacked the proper tools for installation. However, we were fortunate that the property owners at site A138 was kind enough to lend us his pick axe to help us dig through the hard baked clay soils.

A.2 LASSIE instruments

Los Angeles Syncline Interferometry Experiment consist of 73 broadband seismometers Table A.1.

Table A.1: *The type of seismometer at each LASSIE location.*

Name	Latitude	Longitude	Institution	Instrument	Corner Period
A122	33.892	-118.1005	CIT	Trillium Compact + Taurus	20 s
A123	33.8991	-118.0945	CIT	Trillium Compact + Taurus	20 s
A124	33.9066	-118.0889	CIT	Trillium Compact + Taurus	20 s
A125	33.9124	-118.0847	CIT	Trillium Compact + Taurus	20 s
A126	33.9214	-118.0785	CIT	Trillium Compact + RefTek	20 s
A127	33.9285	-118.0732	USGS	Trillium Compact + RefTek	20 s
A128	33.9365	-118.0645	USGS	Trillium Compact + RefTek	20 s
A129	33.9465	-118.0599	USGS	Trillium Compact + RefTek	20 s
A130	33.9498	-118.0516	USGS	Trillium Compact + RefTek	20 s
A131	33.9595	-118.0482	USGS	Trillium Compact + RefTek	20 s
A132	33.9649	-118.0417	UCLA	Guralp 3T + Quanterra 330	30 s
A133	33.9727	-118.0365	UCLA	Guralp 3T + Quanterra 330	30 s
A134	33.9807	-118.0289	UCLA	Guralp 3T + Quanterra 330	30 s
A135	33.9871	-118.0216	UCLA	Guralp 3T + Quanterra 330	30 s
A136	34.0048	-118.0375	UCLA	Guralp 3T + Quanterra 330	30 s
A137	34.0025	-118.0085	CPP	Guralp 6T	30 s
A138	34.0074	-117.9988	CPP	Guralp 6T	30 s
A139	34.0155	-117.9946	CPP	Guralp 6T	30 s
A140	34.0236	-117.9896	CPP	Guralp 6T	30 s

Continued on the next page

Table A.1 – *Continued from previous page*

Name	Latitude	Longitude	Institution	Instrument	Corner Period
A141	34.0335	-117.9882	CPP	Guralp 6T	30 s
A142	34.0389	-117.9825	CPP	Guralp 6T	30 s
A143	34.0476	-117.9773	CPP	Guralp 6T	30 s
A144	34.0556	-117.9722	CPP	Guralp 6T	30 s
B501	33.7663	-118.2043	Industry	Guralp 3T + Quanterra 330	30 s
B502	33.7638	-118.1684	Industry	Guralp 3T + Quanterra 330	30 s
B503	33.7777	-118.1669	Industry	Guralp 3T + Quanterra 330	30 s
B504	33.7788	-118.1533	Industry	Guralp 3T + Quanterra 330	30 s
B505	33.7605	-118.145	Industry	Guralp 3T + Quanterra 330	30 s
B506	33.753	-118.1028	Industry	Guralp 3T + Quanterra 330	30 s
B507	33.7591	-118.1798	Industry	Guralp 3T + Quanterra 330	30 s
B508	33.7525	-118.1613	Industry	Guralp 3T + Quanterra 330	30 s
B509	33.7398	-118.1405	Industry	Guralp 3T + Quanterra 330	30 s
B510	33.7423	-118.1612	Industry	Guralp 3T + Quanterra 330	30 s
N101	33.7772	-118.2012	Industry	Guralp 3T + Quanterra 330	30 s
N102	33.7798	-118.1969	Industry	Guralp 3T + Quanterra 330	30 s
N103	33.7892	-118.1851	Industry	Guralp 3T + Quanterra 330	30 s
N104	33.7906	-118.1828	Industry	Guralp 3T + Quanterra 330	30 s
N105	33.795	-118.178	Industry	Guralp 3T + Quanterra 330	30 s
N106	33.7994	-118.1682	Industry	Guralp 3T + Quanterra 330	30 s
N107	33.8025	-118.1701	Industry	Guralp 3T + Quanterra 330	30 s
N108	33.8055	-118.1709	Industry	Guralp 3T + Quanterra 330	30 s
N109	33.8067	-118.1645	Industry	Guralp 3T + Quanterra 330	30 s

Continued on the next page

Table A.1 – *Continued from previous page*

Name	Latitude	Longitude	Institution	Instrument	Corner Period
N110	33.8147	-118.158	Industry	Guralp 3T + Quanterra 330	30 s
N111	33.8158	-118.1553	Industry	Guralp 3T + Quanterra 330	30 s
N112	33.8183	-118.1505	Industry	Guralp 3T + Quanterra 330	30 s
N113	33.8222	-118.1471	Industry	Guralp 3T + Quanterra 330	30 s
N114	33.8234	-118.1426	Industry	Guralp 3T + Quanterra 330	30 s
N115	33.8299	-118.1323	Industry	Guralp 3T + Quanterra 330	30 s
N116	33.8461	-118.1347	Industry	Guralp 3T + Quanterra 330	30 s
N117	33.8534	-118.1301	Industry	Guralp 3T + Quanterra 330	30 s
N118	33.8645	-118.1245	Industry	Guralp 3T + Quanterra 330	30 s
N119	33.8658	-118.1184	Industry	Guralp 3T + Quanterra 330	30 s
N120	33.8762	-118.111	Industry	Guralp 3T + Quanterra 330	30 s
N121	33.8879	-118.1156	Industry	Guralp 3T + Quanterra 330	30 s
N201	33.7672	-118.1795	Industry	Guralp 3T + Quanterra 330	30 s
N202	33.7882	-118.1705	Industry	Guralp 3T + Quanterra 330	30 s
N203	33.7971	-118.165	Industry	Guralp 3T + Quanterra 330	30 s
N204	33.8018	-118.1591	Industry	Guralp 3T + Quanterra 330	30 s
N205	33.8107	-118.1463	Industry	Guralp 3T + Quanterra 330	30 s
N206	33.8138	-118.1416	Industry	Guralp 3T + Quanterra 330	30 s
N207	33.7781	-118.1556	Industry	Guralp 3T + Quanterra 330	30 s
N208	33.7862	-118.1452	Industry	Guralp 3T + Quanterra 330	30 s
N209	33.778	-118.1266	Industry	Guralp 3T + Quanterra 330	30 s
N301	33.7958	-118.1926	Industry	Guralp 3T + Quanterra 330	30 s
N302	33.8011	-118.1856	Industry	Guralp 3T + Quanterra 330	30 s

Continued on the next page

Table A.1 – *Continued from previous page*

Name	Latitude	Longitude	Institution	Instrument	Corner Period
N303	33.8088	-118.18	Industry	Guralp 3T + Quanterra 330	30 s
N304	33.818	-118.1726	Industry	Guralp 3T + Quanterra 330	30 s
N305	33.8219	-118.1605	Industry	Guralp 3T + Quanterra 330	30 s
N306	33.8242	-118.1552	Industry	Guralp 3T + Quanterra 330	30 s
N307	33.777	-118.1862	Industry	Guralp 3T + Quanterra 330	30 s
N308	33.8032	-118.1932	Industry	Guralp 3T + Quanterra 330	30 s
N309	33.8286	-118.1976	Industry	Guralp 3T + Quanterra 330	30 s
N310	33.8384	-118.2126	Industry	Guralp 3T + Quanterra 330	30 s

Appendix B

HVSR data tables

B.1 Geopsy default settings

Geopsy default settings are shown in table B.1. These default values have been tested by Ho & Polet (2015).

Table B.1: *Geopsy default settings for this thesis*

STA	LTA	Min STA/LTA	Max STA/LTA
1	30	0.2	2.5

B.2 LASSIE spectral ratio measurements

Spectral ratio parameters are listed in tables B.2 - B.6.

Table B.2: *Parameters for the peaks determined from the spectral ratio graphs for* $0.003Hz \leq f_0 \leq 0.084Hz$. *The name of each station, latitude, longitude, peak frequency, peak frequency error, amplitude, standard deviation of the amplitude of the peak, and how many SESAME reliable curve / clear peak criteria failed.*

Station	**Latitude**	**Longitude**	f_0	$\pm f_0$	A_0	σ_A	**Curve / Peak**
A124	33.907	-118.089	0.080	0.004	3.030	1.400	0/1
A128	33.937	-118.065	0.079	0.005	3.300	1.390	0/1
A129	33.947	-118.060	0.081	0.003	4.193	1.667	0/1
A135	33.987	-118.022	0.082	0.004	2.458	1.432	0/1,2
B501	33.7663	-118.2043	0.082	0.007	7.820	1.571	0/1
B502	33.7638	-118.1684	0.080	0.005	6.000	1.452	0/1
B510	33.7423	-118.1612	0.062	0.007	6.100	1.205	0/1
N202	33.7882	-118.1705	0.083	0.007	3.680	1.333	0/1
N203	33.7971	-118.165	0.079	0.004	3.650	1.704	0/1
N207	33.7781	-118.1556	0.084	0.006	6.670	1.527	0/1
N208	33.7862	-118.1452	0.082	0.006	4.120	1.398	0/1
N304	33.818	-118.1726	0.081	0.008	3.240	1.407	0/1

Table B.3: *Results of LASSIE spectral graph generation for* $0.085Hz \leq f_0 \leq 0.159Hz$. *The table description is the same as table B.2.*

Station	**Latitude**	**Longitude**	f_0	$\pm f_0$	A_0	σ_A	**Curve / Peak**
N101	33.777	-118.201	0.138	0.012	5.300	1.183	0/1
N102	33.780	-118.197	0.137	0.012	5.070	1.180	0/1
N103	33.789	-118.185	0.134	0.012	4.660	1.193	0/1

Continued on the next page

Table B.3 – *Continued from previous page*

Station	**Latitude**	**Longitude**	f_0	$\pm f_0$	A_0	σ_A	**Curve / Peak**
N105	33.795	-118.178	0.131	0.012	4.220	1.183	0/1
N106	33.799	-118.168	0.131	0.012	2.000	0.611	0/1
N107	33.803	-118.170	0.131	0.013	3.910	1.193	0/1
N108	33.806	-118.171	0.087	0.005	2.700	1.450	0/1
N108	33.806	-118.171	0.133	0.016	3.700	1.261	0/1
N109	33.807	-118.165	0.131	0.015	3.700	1.189	0/1
N110	33.815	-118.158	0.126	0.019	3.630	1.209	0/1
N111	33.816	-118.155	0.127	0.017	3.540	1.210	0/0
N112	33.818	-118.151	0.123	0.021	3.560	1.204	0/1
N113	33.822	-118.147	0.120	0.018	3.480	1.175	0/1
N114	33.823	-118.143	0.120	0.013	3.690	1.261	0/1
N115	33.830	-118.132	0.122	0.013	3.470	1.332	0/1
N116	33.846	-118.135	0.085	0.006	4.100	1.270	0/1
N117	33.853	-118.130	0.120	0.010	3.880	1.359	0/1
N118	33.865	-118.125	0.115	0.013	3.700	1.219	0/1
N119	33.866	-118.118	0.110	0.014	3.780	1.205	0/1
N120	33.876	-118.111	0.111	0.016	3.969	1.235	0/1
N121	33.888	-118.116	0.114	0.014	3.530	1.225	0/1
A122	33.892	-118.101	0.126	0.018	3.170	1.512	0/1
A124	33.907	-118.089	0.107	0.013	3.314	1.329	0/1
A126	33.921	-118.079	0.106	0.012	3.520	1.237	0/1
A127	33.929	-118.073	0.108	0.014	3.074	1.241	0/1,4
A128	33.937	-118.065	0.124	0.012	2.730	1.286	0/1

Continued on the next page

Table B.3 – *Continued from previous page*

Station	**Latitude**	**Longitude**	f_0	$\pm f_0$	A_0	σ_A	**Curve / Peak**
A130	33.950	-118.052	0.109	0.010	2.610	1.264	0/1
A132	33.965	-118.042	0.111	0.017	2.190	1.237	0/3
A133	33.973	-118.037	0.116	0.009	2.030	1.216	0/1,2
A134	33.981	-118.029	0.116	0.008	1.708	1.222	0/1,2,3
A137	34.003	-118.009	0.122	0.012	1.886	1.201	0/1,3,4
A138	34.007	-117.999	0.122	0.010	2.058	1.212	0/1,2
A139	34.016	-117.995	0.126	0.010	2.074	1.192	0/1,2
A140	34.024	-117.990	0.125	0.011	2.140	1.206	0/1,2
A141	34.034	-117.988	0.136	0.016	2.350	1.195	0/2
A142	34.039	-117.983	0.144	0.028	2.250	1.200	0/1,2
A144	34.056	-117.972	0.150	0.014	2.447	1.180	0/1,2
B501	33.7663	-118.2043	0.141	0.011	5.800	1.980	0/1
B502	33.7638	-118.1684	0.134	0.013	4.960	1.220	0/1
B504	33.7788	-118.1533	0.132	0.019	4.070	1.330	0/1
B506	33.753	-118.1028	0.130	0.014	4.580	1.200	0/1
B508	33.7525	-118.1613	0.098	0.014	9.450	1.280	0/1
B509	33.7398	-118.1405	0.160	0.021	2.920	1.523	0/1
B510	33.7423	-118.1612	0.145	0.007	3.620	1.558	0/1
N201	33.7672	-118.1795	0.132	0.013	4.610	1.228	0/1
N202	33.7882	-118.1705	0.132	0.013	4.340	1.194	0/1
N203	33.7971	-118.165	0.132	0.013	3.770	1.188	0/0
N204	33.8018	-118.1591	0.131	0.014	3.850	1.132	0/1
N205	33.8107	-118.1463	0.123	0.015	3.750	1.212	0/1

Continued on the next page

Table B.3 – *Continued from previous page*

Station	**Latitude**	**Longitude**	f_0	$\pm f_0$	A_0	σ_A	**Curve / Peak**
N206	33.8138	-118.1416	0.116	0.020	3.880	1.220	0/0
N207	33.7781	-118.1556	0.126	0.014	4.090	1.220	0/1
N208	33.7862	-118.1452	0.129	0.013	4.050	1.195	0/1
N209	33.778	-118.1266	0.139	0.019	4.270	1.366	0/1
N301	33.7958	-118.1926	0.130	0.012	4.740	1.204	0/1
N303	33.8088	-118.18	0.132	0.014	3.990	1.206	0/0
N304	33.818	-118.1726	0.136	0.016	3.620	1.132	0/1
N305	33.8219	-118.1605	0.116	0.021	3.850	1.202	0/1
N306	33.8242	-118.1552	0.115	0.023	3.740	1.222	0/1
N307	33.777	-118.1862	0.128	0.011	3.980	1.193	0/1
N308	33.8032	-118.1932	0.131	0.013	3.840	1.224	0/1
N309	33.8286	-118.1976	0.140	0.013	3.820	1.165	0/1
N310	33.8384	-118.2126	0.133	0.013	4.100	1.203	0/1
N310	33.8384	-118.2126	0.085	0.008	5.520	1.901	0/1

Table B.4: *Results of SCSN spectral graph generation for* $0.085Hz \leq f_0 \leq 0.159Hz$*. The table description is the same as table B.2.*

Station	**Latitude**	**Longitude**	f_0	$\pm f_0$	A_0	σ_A	**Curve / Peak**
STS	33.79033	-118.19878	0.136	0.015	4.830	1.261	0/1
LTP	33.8811	-118.17568	0.117	0.019	3.360	1.238	0/1
DLA	33.84822	-118.09624	0.107	0.021	3.650	1.237	0/1
USC	34.01919	-118.28631	0.155	0.013	3.880	1.121	0/1
LGB	33.9753	-118.14918	0.110	0.019	2.840	1.241	0/1

Table B.5: *Results of LASSIE & SCSN spectral graph generation for* $0.16Hz \leq f_0 \leq 1.0Hz$. *The table description is the same as table B.2.*

Station	**Latitude**	**Longitude**	f_0	$\pm f_0$	A_0	σ_A	**Curve / Peak**
N103	33.789	-118.185	0.535	0.044	2.210	1.604	0/1
A126	33.921	-118.079	0.169	0.011	2.470	1.174	0/1
A127	33.929	-118.073	0.175	0.069	2.230	1.181	0/1
A128	33.937	-118.065	0.178	0.010	2.170	1.235	0/1
A137	34.003	-118.009	0.238	0.018	2.220	1.151	0/1
WLT	34.00948	-117.95077	0.891	0.109	2.480	1.128	0/1
A141	34.034	-117.988	0.256	0.010	2.430	1.184	0/2
A140	34.024	-117.990	0.993	0.099	2.140	1.104	0/1
A140	34.024	-117.990	0.197	0.011	2.277	1.173	0/1,2
A129	33.947	-118.060	0.244	0.019	1.793	1.137	0/1,2,3
A133	33.973	-118.037	0.257	0.021	1.695	1.134	0/1,2,3
A143	34.048	-117.977	0.278	0.027	1.971	1.194	0/1,2,3
A144	34.056	-117.972	0.974	0.107	1.770	1.128	0/1,2,3
B508	33.7525	-118.1613	0.515	0.054	2.070	1.602	0/1
B509	33.7398	-118.1405	0.295	0.023	2.490	1.528	0/1

Table B.6: *Results of LASSIE & SCSN spectral graph generation for* $1.0Hz \leq f_0$. *The table description is the same as table B.2.*

Station	**Latitude**	**Longitude**	f_0	$\pm f_0$	A_0	σ_A	**Curve / Peak**
STS	33.79033	-118.19878	1.480	0.228	2.160	1.091	0/1
LTP	33.8811	-118.17568	1.020	0.089	2.100	1.119	0/1

Continued on the next page

Table B.6 – *Continued from previous page*

Station	**Latitude**	**Longitude**	f_0	$\pm f_0$	A_0	σ_A	**Curve / Peak**
A129	33.947	-118.060	1.125	0.159	1.380	1.110	0/1,2,3,5
A130	33.950	-118.052	1.039	0.075	1.585	1.090	0/1,2
A130	33.950	-118.052	20.910	1.246	1.540	1.076	0/1,2,3,5
A131	33.960	-118.048	1.001	0.099	1.622	1.132	0/1,2,3
A131	33.960	-118.048	18.247	0.839	2.239	1.139	0/1,2
A131	33.960	-118.048	34.958	1.295	1.435	1.148	0/1,2,3
A132	33.965	-118.042	1.027	0.105	2.083	1.111	0/1,2,5
A132	33.965	-118.042	4.583	0.252	2.079	1.087	0/1,2,5
A134	33.981	-118.029	1.412	0.101	1.772	1.118	0/1,2,3
A134	33.981	-118.029	19.500	1.358	3.410	1.153	0/2
A135	33.987	-118.022	1.286	0.089	2.065	1.133	0/1,2
A137	34.003	-118.009	5.450	0.204	2.420	1.135	0/1
A137	34.003	-118.009	32.050	2.080	3.061	1.149	0/5
A138	34.007	-117.999	1.719	0.103	1.684	1.086	0/1,3
A138	34.007	-117.999	1.719	0.067	1.565	1.170	0/1,2,3
A139	34.016	-117.995	1.060	0.107	2.910	1.212	0/0
A139	34.016	-117.995	2.361	0.051	1.525	1.066	0/1,2,3
A141	34.034	-117.988	1.015	0.110	2.210	1.150	0/1,2,5
A142	34.039	-117.983	1.060	0.070	2.150	1.104	0/1
A143	34.048	-117.977	1.094	0.113	1.937	1.131	0/1,2,3,5
B506	33.753	-118.1028	2.350	0.193	3.150	1.099	0/0
B508	33.7525	-118.1613	2.630	0.239	2.330	1.101	0/0
B509	33.7398	-118.1405	1.760	0.218	2.190	1.182	0/1

Continued on the next page

Table B.6 – *Continued from previous page*

Station	**Latitude**	**Longitude**	f_0	$\pm f_0$	A_0	σ_A	**Curve / Peak**
B510	33.7423	-118.1612	2.240	0.156	2.230	1.069	0/0
N209	33.778	-118.1266	24.380	0.497	4.630	1.039	0/0
N301	33.7958	-118.1926	5.610	0.218	2.110	1.061	0/1
N310	33.8384	-118.2126	1.100	0.063	2.180	1.114	0/1

Appendix C

HVSR graphs of the LASSIE array

Example spectral ratio graphs are shown in this appendix for each station of the LASSIE array. We present the HVSR graphs of the LA basin transect from stations N101-A144 first, then those of the Long Beach cluster of LASSIE stations.

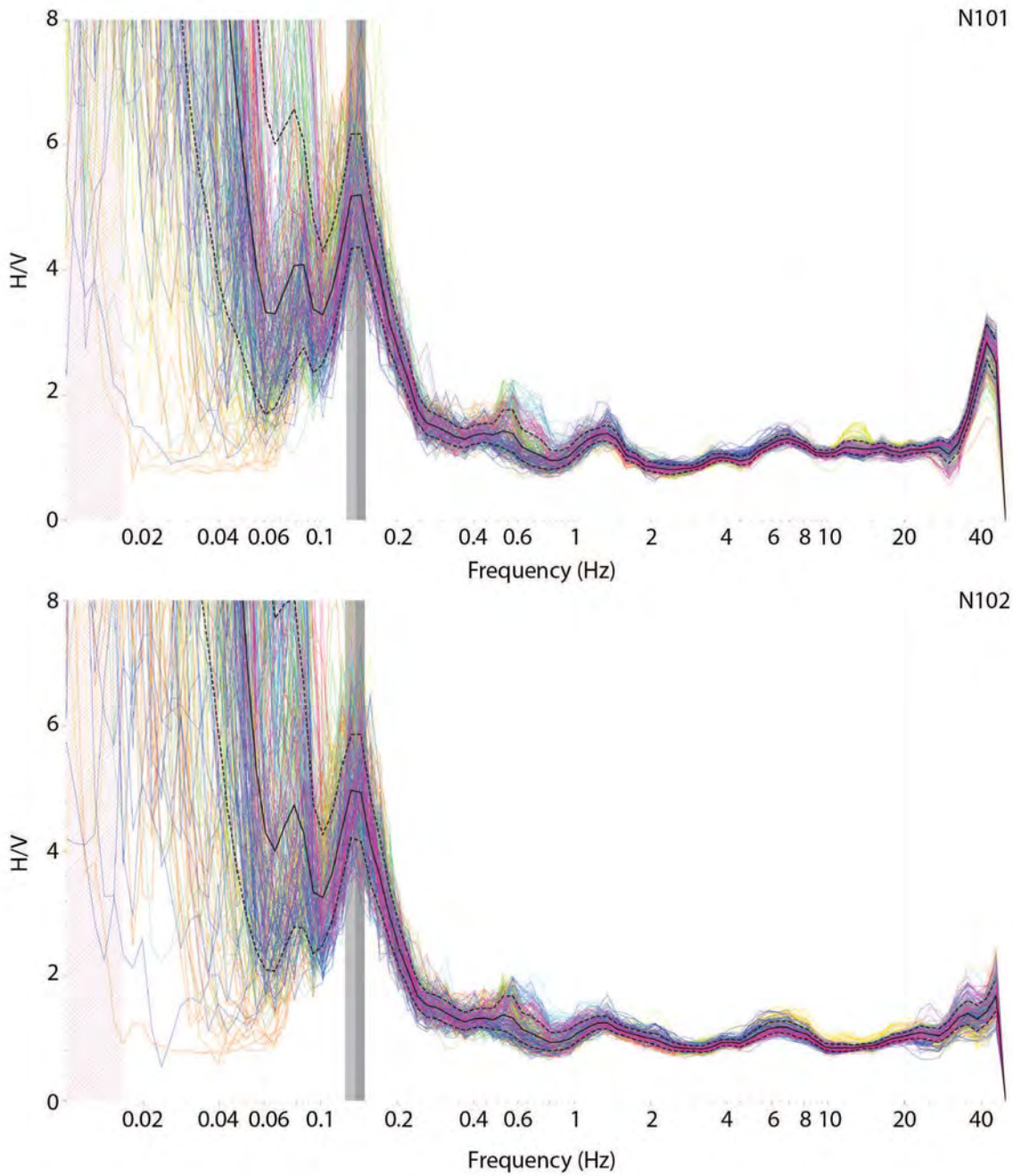

Figure C.1: *Station N101 - N102. Spectral ratio graphs depict the average HVSR curve with a solid line and standard deviation with dashed lines. Solid gray vertical bar shows clear spectral peak frequencies and standard deviation. Individual spectral curves are color coded for specific windows in the total processed waveform duration.*

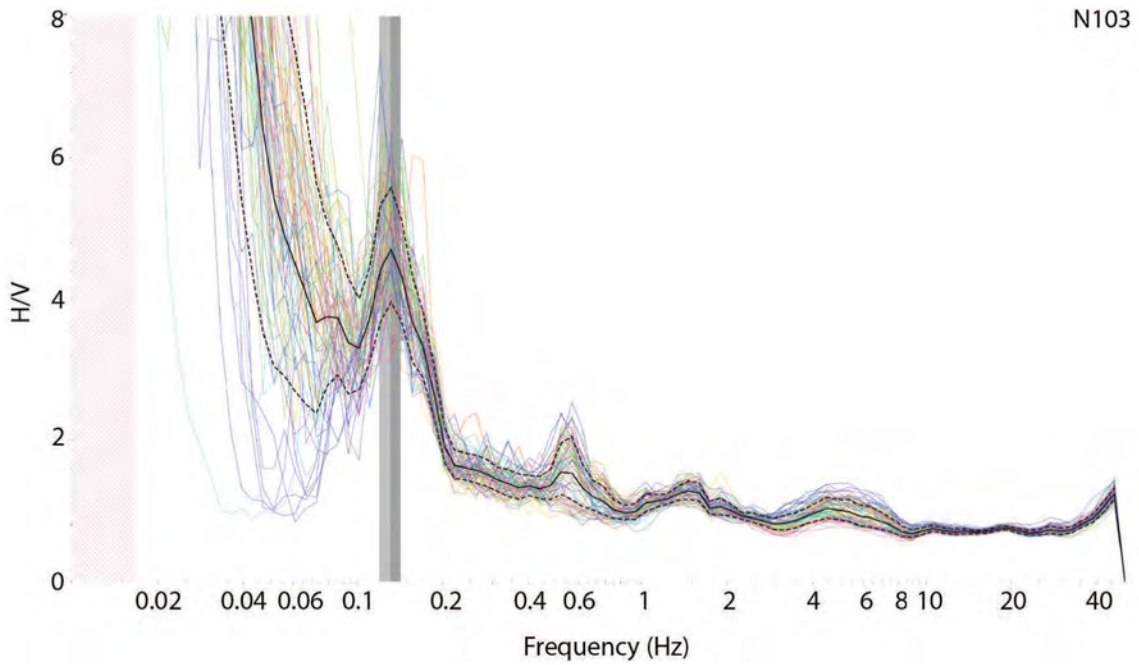

NO DATA AVAILABLE FOR STATION N104

Figure C.2: *Station N103 - N104. Description is the same as figure C.1.*

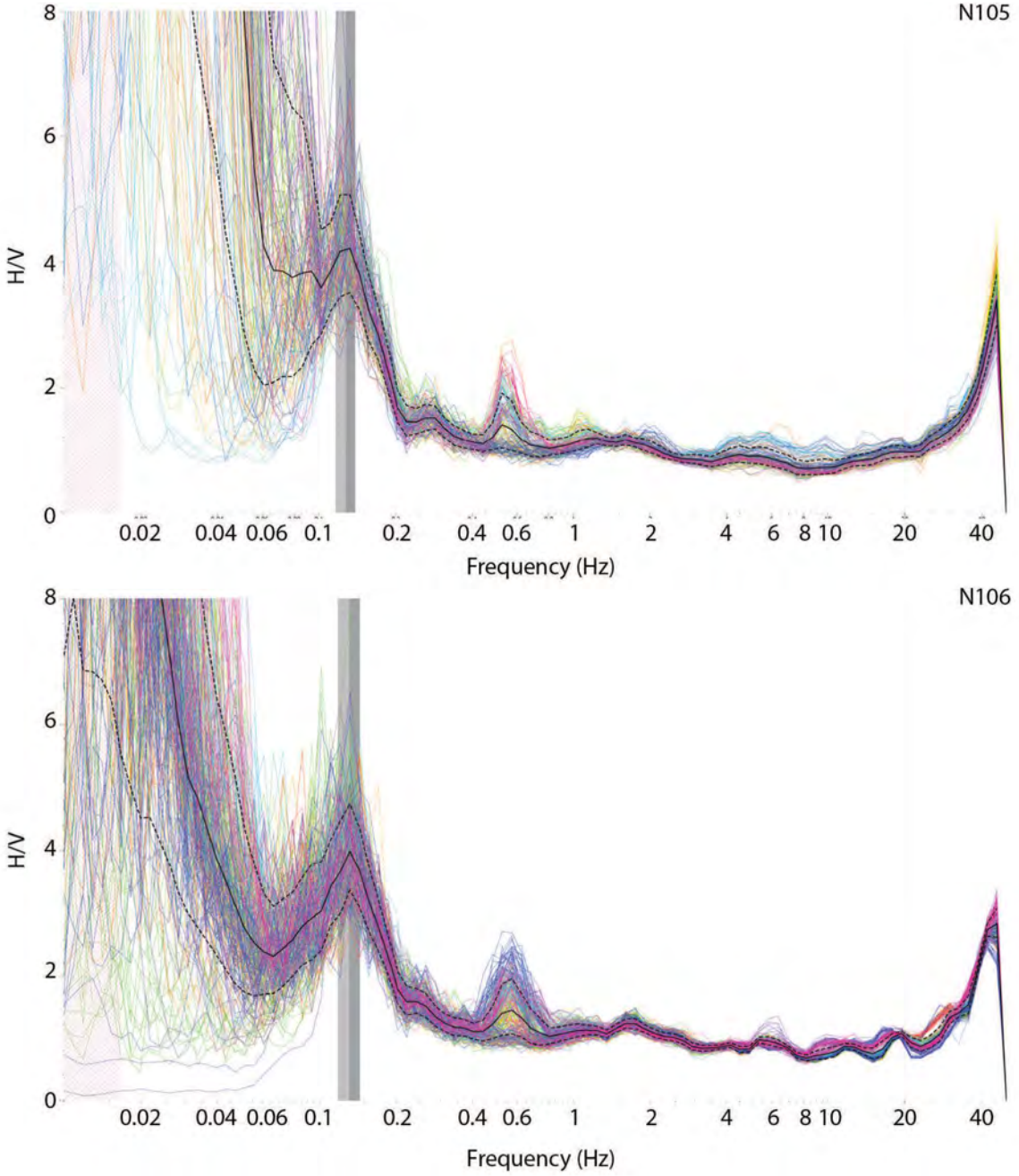

Figure C.3: *Station N105 - N106. Description is the same as figure C.1.*

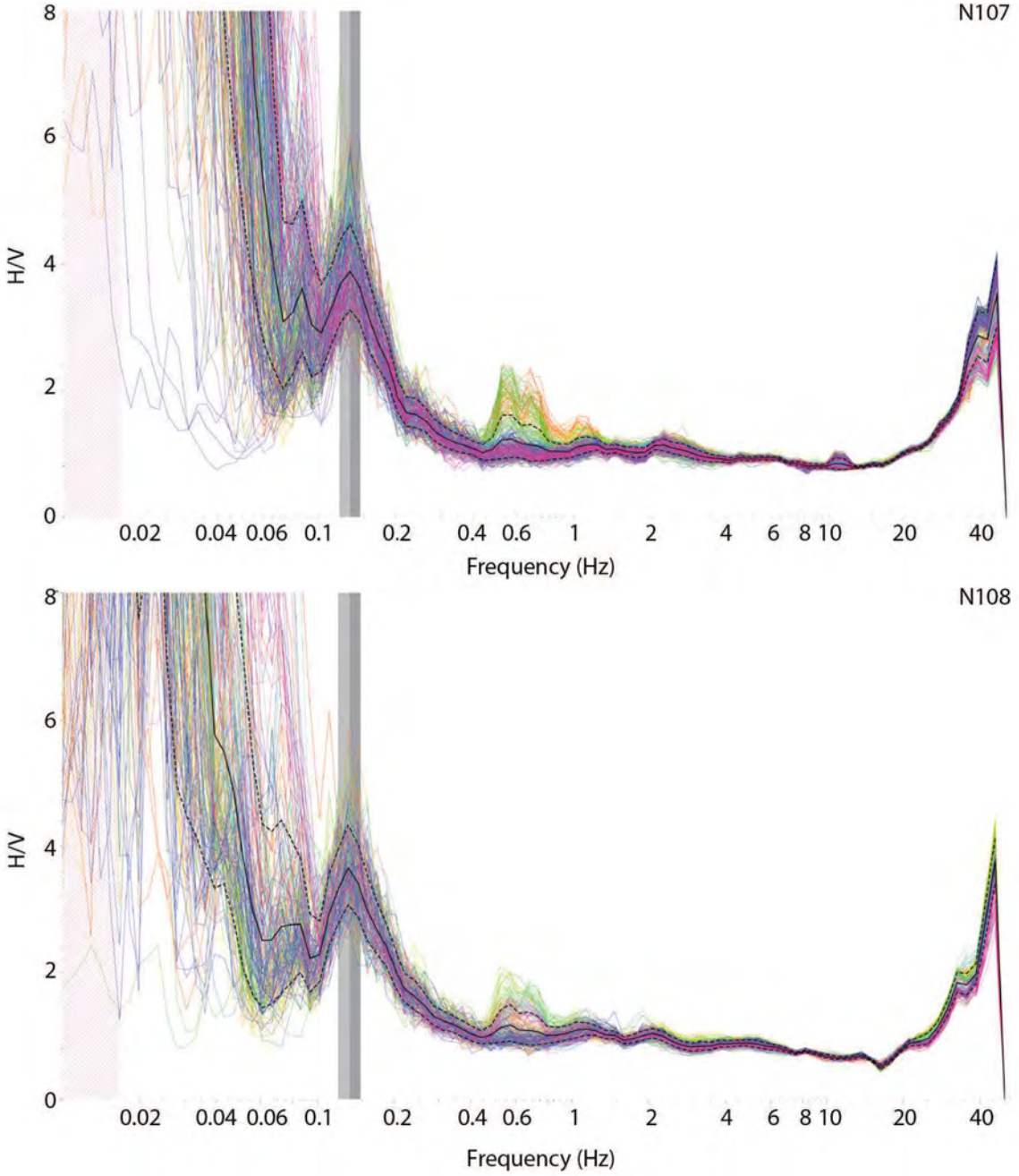

Figure C.4: *Station N107 - N108. Description is the same as figure C.1.*

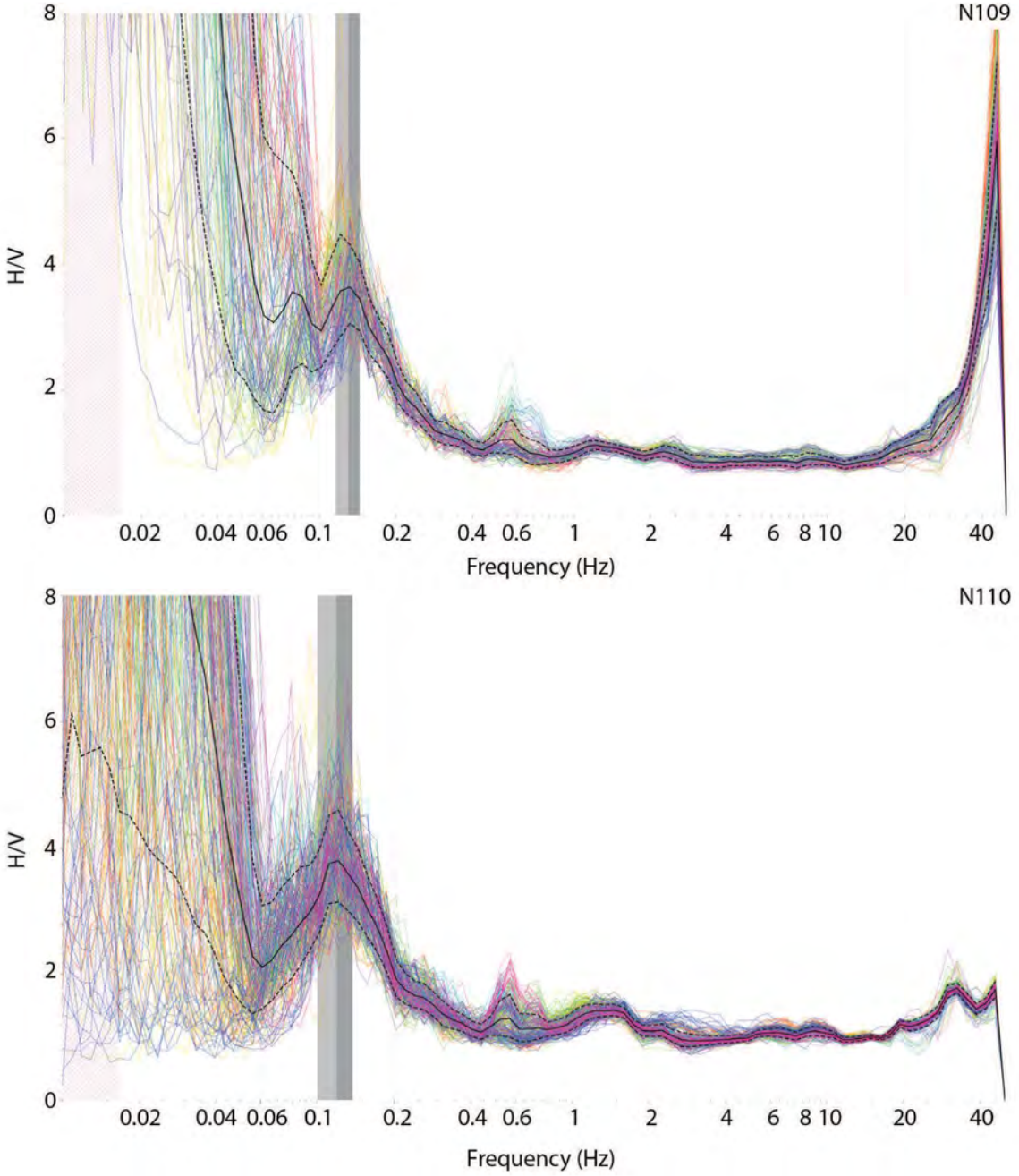

Figure C.5: *Station N109 - N110. Description is the same as figure C.1.*

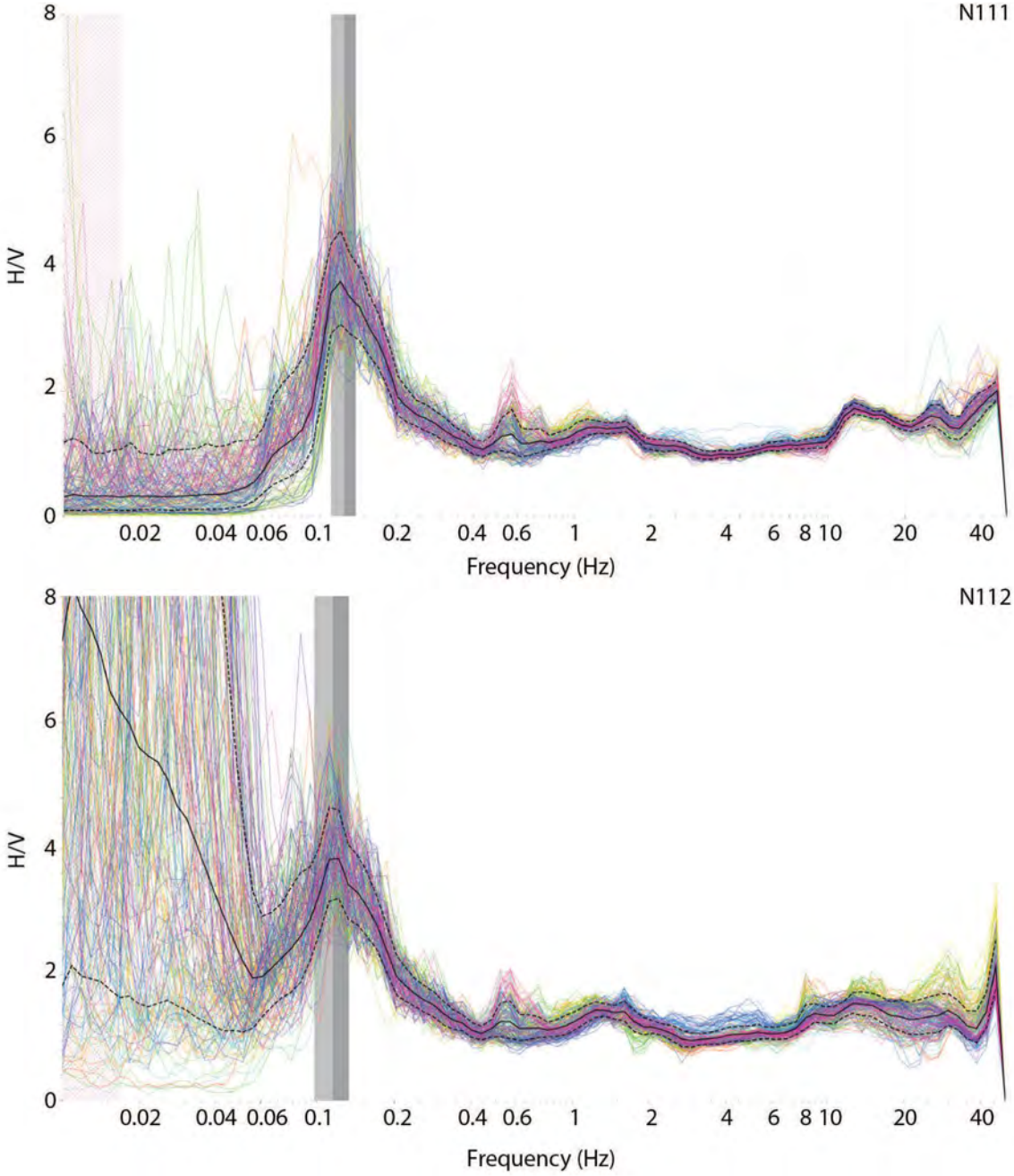

Figure C.6: *Station N111 - N112. Description is the same as figure C.1.*

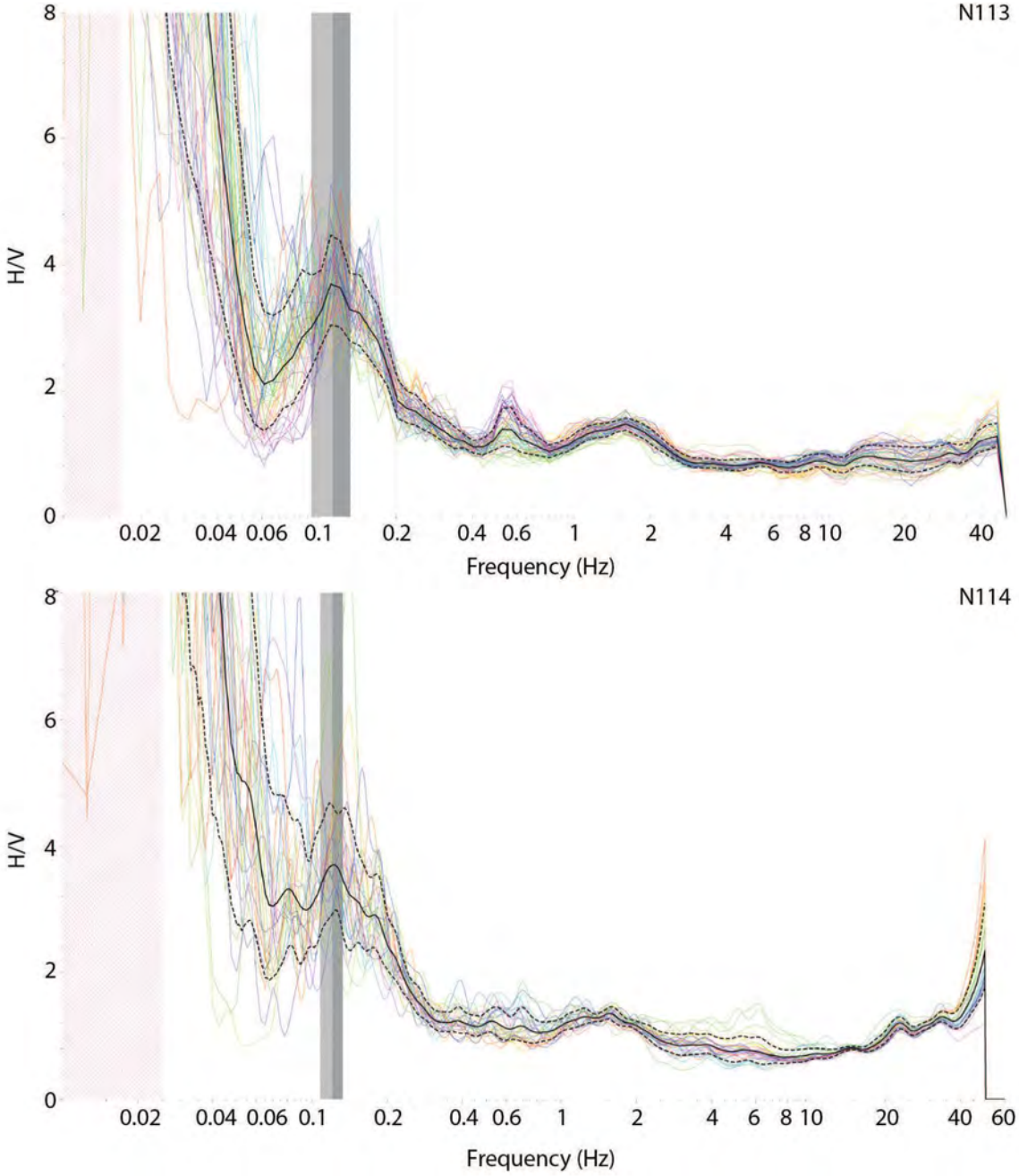

Figure C.7: *Station N113 - N114. Description is the same as figure C.1.*

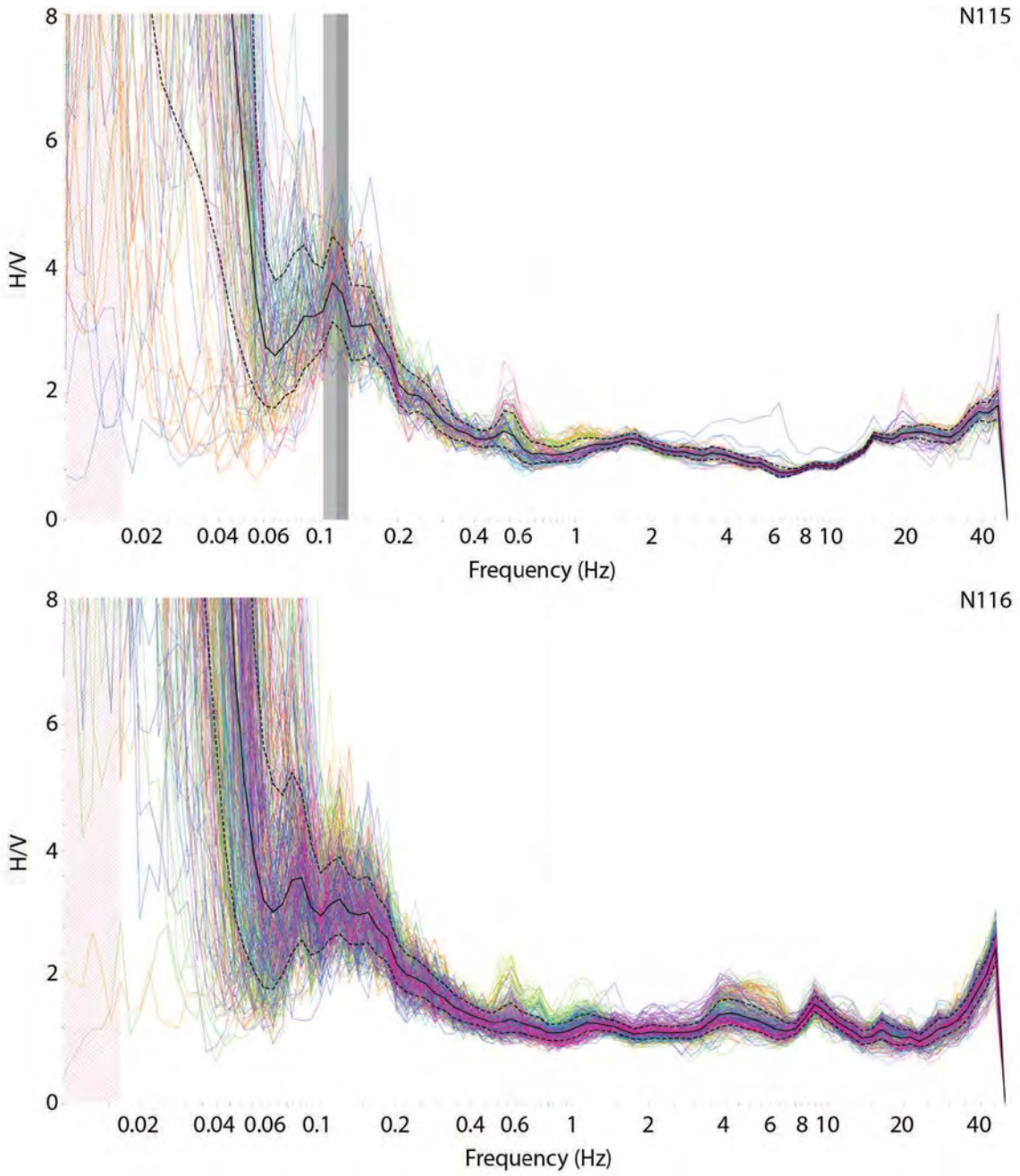

Figure C.8: *Station N115 - N116. Description is the same as figure C.1.*

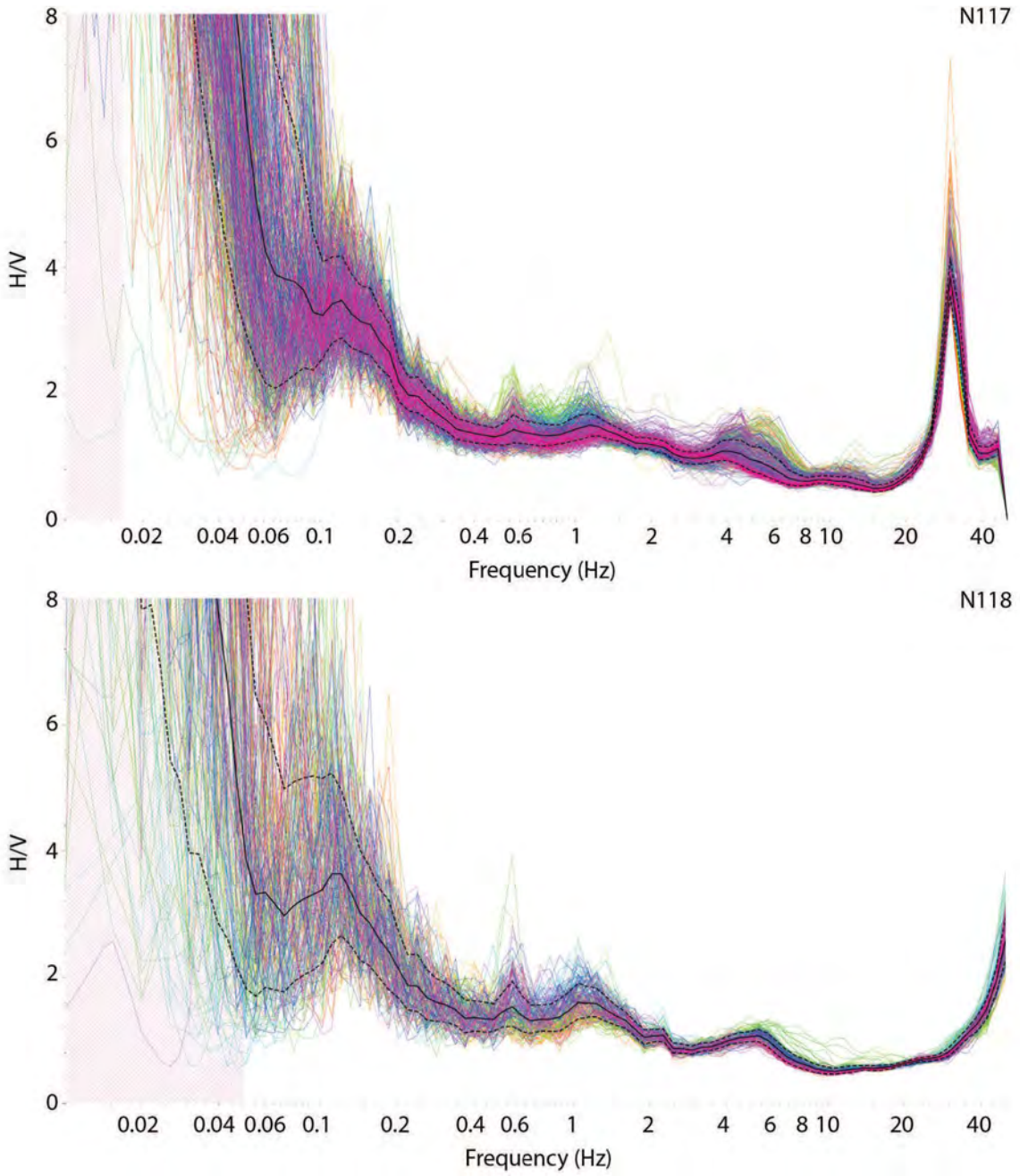

Figure C.9: *Station N117 - N118. Description is the same as figure C.1.*

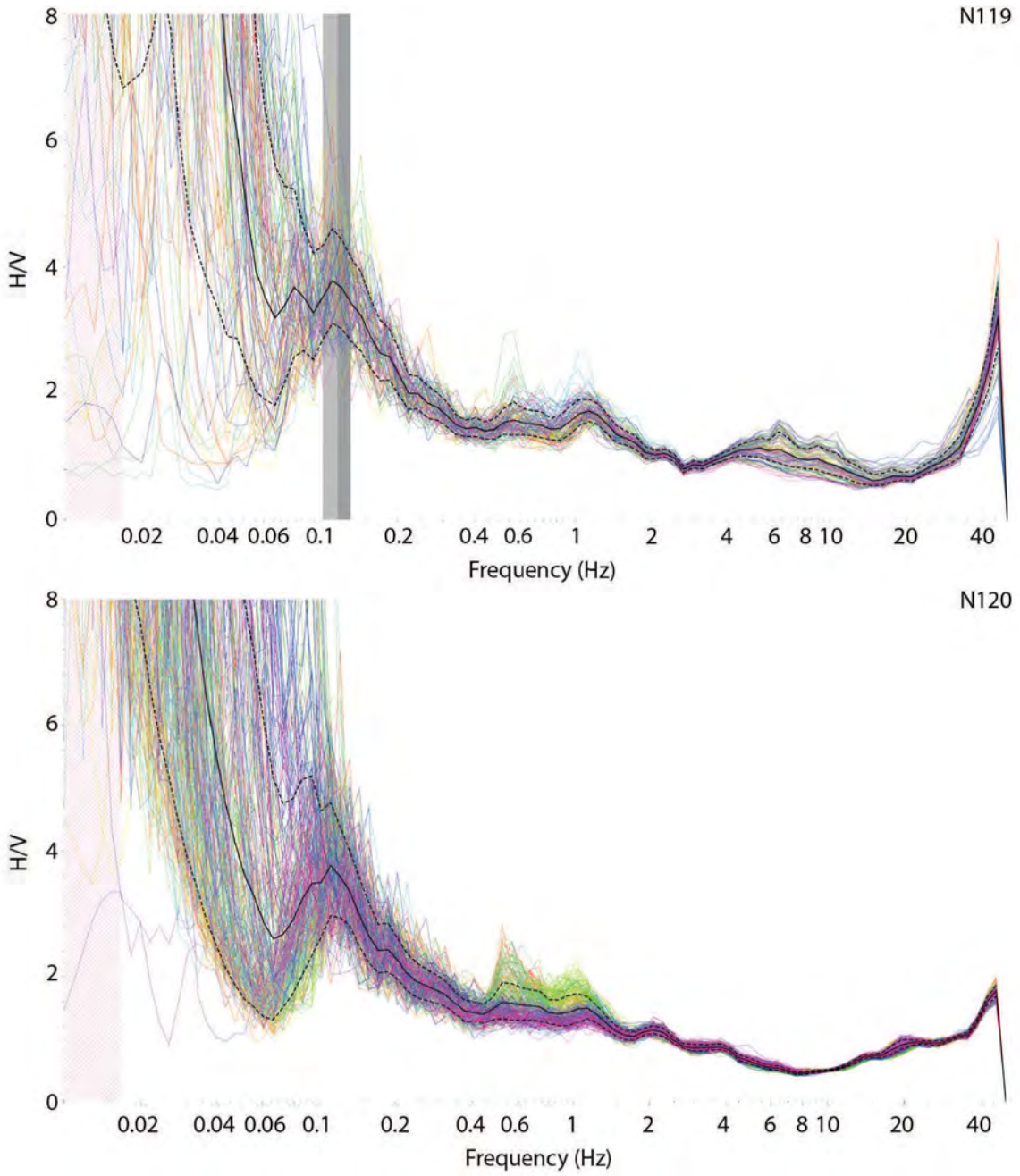

Figure C.10: *Station N119 - N120. Description is the same as figure C.1.*

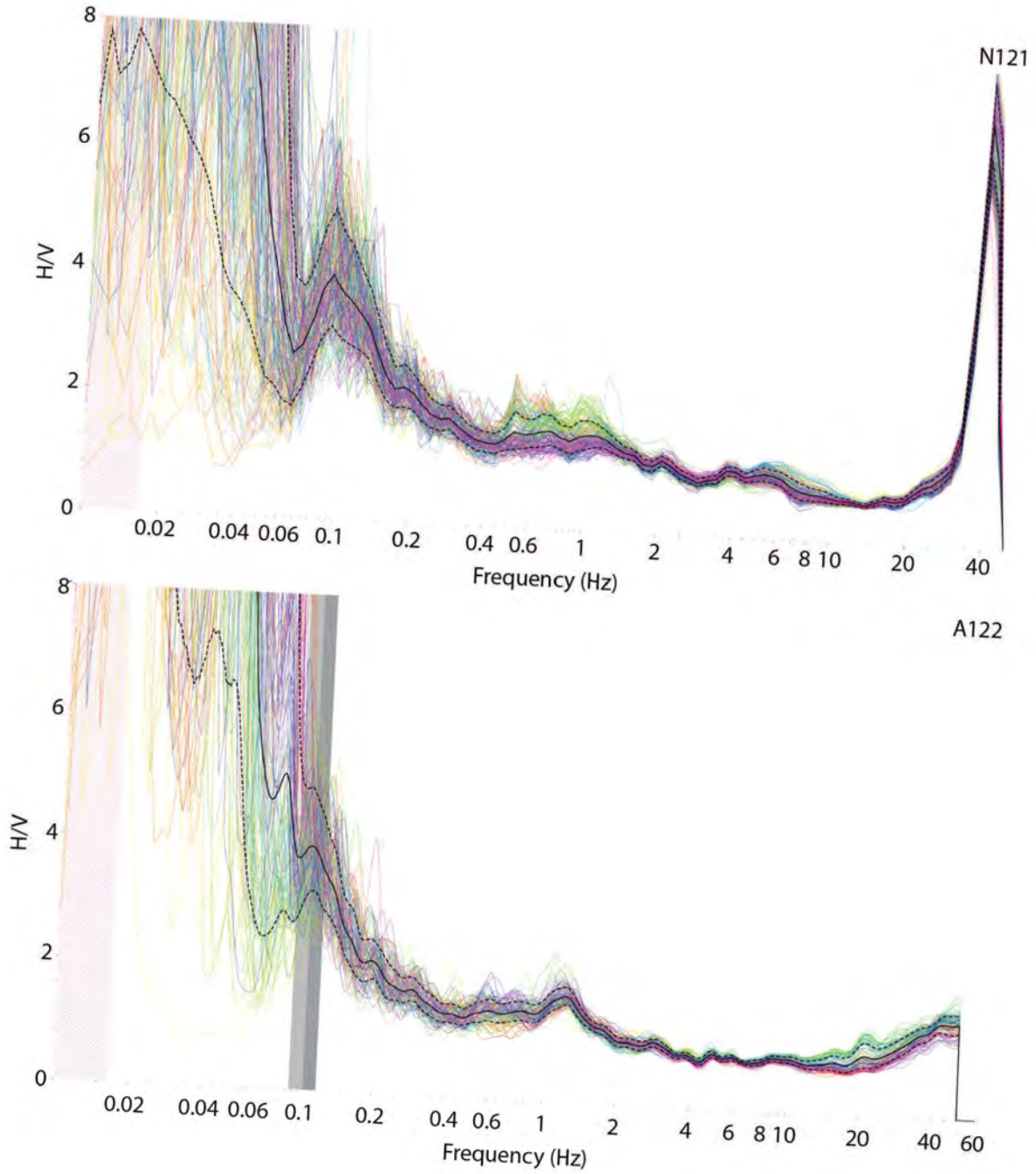

Figure C.11: *Station N121 - A122. Description is the same as figure C.1.*

NO DATA AVAILABLE FOR STATION A123

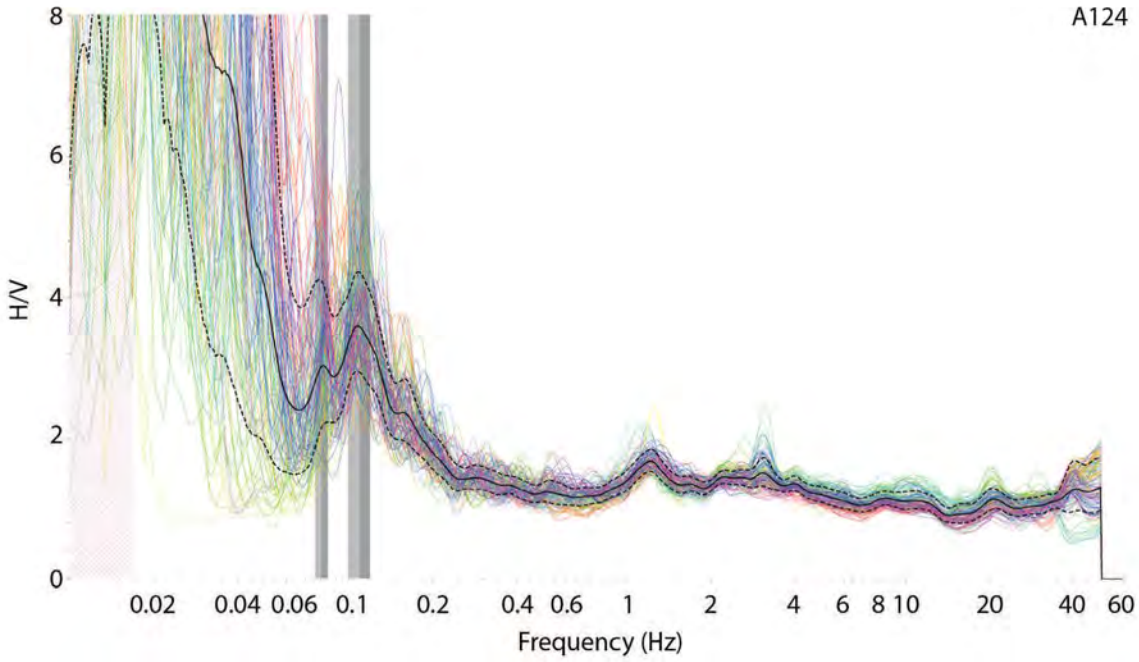

Figure C.12: *Station A123 - A124. Description is the same as figure C.1.*

NO DATA AVAILABLE FOR STATION A125

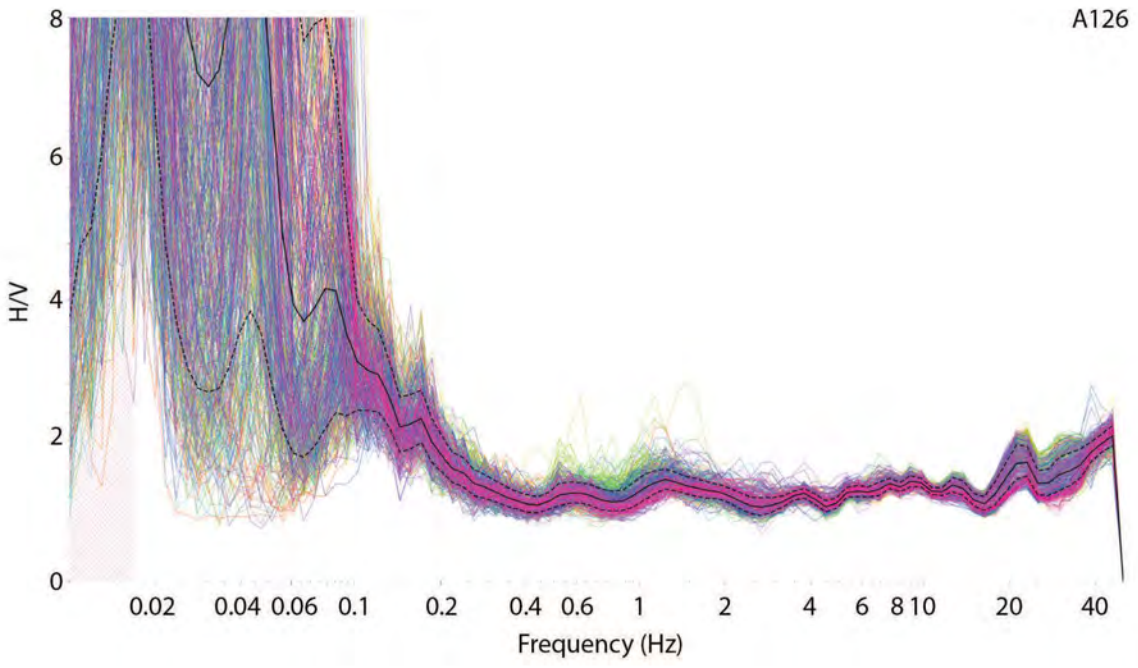

Figure C.13: *Station A125 - A126. Description is the same as figure C.1.*

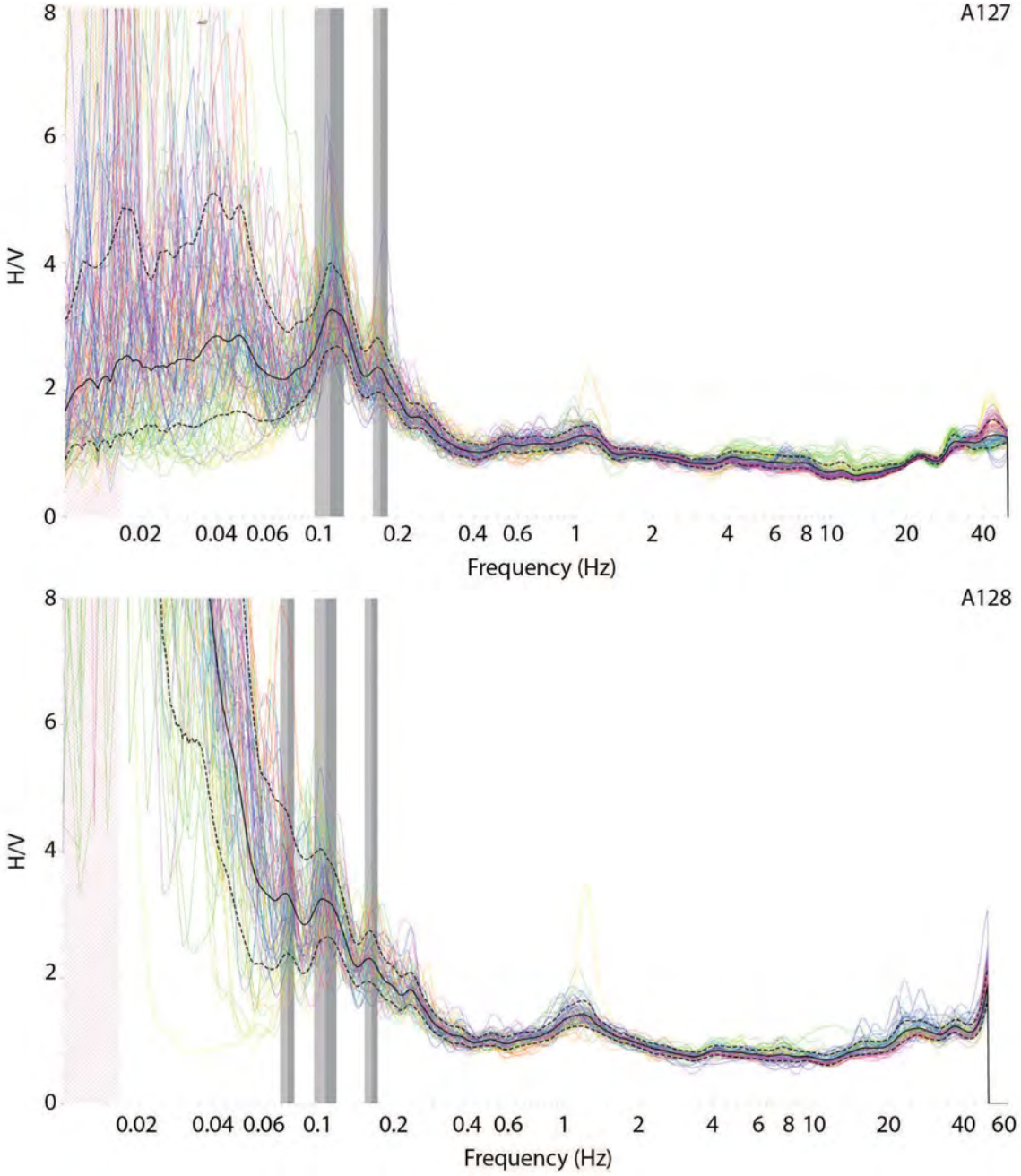

Figure C.14: *Station A127 - A128. Description is the same as figure C.1.*

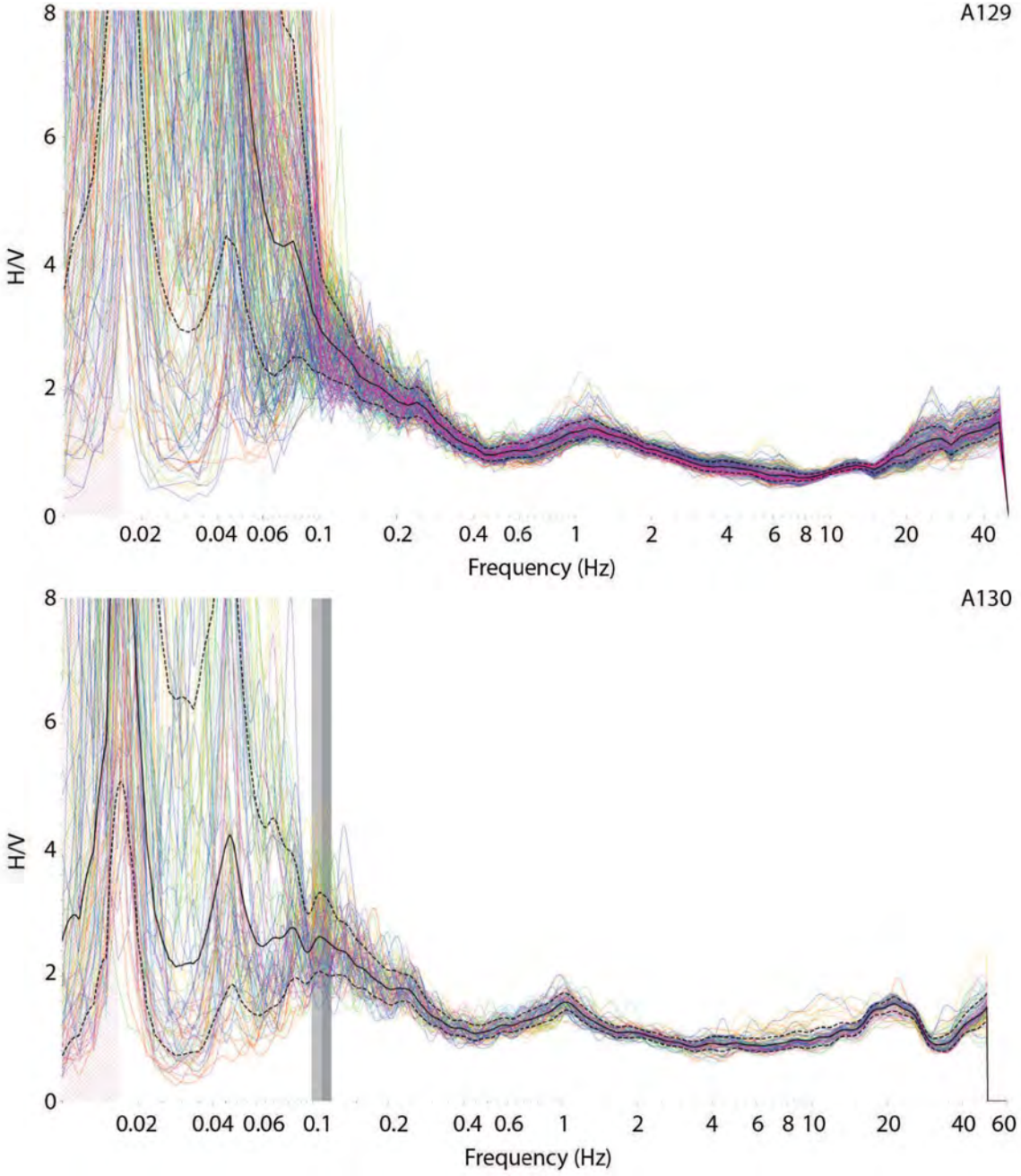

Figure C.15: *Station A129 - A130. Description is the same as figure C.1.*

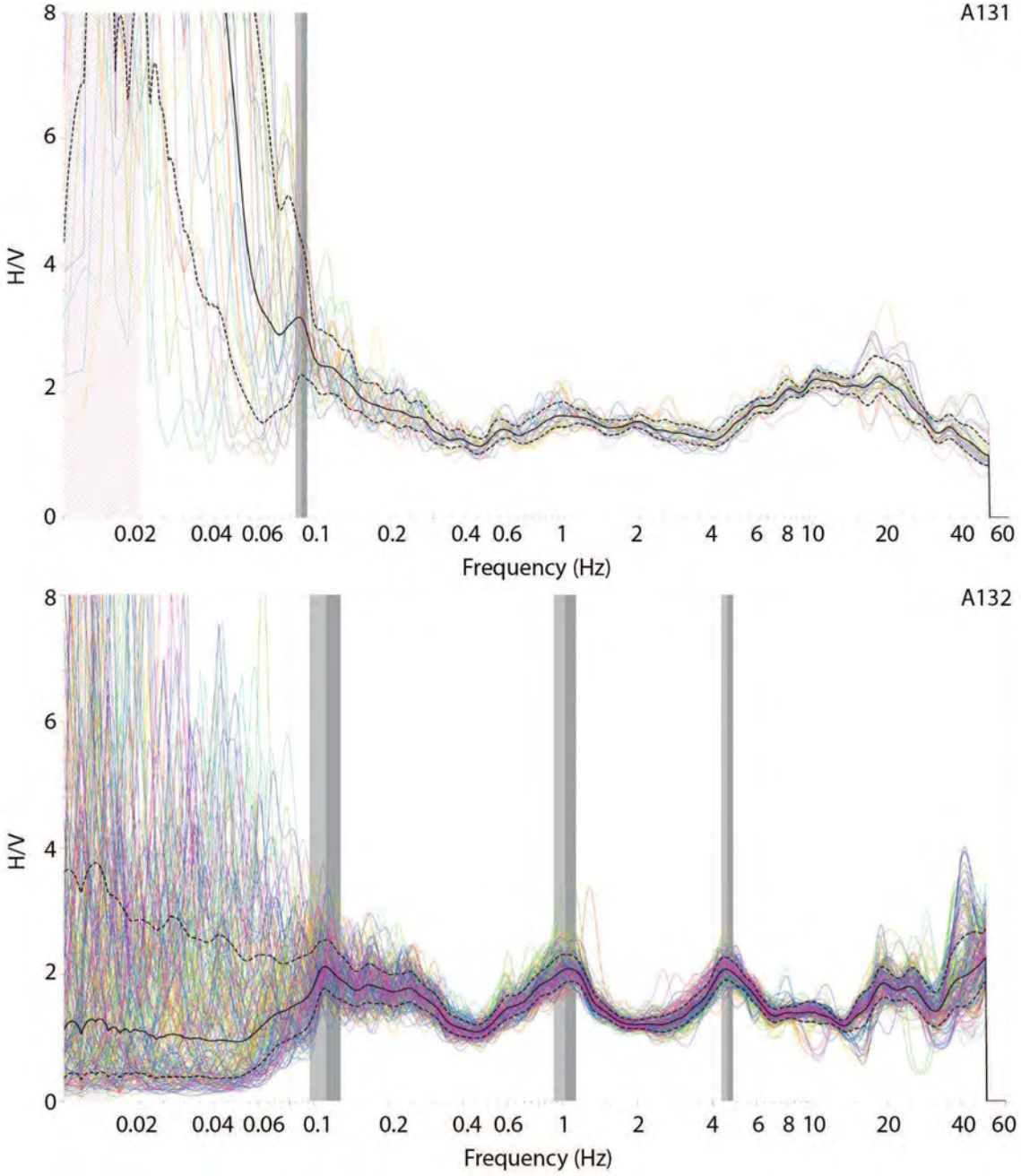

Figure C.16: *Station A131 - A132. Description is the same as figure C.1.*

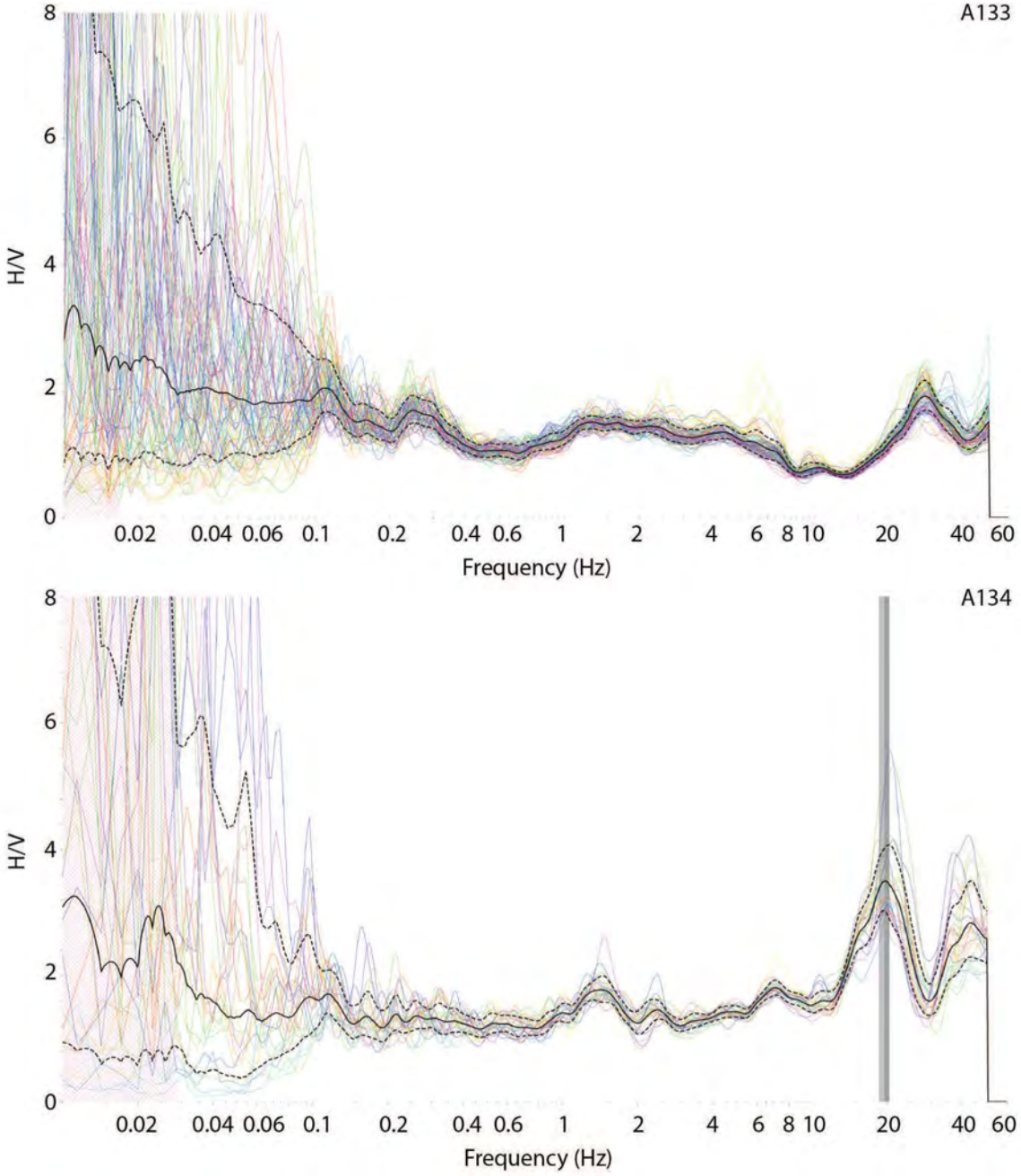

Figure C.17: *Station A133 - A134. Description is the same as figure C.1.*

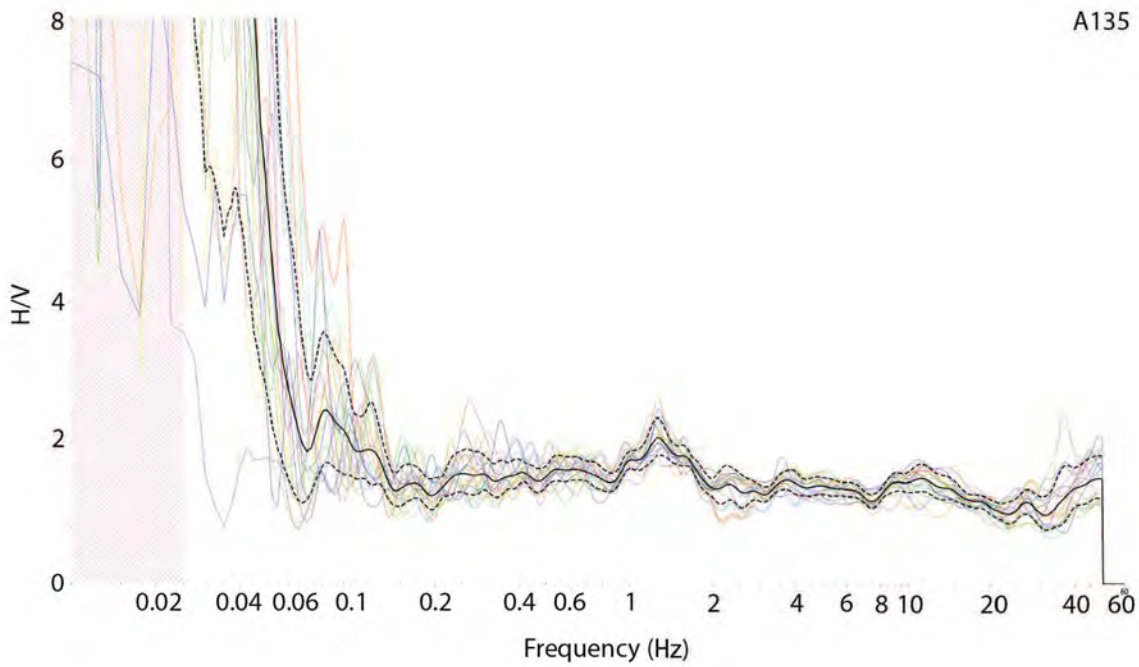

NO DATA AVAILABLE FOR STATION A136

Figure C.18: *Station A135 - A136. Description is the same as figure C.1.*

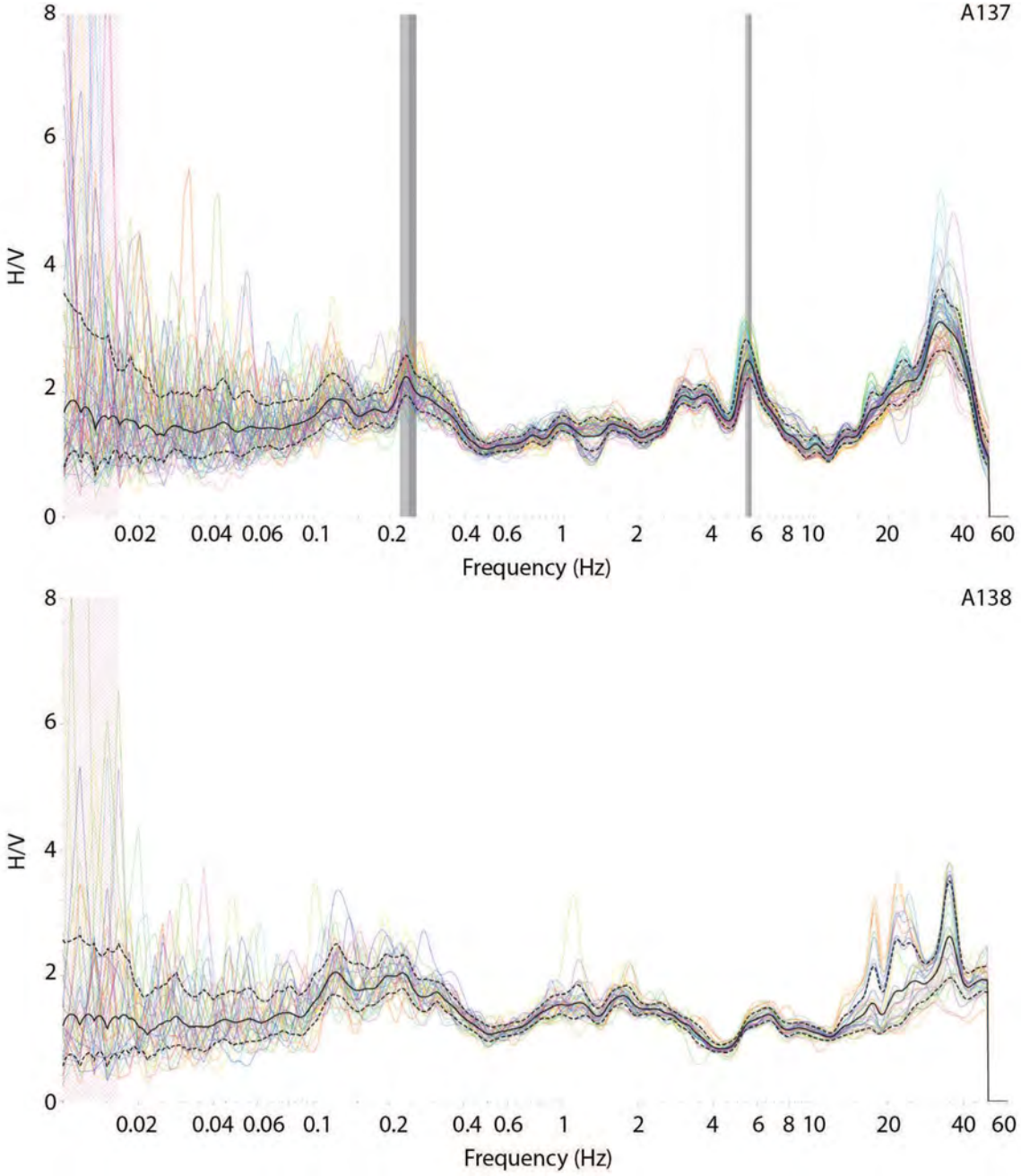

Figure C.19: *Station A137 - A138. Description is the same as figure C.1.*

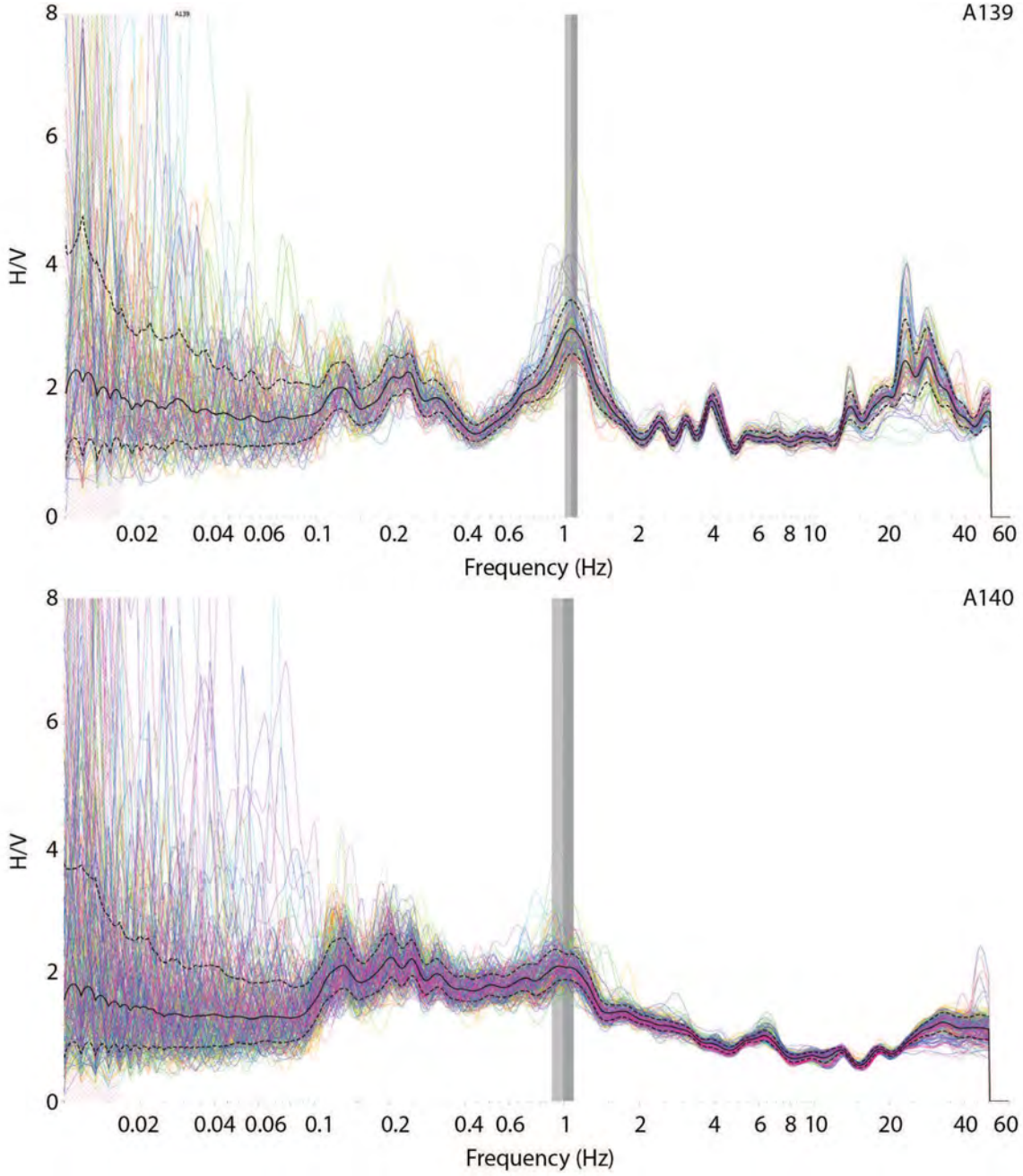

Figure C.20: *Station A139 - A140. Description is the same as figure C.1.*

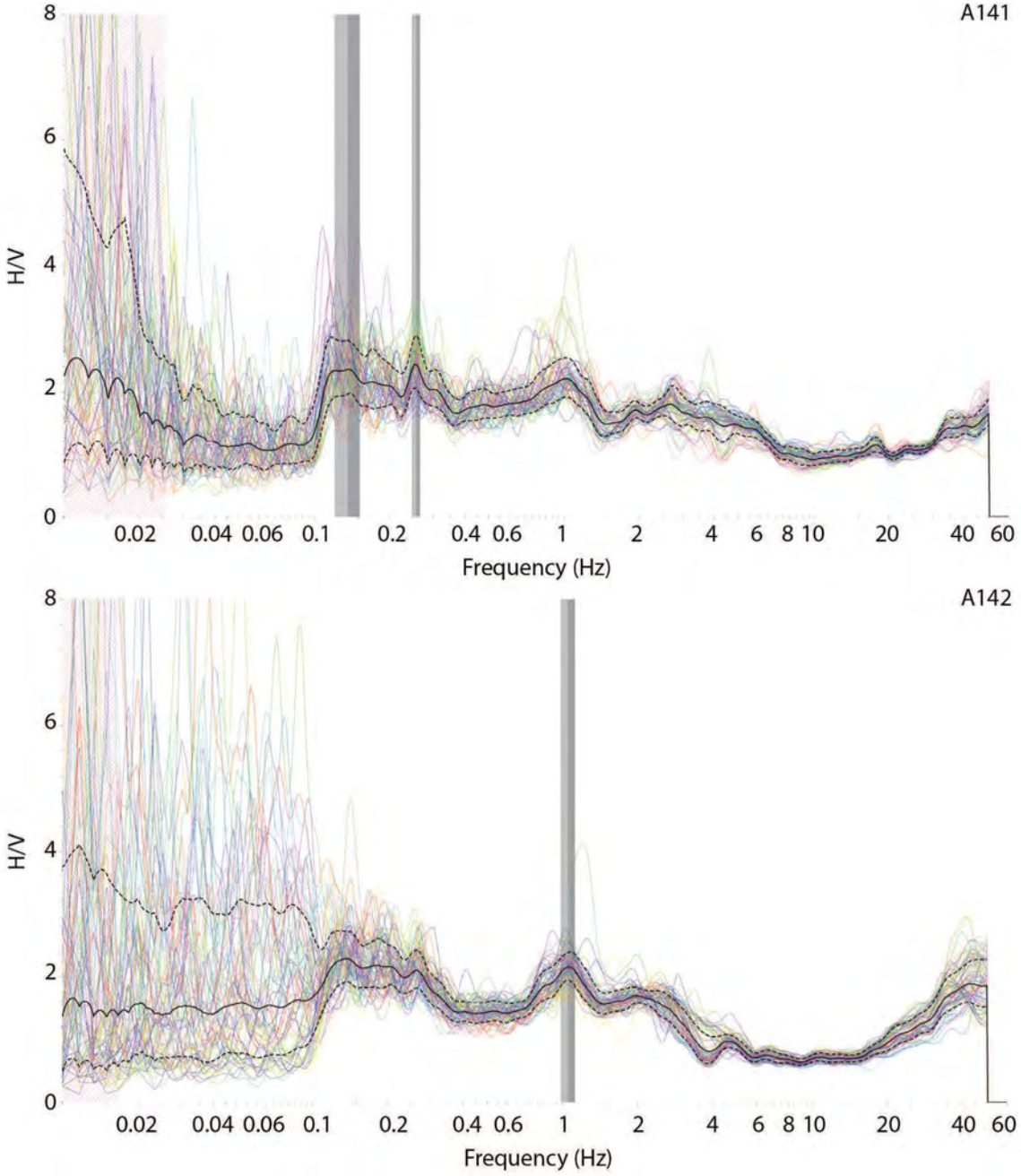

Figure C.21: *Station A141 - A142. Description is the same as figure C.1.*

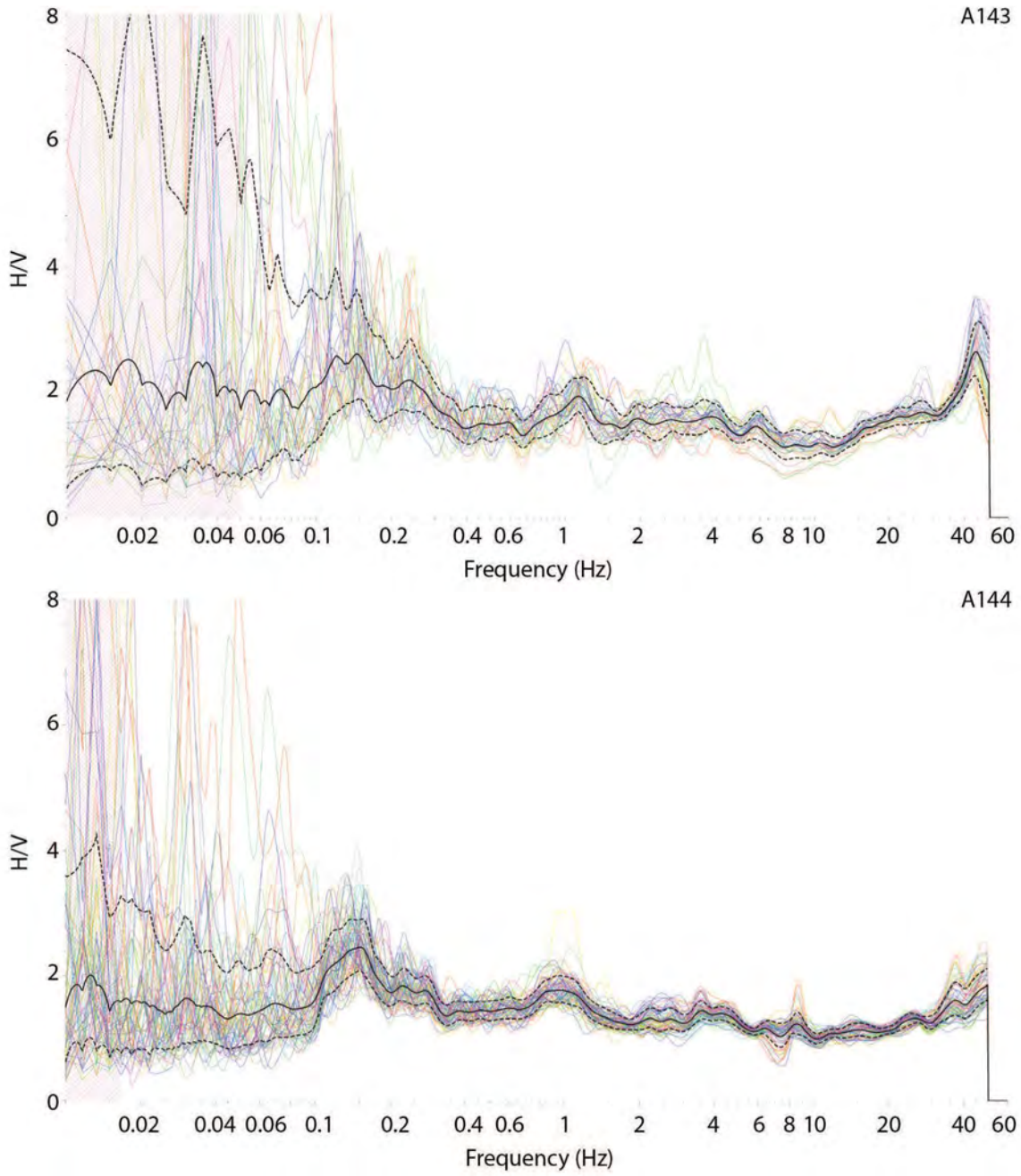

Figure C.22: *Station A143 - A144. Description is the same as figure C.1.*

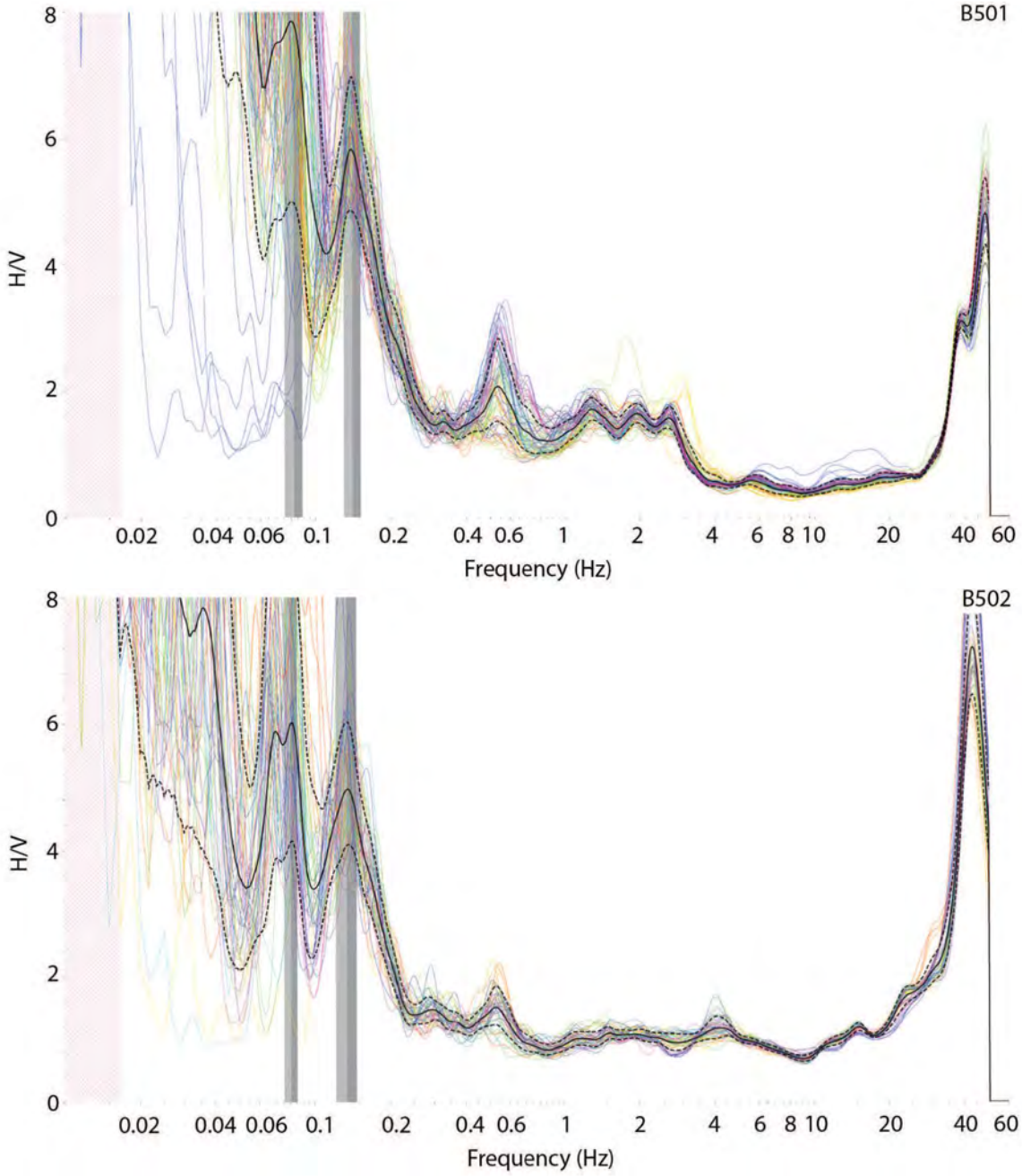

Figure C.23: *Station B501 - B502. Description is the same as figure C.1.*

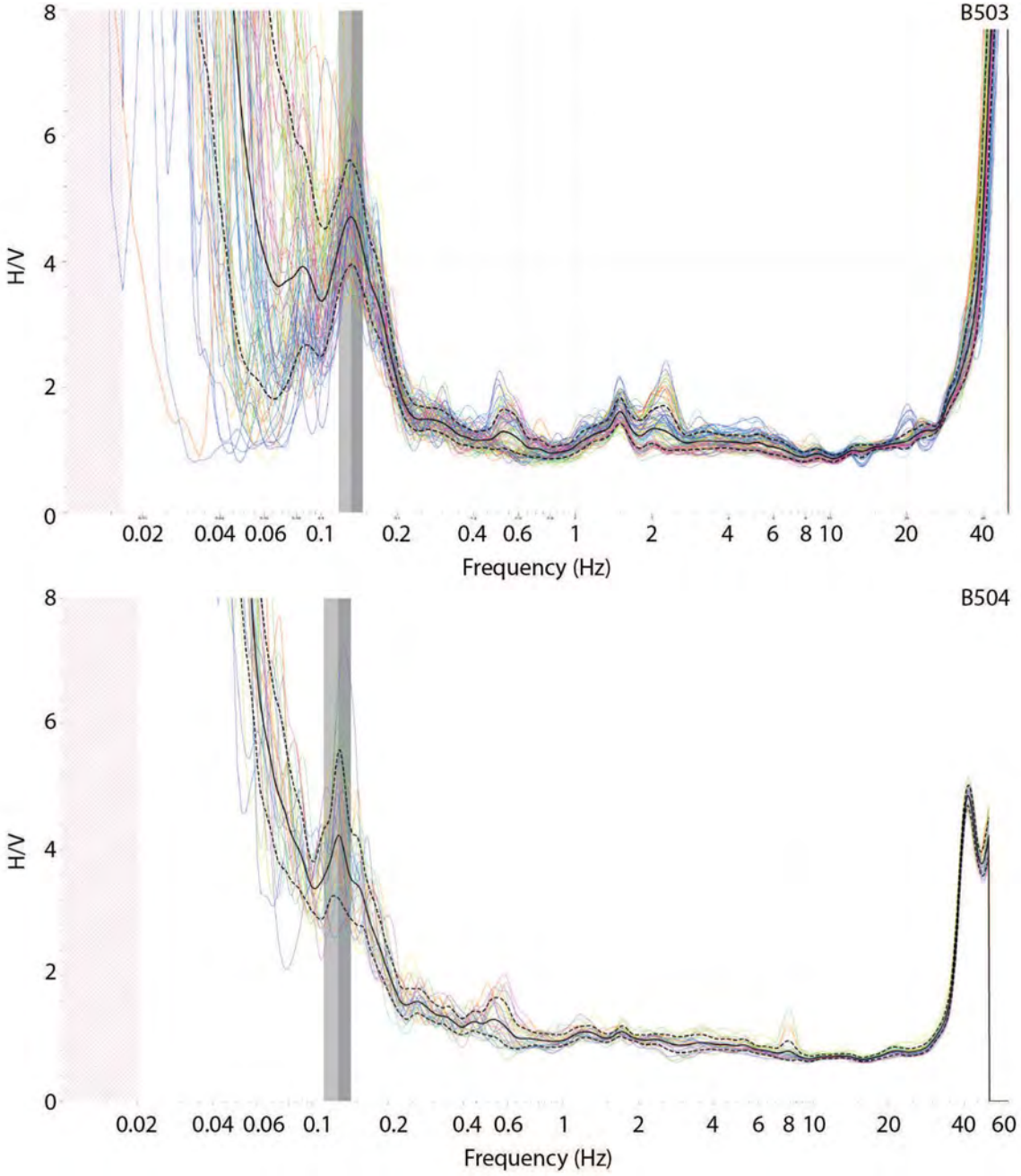

Figure C.24: *Station B503 - B504. Description is the same as figure C.1.*

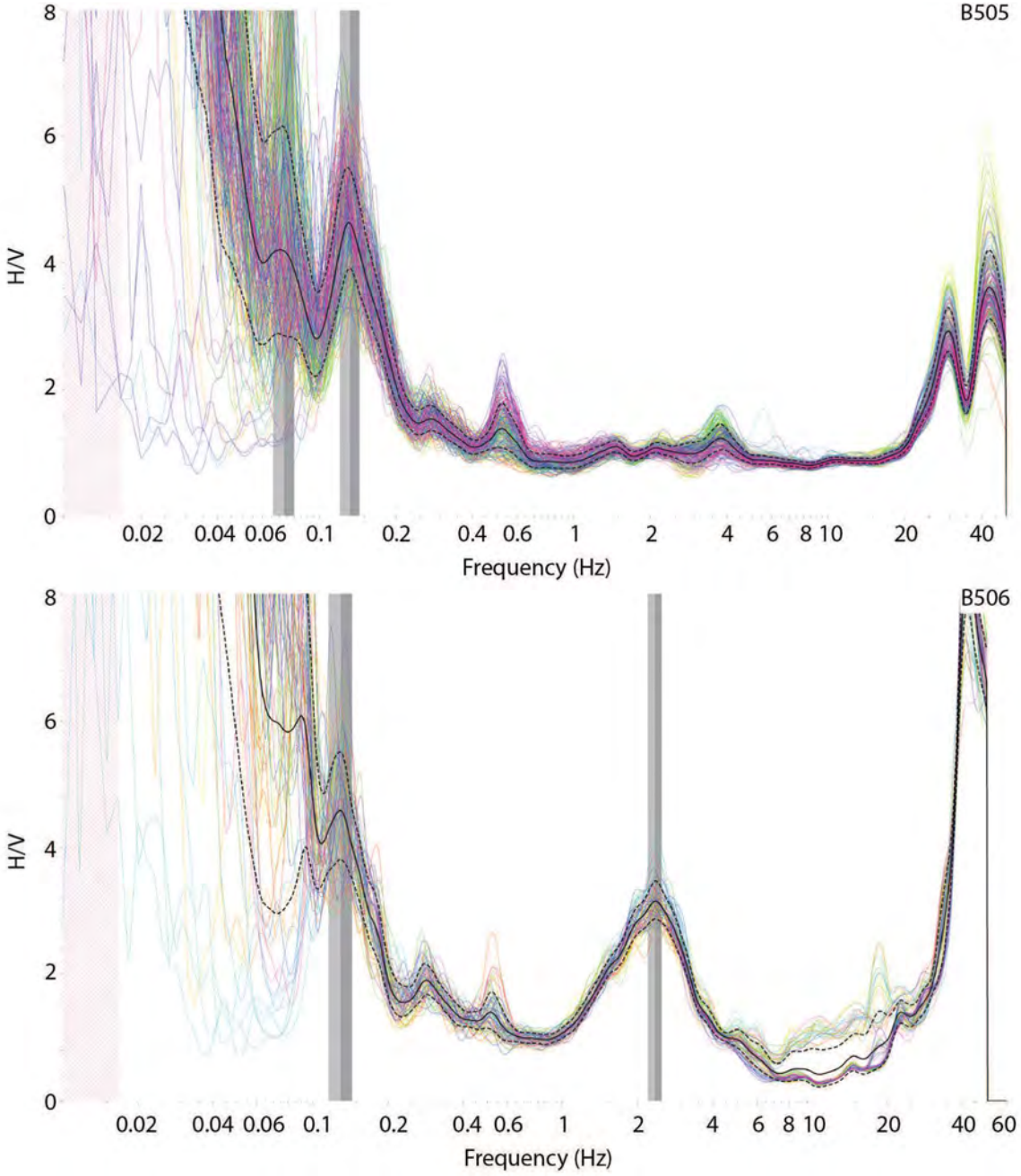

Figure C.25: *Station B505 - B506. Description is the same as figure C.1.*

NO DATA AVAILABLE FOR STATION B507

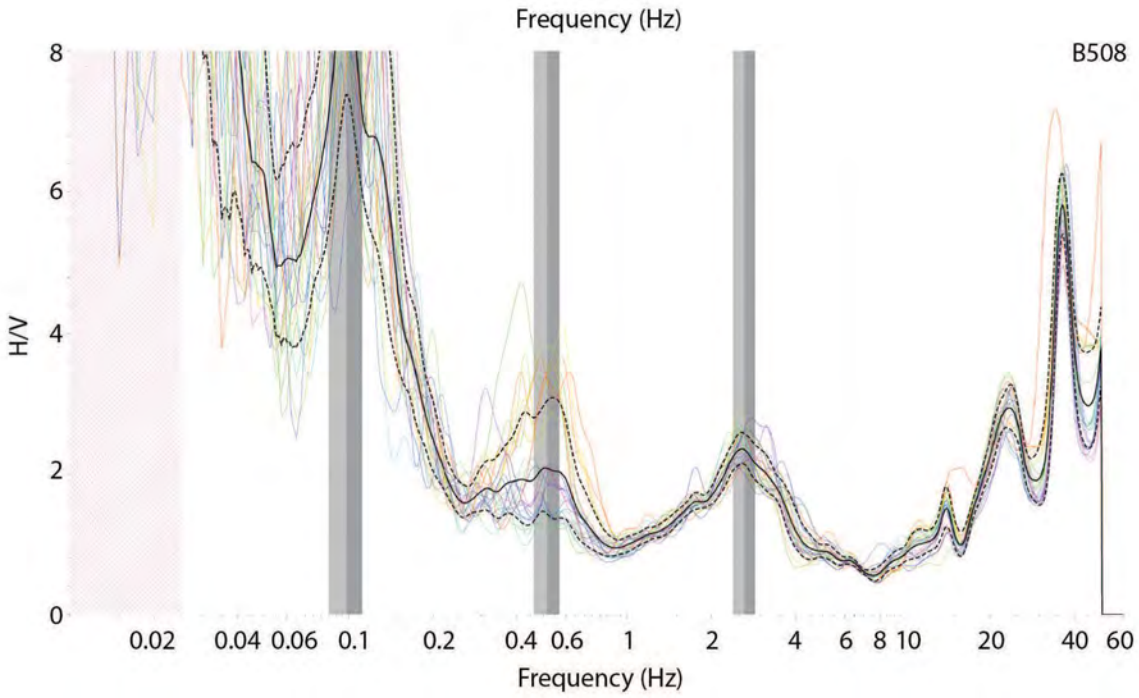

Figure C.26: *Station B507 - B508. Description is the same as figure C.1.*

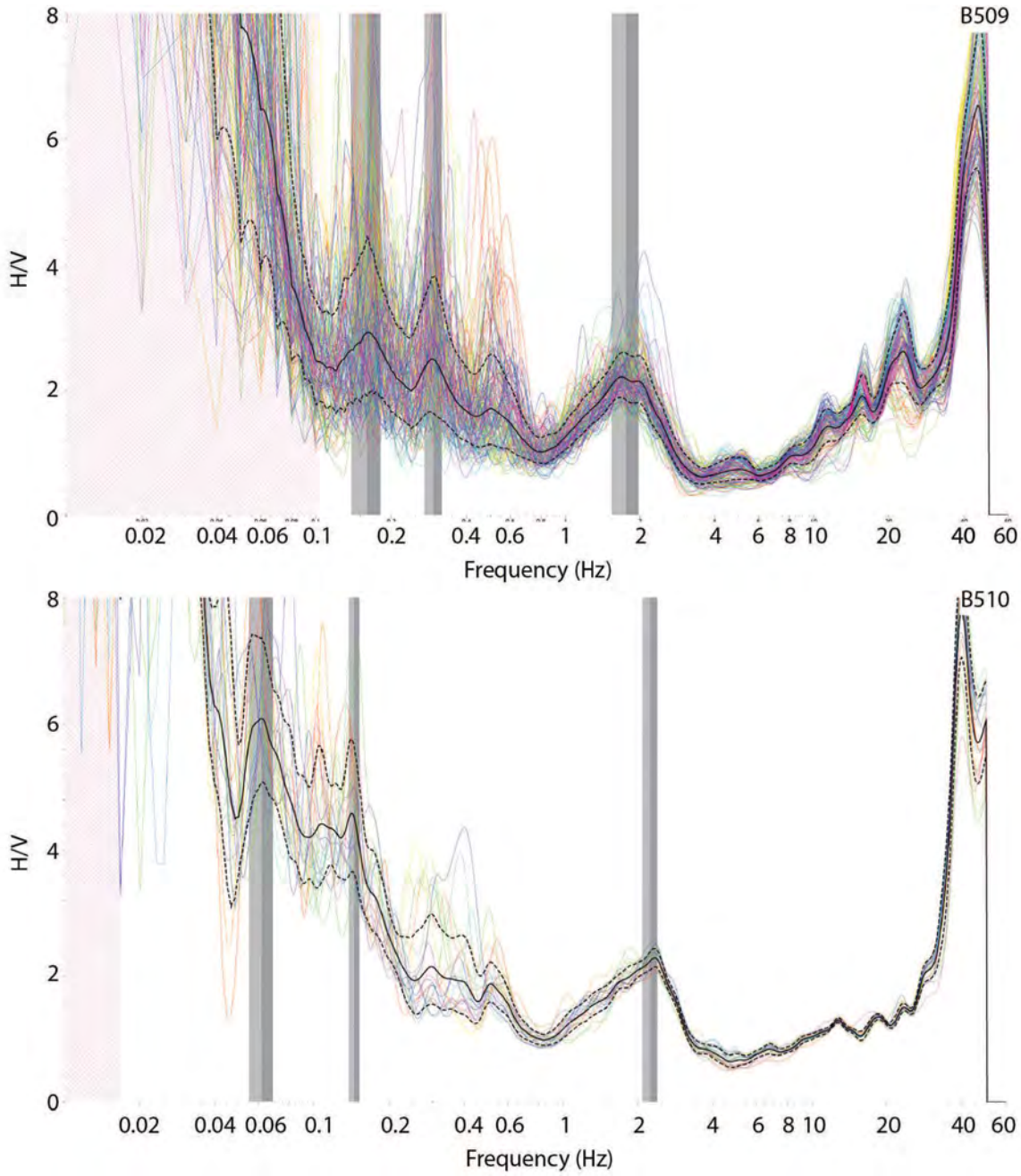

Figure C.27: *Station B509 - B510. Description is the same as figure C.1.*

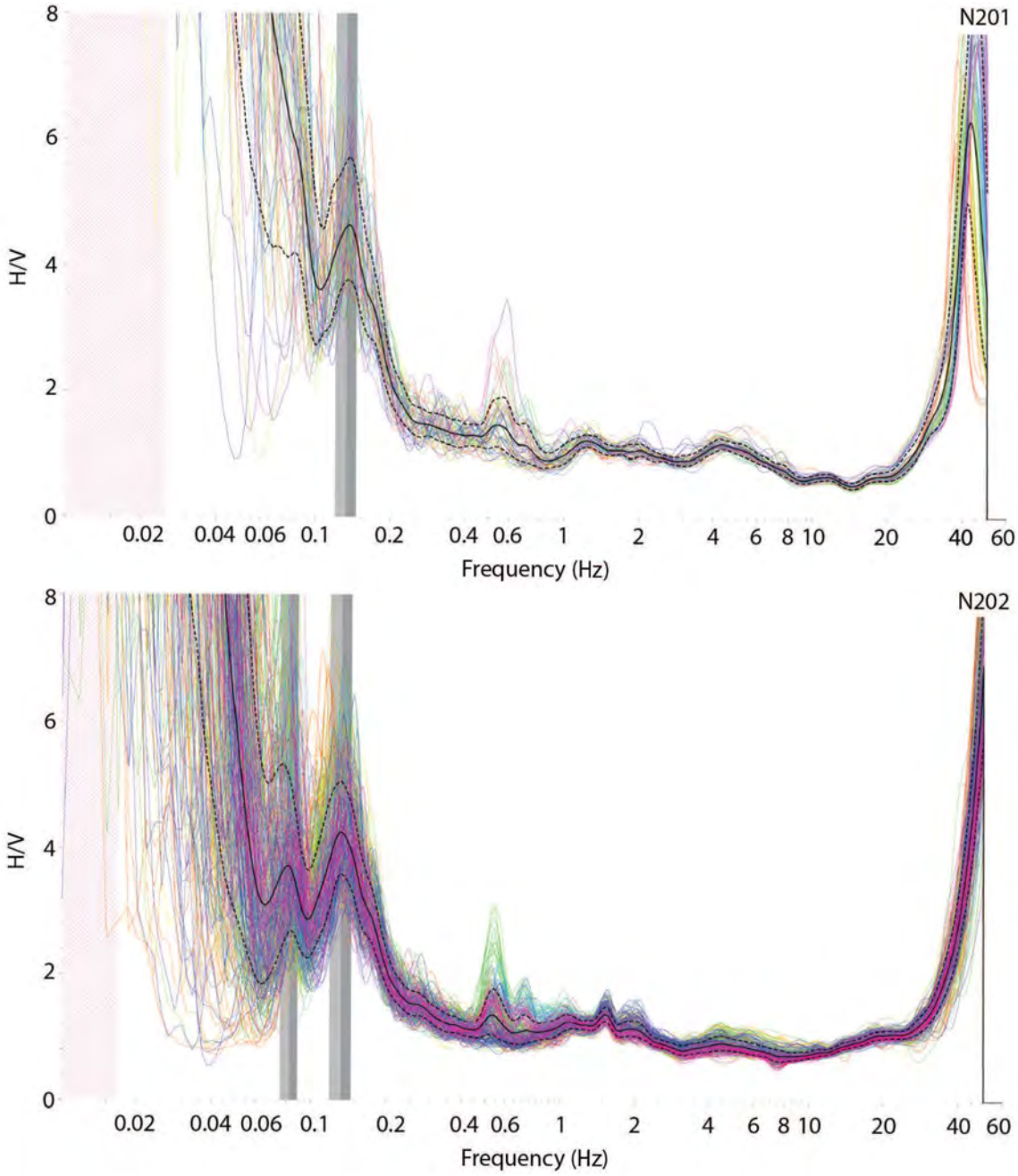

Figure C.28: *Station N201 - N202. Description is the same as figure C.1.*

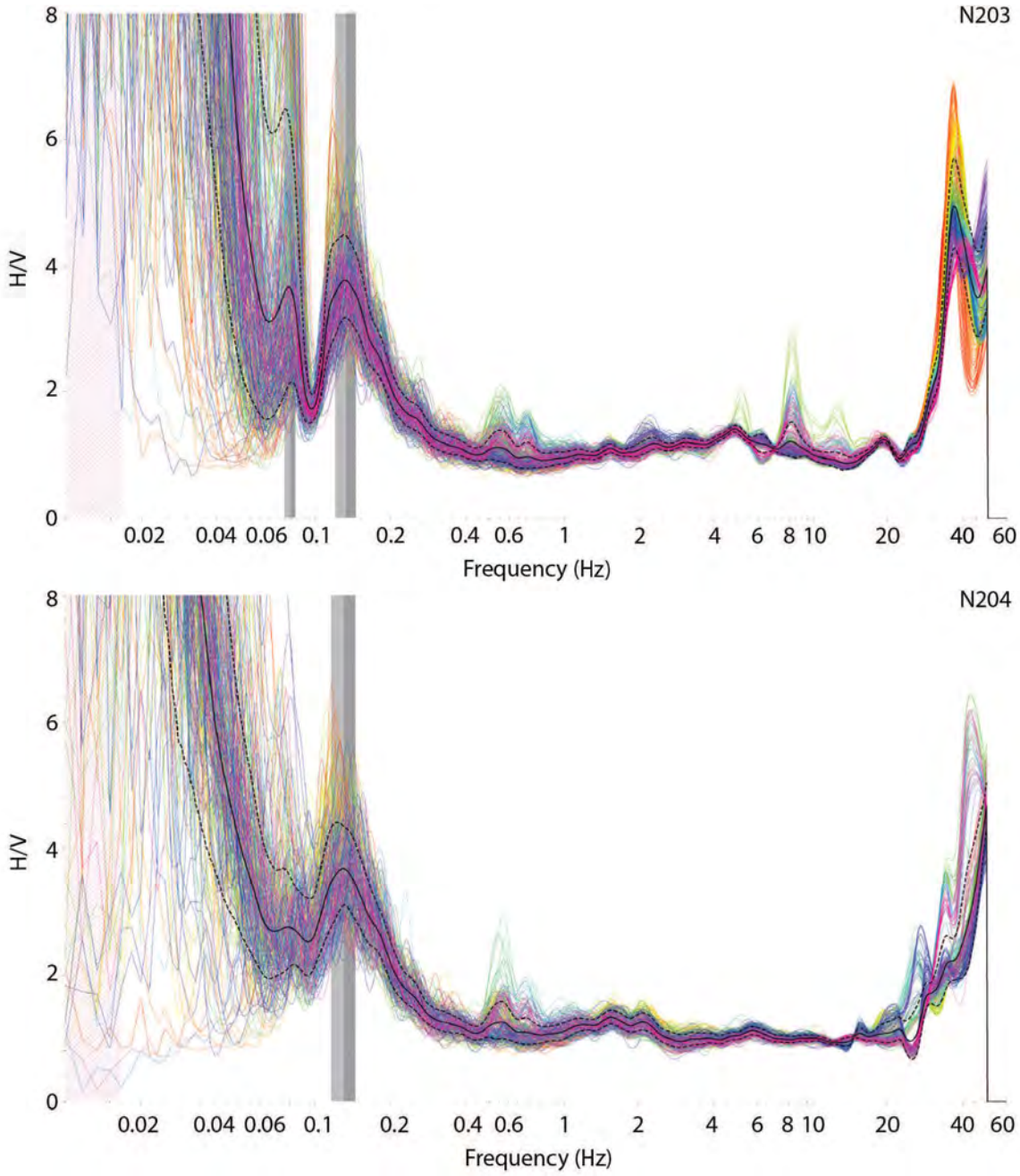

Figure C.29: *Station N203 - N204. Description is the same as figure C.1.*

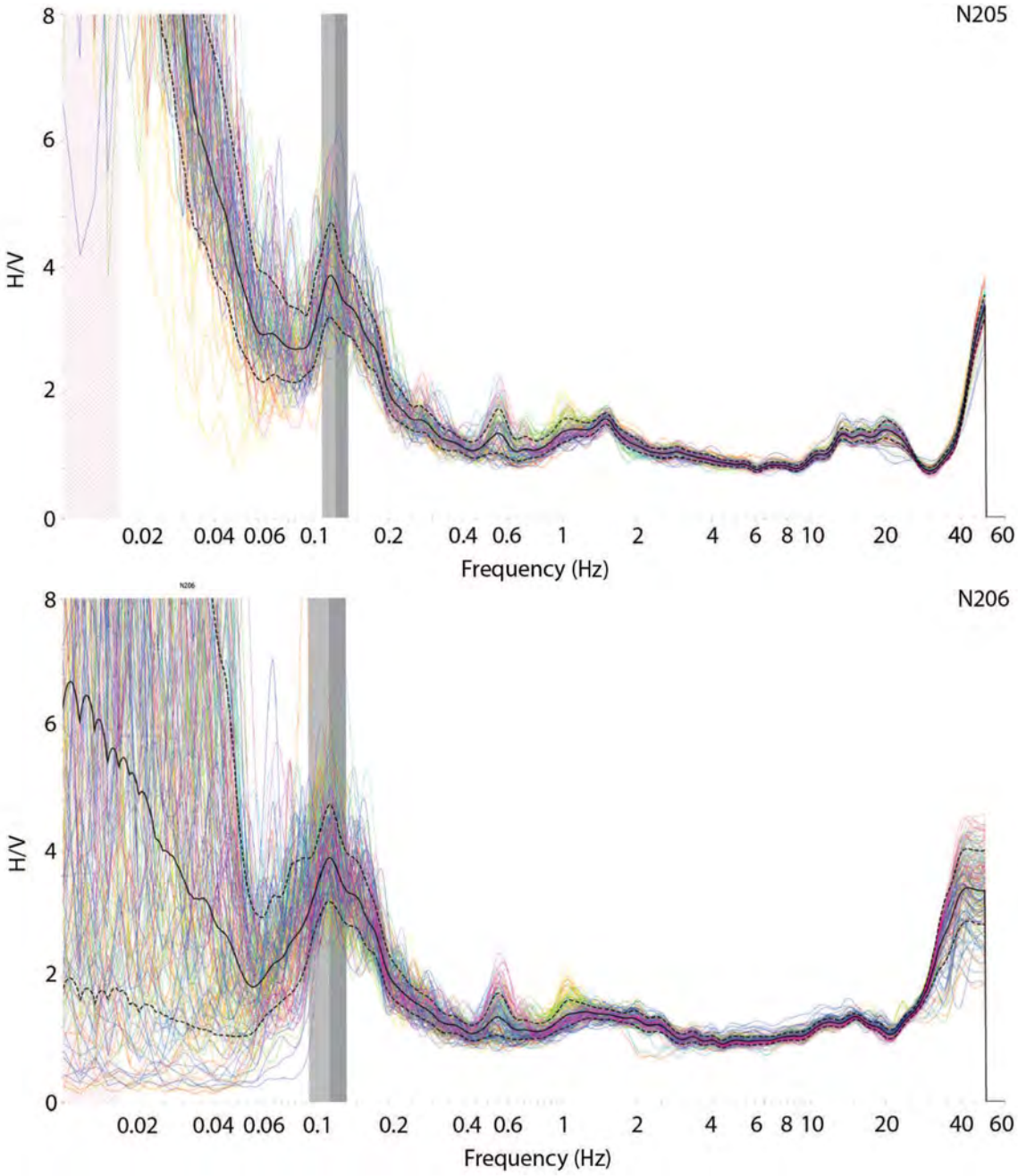

Figure C.30: *Station N205 - N206. Description is the same as figure C.1.*

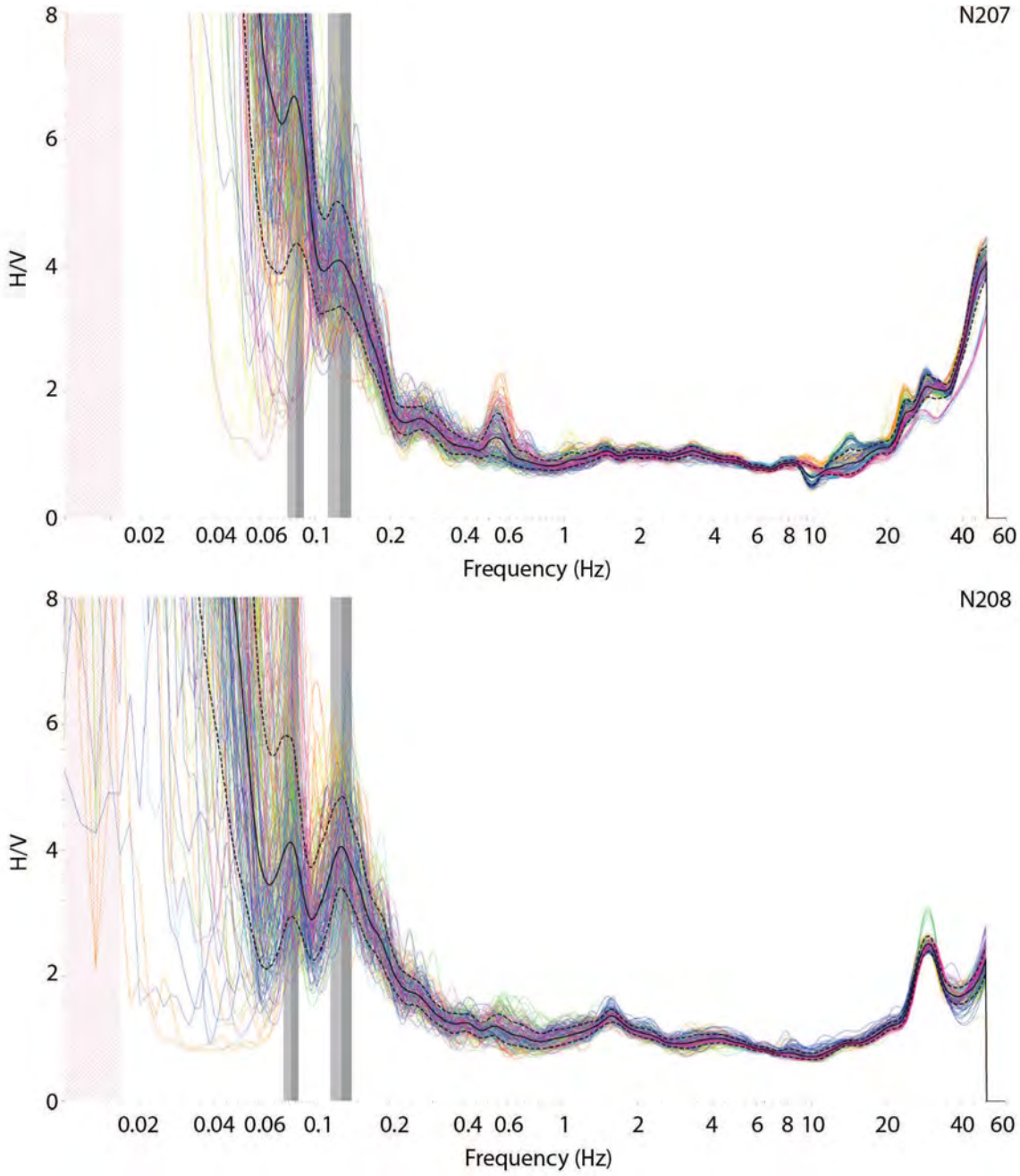

Figure C.31: *Station N207 - N208. Description is the same as figure C.1.*

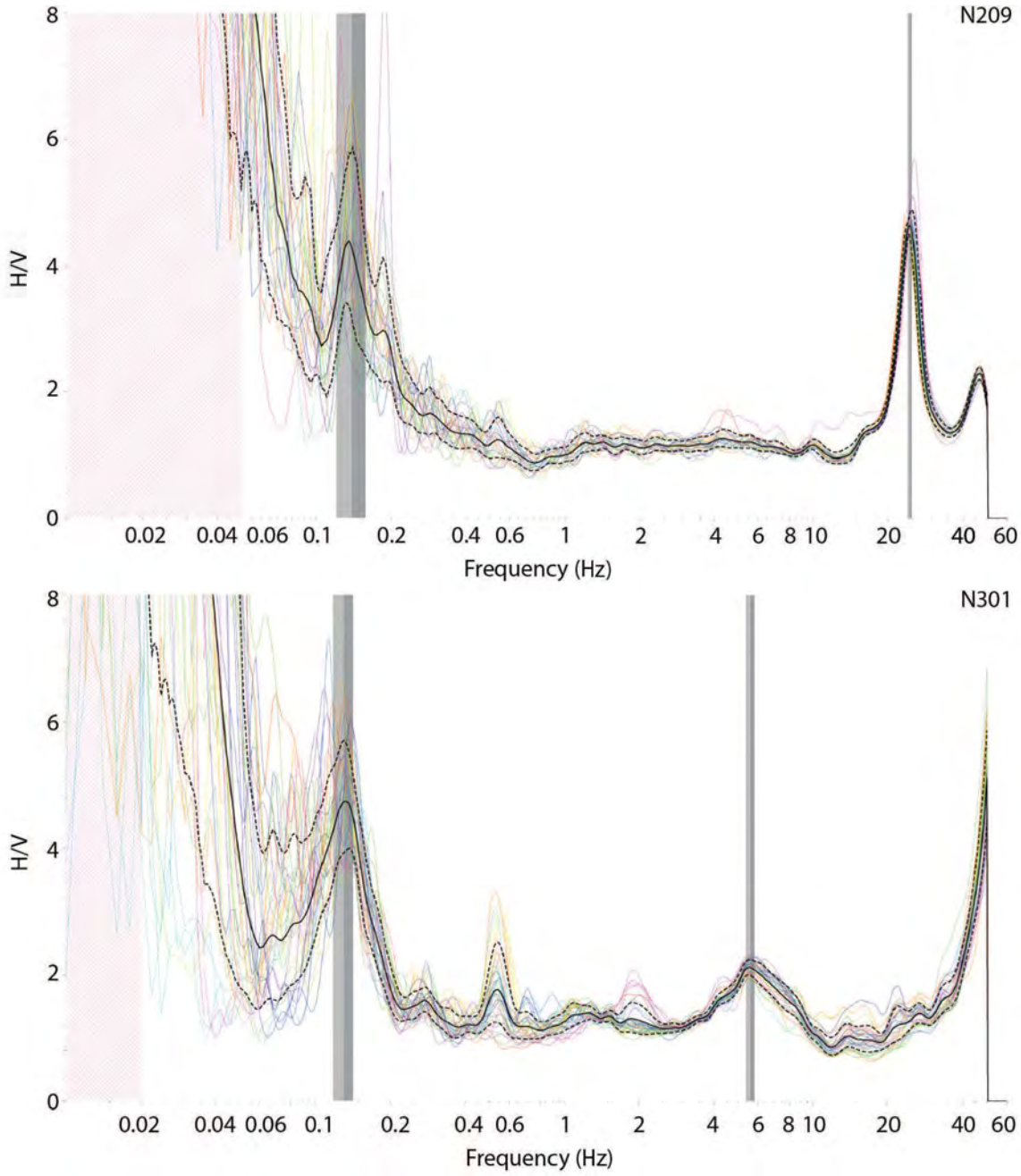

Figure C.32: *Station N209 - N301. Description is the same as figure C.1.*

NO DATA AVAILABLE FOR STATION B302

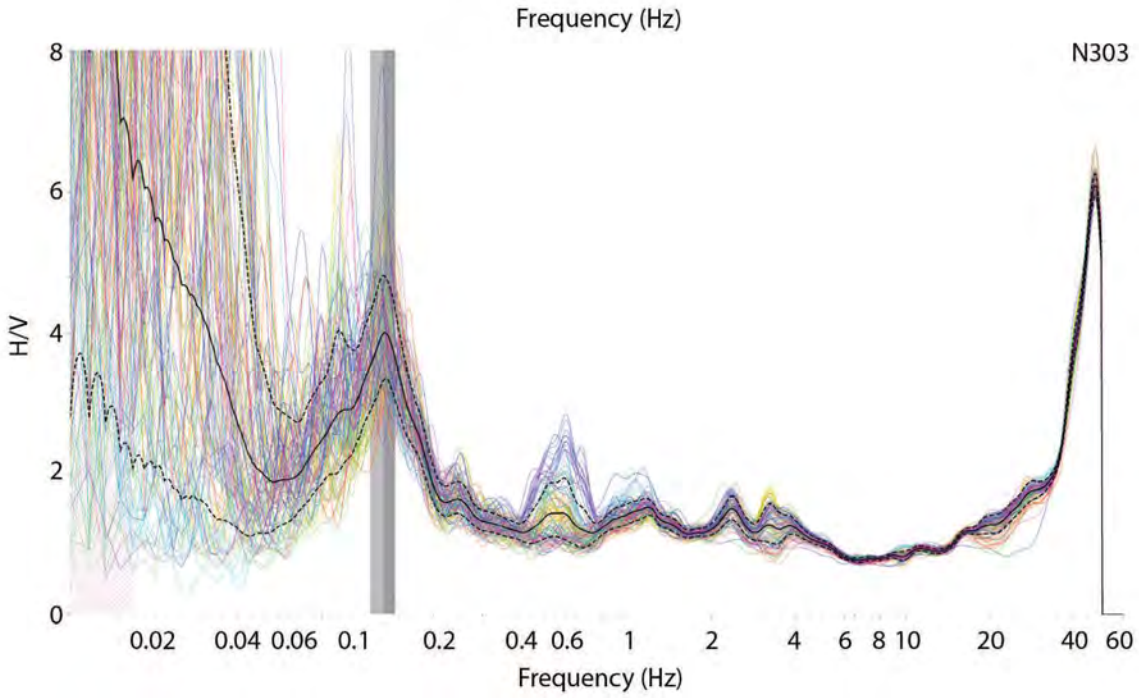

Figure C.33: *Station N302 - N303. Description is the same as figure C.1.*

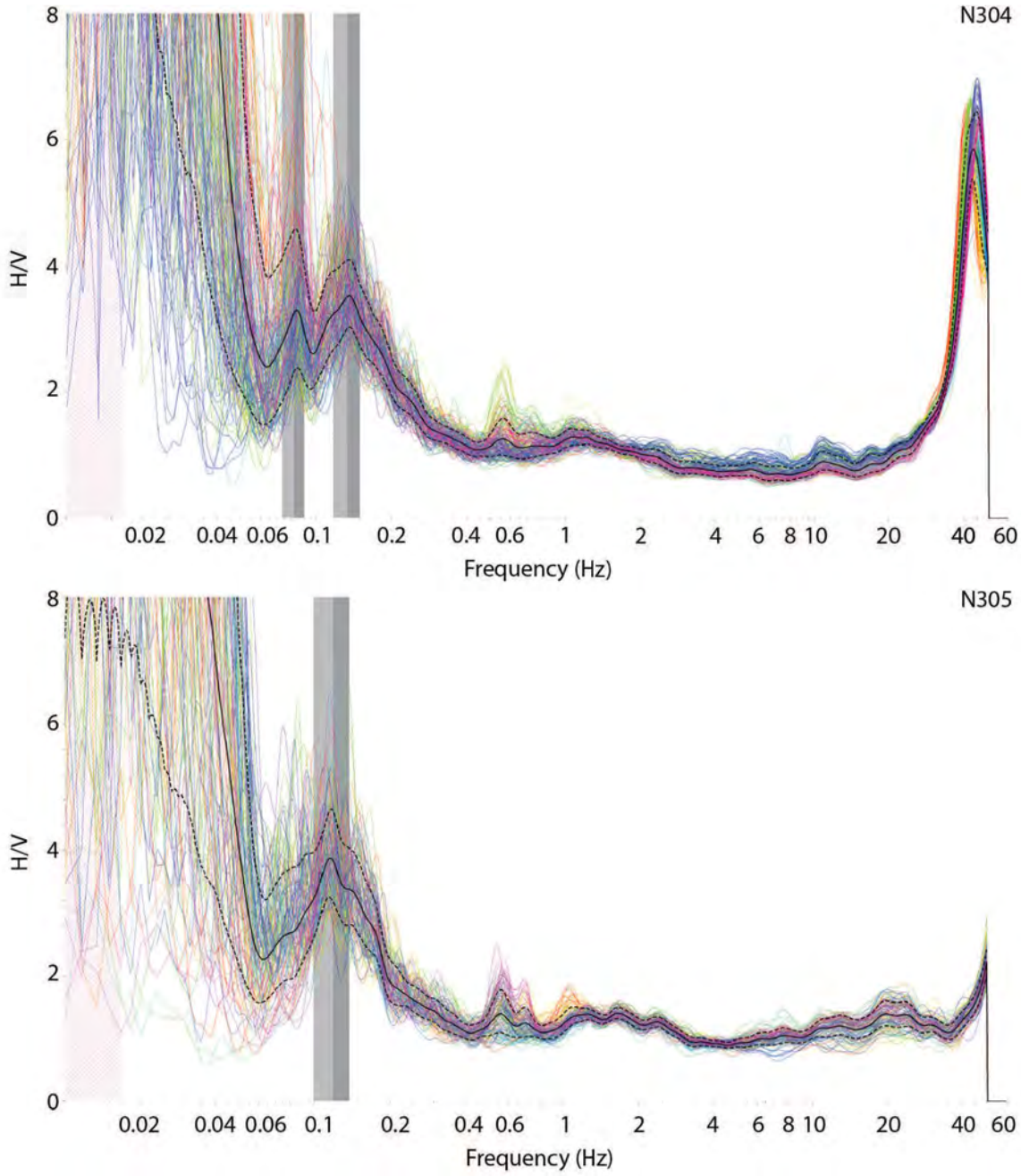

Figure C.34: *Station N304 - N305. Description is the same as figure C.1.*

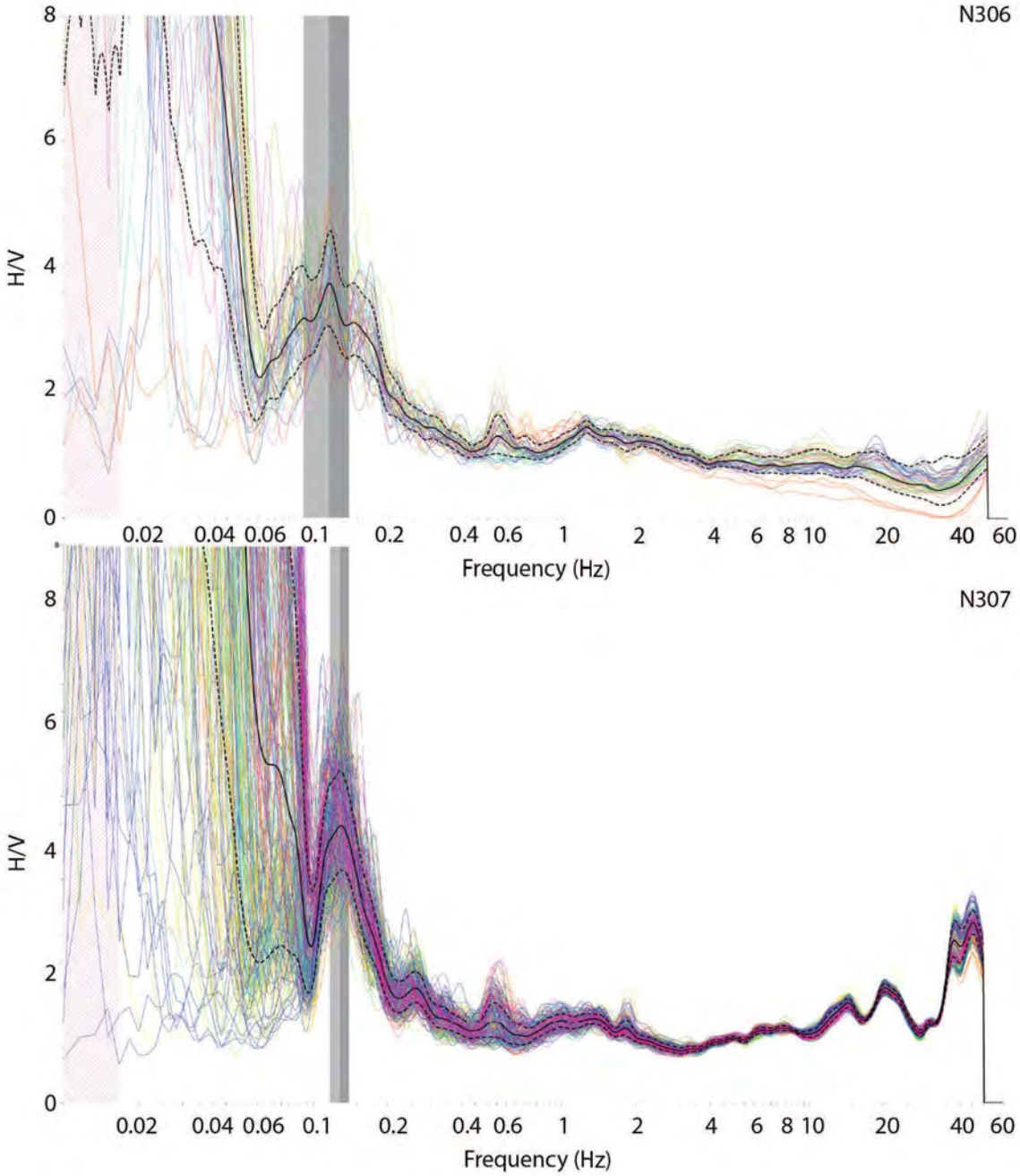

Figure C.35: *Station N306 - M307. Description is the same as figure C.1.*

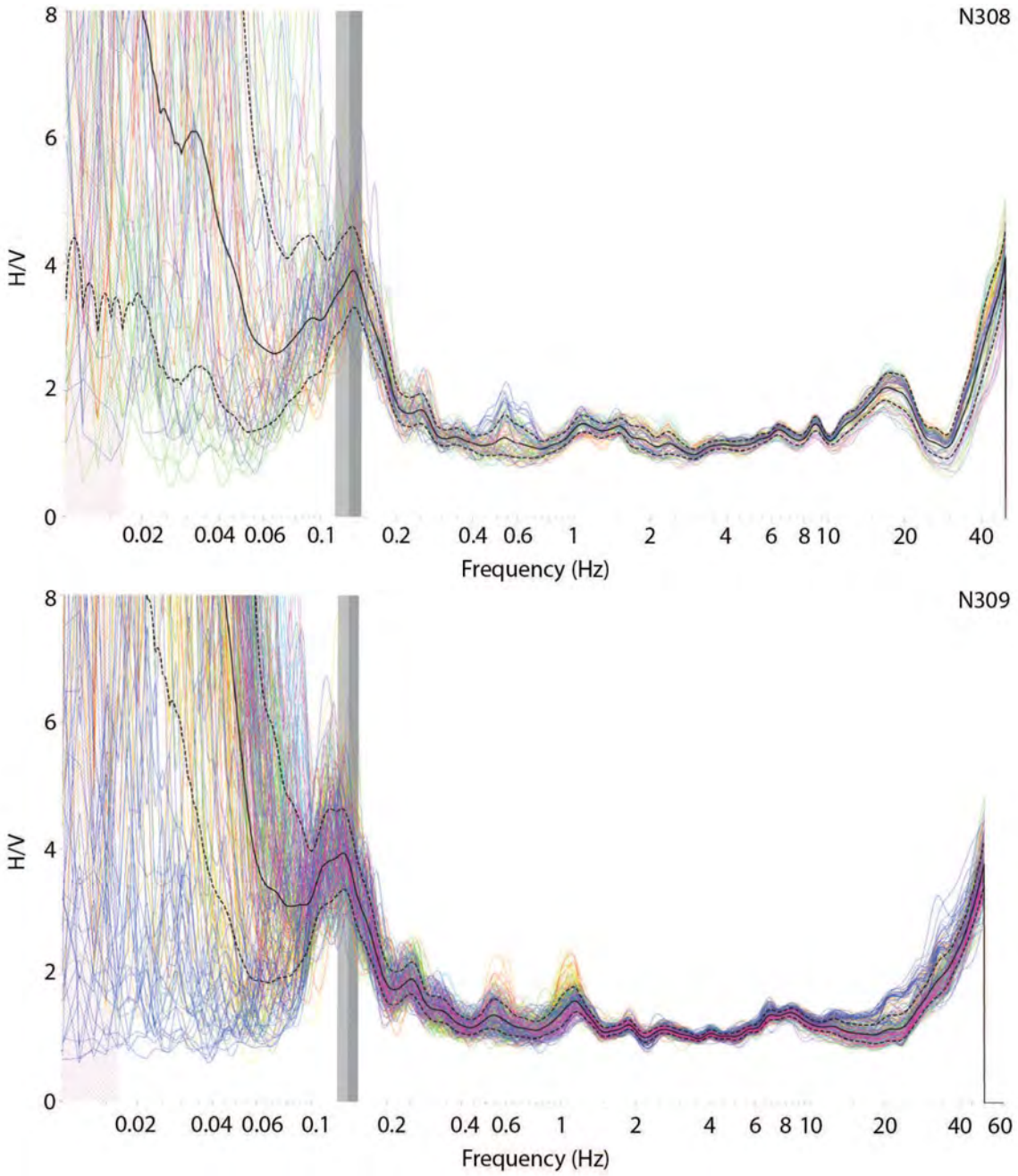

Figure C.36: *Station N308 - N309. Description is the same as figure C.1.*

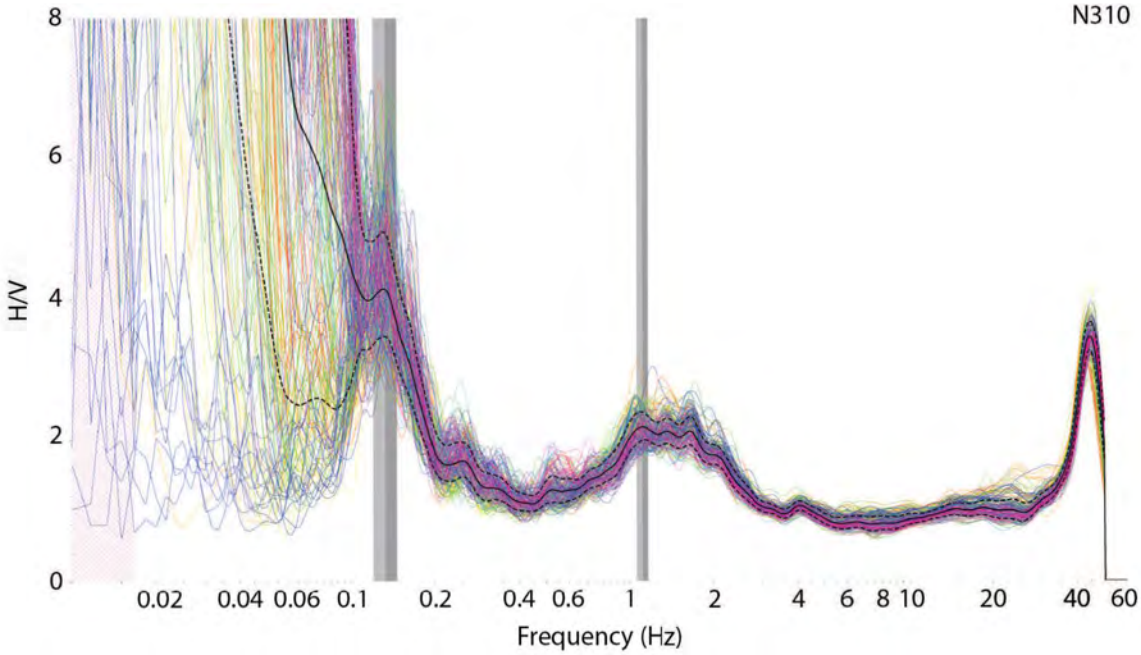

Figure C.37: *Station N309. Description is the same as figure C.1*